Scuola Normale Superiore

The metal enrichment of the intergalactic medium

Thesis

submitted for the degree of
Doctor Philosophiæ

Candidate:
Andrea Pallottini

Supervisor:
Prof. Andrea Ferrara
Co-supervisor:
Dr. Simona Gallerani

September 18, 2015

Abstract

The Big Bang Nucleosyhtesis produced a cosmic gas composed by Hydrogen and Helium, with virtually no trace of heavier elements (metals). Observations show that the diffuse and pervasive cosmic gas surrounding galaxies – the intergalactic medium (IGM) – is ubiquitously enriched with metals, that can only be produced by stars inside galaxies. In turn, the formation and evolution of galaxies is determined by the complex interplay between the interstellar medium and IGM, as mediated by the circumgalactic medium (CGM). Understanding how metal travelled to the IGM, when and from which galaxies are among the current challenge for cosmological models.

The *pre-enrichment* scenario is a theoretical framework that auto-consistently accounts for the evolution of galaxy formation and the cosmic enrichment history. In this picture, massive ($M_\star \gtrsim 10^{11}\mathrm{M}_\odot$) galaxies are able to retain their metals, while low mass ($M_\star \lesssim 10^{8}\mathrm{M}_\odot$) galaxies are prone to material ejection because of their shallower potential well. At high redshift ($z \gtrsim 7$), metal pollution is due to low mass galaxies ejecting metals via supernovae. Additionally, the same low mass galaxies driving the enrichment can play an important role in the first stages of cosmic reionization, since they are the ideal hosts for the first metal-free Population III stars, which may in turn be the responsible for an early reionization. Understanding cosmic metal enrichment is therefore fundamental to explain both the formation and the evolution of galaxies and the reionization history.

Aim of this work is to study the evolution of metal enrichment on galactic and intergalactic scales. Our analysis is based on cosmological simulations. Because of the huge dynamical range of the underlying physical phenomena, a true auto-consistent simulation is impossible, and a viable modelization can be achieved via subgrid models. We devise simulations by accounting for the trade off between implementing highly refined physical models and considering a cosmic volume large enough to allow a fair comparison with observations.

Among our key results, we show that galaxies develop a mass-metallicity ($M_\star$-Z) relation by $z = 6$. Our $M_\star$-Z relation agrees with $z = 4$ observations. The presence of cold enriched gas in the IGM/CGM implies that these metals must have been injected at epochs early enough to allow an efficient cooling as expected in a *pre-enrichment* scenario. Due to the physical conditions of the diffuse phases, C IV absorption line experiments can probe only $\simeq 2\%$ of the total carbon present in the IGM/CGM.

By analyzing each galactic environment, we find that the CGM density profiles are self-similar, once scaled with the virial radius of the parent dark matter halo. We then construct an analytical model for the H I absorption, testing it against synthetic spectra. When compared with available data, our CGM model nicely predicts the observed profile in $z \lesssim 2$ galaxies, and supports the idea that the CGM profile does not evolve with redshift.

We produce [C II] emission mock maps that can be directly compared with ALMA observations. At $z \simeq 6$ we find that the [C II] galaxy flux is correlated with M_{UV}, and such relation is in very good agreement with recent observations. In our mock maps we find that C II ions in the CGM/IGM can be seen as $\simeq \pm 0.1$ μJy/beam [C II] emission/absorptions features via CMB resonant scattering. Such signals are very challenging to be detected with current facilities.

Finally, we analyse the case of CR7 – the brightest $z = 6.6\,\mathrm{Ly}\alpha$ emitter (LAE) known to date – that might represent the first case of Pop III detection. If CR7 is powered by Pop III, we predict that in the COSMOS/UDS/SA22 fields, 14 out of the 30 LAEs with $L_\alpha > 10^{43.3}\mathrm{erg\,s^{-1}}$ should also host Pop III stars producing an observable $L_{\mathrm{HeII}} \gtrsim 10^{42.7}\mathrm{erg\,s^{-1}}$. As an alternate explanation, we explore the possibility that CR7 is instead powered by accretion onto a Direct Collapse Black Hole. Our model predicts L_α, L_{HeII}, and X-ray luminosities that are in agreement with the observations. We propose that further X-ray observations can distinguish between the two above scenarios.

FOREWORD

> With magic, you can turn a frog into a prince. With science, you can turn a frog into a Ph.D. and you still have the frog you started with.
>
> *The Science of Discworld (1999)*
> *Terry Pratchett (1948 - 2015)*

I acknowledge the Scuola Normale Superiore which has given me the possibility to meet stimulating people and to start international collaborations.

I thank the members of the **D**ark **A**ges **VI**rtual **D**epartment and the scientists whose efforts, work and fruitful discussions have made possible the studies published during my period of Ph.D: Sergio Campana, Carmelo Evoli, Chiara Feruglio, Eiichiro Komatsu, Roberto Maiolino, Jorryt Matthee, Andrei Mesinger, Valentina D'Odorico, Fabio Pacucci, Stefania Salvadori, Ruben Salvaterra, Daniel Schaerer, Raffaella Schneider, David Sobral, Livia Vallini, Bin Yue.

In particular, I thank Andrea Ferrara and Simona Gallerani, for turning frogs into Ph.D.s

CONTENTS

CHAPTER 1

INTRODUCTION

Our current understanding of the evolution of the Universe is based on the ΛCDM model. In this standard model, today the energy content of the Universe is composed by a mix of radiation (with density parameter $\Omega_r \sim 10^{-5}$), baryonic – visible – matter ($\Omega_b \simeq 0.04$), dark – interacting only via gravity – matter ($\Omega_{dm} \simeq 0.3$) and a dominant component of vacuum energy ($\Omega_\Lambda \simeq 0.7$). According to the standard model, the Universe began about 13.7 Gyr ago expanding from a hot and compact space-time singularity. At $t \sim 10^{-34}$s, the Universe underwent a brief period of exponentially accelerated expansion called Inflation (e.g. Liddle & Lyth, 2000). During this period the Universe size expanded by about 60 e-fold ($\simeq$ 26 order of magnitudes). At the end of Inflation, the Universe was highly homogeneous and isotropic on large scales, with vanishingly small local perturbations. After Inflation, the energy budget of the radiation dominated over the one of the matter, and the two components were thermally coupled.

The radiation kept driving the expansion, and the Universe temperature dropped with time – linearly with redshift (z). By $t \sim 10^2$s ($z \sim 10^{10}$), the temperature was low enough to allow the formation of light-nuclei, during the so-called Big Bang Nucleosynthesis (BBN). After $\simeq 20$ min the Universe was too cold and nuclear fusion became inefficient, effectively freezing the abundance of baryonic matter. As a result of BBN, the baryonic matter of the Universe was composed by hydrogen (H, 75%), helium (^{4}He, 24.8%), a small amount of Deuterium (D, $\simeq$ 0.002%) and almost no heavier elements, the so-called metals (e.g. Dodelson, 2003, Krane, 1987).

As the Universe keep expanding it became matter dominated at $t \sim 10$ kyr ($z \simeq 3500$), and then, as it kept cooling, at $t \sim 0.1$ Myr ($z \simeq 1100$) the radiation decoupled from matter at the so-called last scattering surface. This process led to the Recombination and to the formation of the Cosmic Microwave Background (CMB). Observations of the CMB can be used to accurately calculate the cosmic density parameters (Ω_x, e.g. Larson et al. 2011). In particular, such observations shows that today ($z = 0$) the CMB has a temperature of 2.725 (e.g. Fixsen, 2009), and anisotropies of order 10^{-5} (e.g. Planck Collaboration et al., 2014, see also Fig. D.1), due to the quantum fluctuations imprinted during the Inflation period. These anisotropies are associated with matter density perturbations existing at the recombination epoch. Gravitational instability allows these fluctuations in the density field to grow, forming a filamentary web-like structure, the so-called cosmic web. At this time, stars and (then) galaxies started to form predominantly at the intersections of these filaments (see Sec. 1.1).

Due to a lack of sources of light, the period between $z \simeq 1100$ ($t \sim 0.1\,\text{Myr}$) and the formation of the first stars at $z \sim 50$ ($t \sim 47\,\text{Myr}$) is known as the Dark ages. The stars in the first galaxies begun to produce both metals and radiation, in particular H I ionizing photons ($E_\nu > 13.6\,\text{ev}$). These photons in turn started to ionize the hydrogen in the surrounding fluctuating low density diffuse and pervasive cosmic baryonic component, the InterGalactic Medium (IGM). As these ionized regions started overlapping, they drastically changed the IGM thermodynamical state, during the evolutionary phase called Cosmic Reionization, that ended around $z \simeq 6-7$ ($t \sim 1\,\text{Gyr}$) (e.g. Gallerani et al., 2008a, Madau & Haardt, 2015, Mesinger et al., 2014).

The IGM has been extensively investigated through the study of the H I Lyα forest (Rauch, 1998) and the absorption features due to ionized metal species (e.g. Songaila & Cowie, 1996) detected in the spectra of high redshift quasars (QSO). Observations have probed metal enrichment in different intergalactic environments: damped Lyα absorbers (DLA), characterized by column densities $\log N_{\text{HI}}/\text{cm}^{-2} \gtrsim 20$ and representative metallicities $10^{-1.5} \lesssim Z/\text{Z}_\odot \lesssim 10^{-1}$ (cf. with Péroux et al., 2006); Lyman limit ($17 \lesssim \log N_{\text{HI}}/\text{cm}^{-2} \lesssim 20$) and Ly$\alpha$ forest ($14 \lesssim \log N_{\text{HI}}/\text{cm}^{-2} \lesssim 17$) systems, typically enriched at $10^{-3.5} \lesssim Z/\text{Z}_\odot \lesssim 10^{-2}$ (Meiksin, 2009).

The evolution of the IGM enrichment can be studied by measuring the abundance of ionized species at different cosmic times. For example, the C IV density parameter decreases with redshift from $\Omega_{\text{CIV}} \simeq 8 \times 10^{-8}$ at $z \simeq 0$ to $\Omega_{\text{CIV}} \simeq 10^{-8}$ at $z \simeq 2.5$ (e.g. D'Odorico et al., 2010), it is constant up to $\lesssim 5$ (e.g. Cooksey et al., 2010, Schaye et al., 2003), and could possibly show sign of a downturn, $\Omega_{\text{CIV}} \lesssim 0.5 \times 10^{-8}$, for $z \gtrsim 5$ (e.g. Becker et al., 2009, D'Odorico et al., 2013, Ryan-Weber et al., 2009, Simcoe et al., 2011). Similarly, Si IV displays a flat behavior for $2.5 \lesssim z \lesssim 5$ (Songaila, 2001, 2005).

Metals are produced by stars inside galaxies featuring a cosmic star formation rate density (SFR) $\simeq 10^{-2}\text{M}_\odot\text{yr}^{-1}\text{Mpc}^{-3}$ at $z = 0$, increasing up to one order of magnitude at $z \sim 3$ and decreasing by a factor $\sim 10^2$ for $3 \lesssim z \lesssim 9$ (Dunlop, 2013a). IGM is metal polluted by galaxies, whose SFR can be can used to infer the total metal density parameter. Pettini (1999) have shown that observations account for $\sim 20\%$ of metals at $z \gtrsim 2$, implying that the missing ones must be locked in a warm-hot ionized phase (e.g. Ferrara et al., 2005).

Galaxies with high ($M_\star \gtrsim 10^{11}\mathrm{M}_\odot$) and low ($M_\star \lesssim 10^{8}\mathrm{M}_\odot$) stellar mass display different characteristics. The local (Panter et al., 2008) and $z \lesssim 3$ (Maiolino et al., 2008, Mannucci et al., 2010) mass-metallicity ($M_\star - Z$) relation shows an increasing metal abundance with $M_\star$ from $\sim 10^{4}\mathrm{M}_\odot$ (Kirby et al., 2013) up to $\sim 10^{10}\mathrm{M}_\odot$ and a flattening for higher stellar mass. Similar difference is present in the dark-to-visible mass ratio (e.g. Guo et al., 2010, McGaugh & Wolf, 2010, Tolstoy, 2010): dwarf galaxies typically show values $\gtrsim 30$, while Milky Way size galaxies have a ratio $\lesssim 15$; for increasing mass the value approaches (but does not reach) the cosmological one, $\Omega_m/\Omega_b \sim 6$.

A theoretical framework must auto-consistently account for the history of IGM enrichment, its thermal state and the global evolution of galaxy formation. An attractive scenario consists in the so-called *pre-enrichment* (Ferrara, 2008, Madau et al., 2001), in which IGM pollution is mainly due to low mass ($M_\star \lesssim 10^{7}\mathrm{M}_\odot$) galaxies ejecting metals via supernova (SN) explosions at high redshift ($z \gtrsim 8$). In this picture massive galaxies are able to retain their metals, thus their evolution follows a closed box chemical model(e.g. Tremonti et al., 2004). On the other hand, low mass galaxies are prone to material ejection because of the shallower potential well and since their smaller size allows the SN to coherently drive the outflows (e.g. Ferrara & Tolstoy, 2000).

Ejection from low mass galaxies has an obvious advantage in terms of volume filling factor, given the abundance of these sources in ΛCDM models (i.e. Press & Schechter, 1974). Additionally, an early ($z \gtrsim 5$) IGM pollution allows the shocked and enriched gas to cool down (e.g. Ferrara, 2008), which can explain the observed narrowness (~ 15 km s^{-1}) of the Doppler width of metal lines (Meiksin, 2009).

The *pre-enrichment* scenario is appealing because the same low mass galaxies which start to pollute the IGM can play an important role in the first stages ($z \gtrsim 8$) of cosmic Reionization (e.g. Salvadori et al., 2014). In particular, (e.g. Choudhury et al., 2008) low mass galaxies are the ideal hosts for first metal-free Population III (Pop III) stars, which may possibly be the responsible for an early ($z \simeq 7$) Reionization (e.g. Gallerani et al., 2008a,b). However, the nature of Pop III stars is still under debate, because of lack of observations. From a theoretical point of view there is no clear consensus on their formation properties (Bromm et al., 2002, Greif et al., 2012, Hosokawa et al., 2012, Meece et al., 2014, Yoshida et al., 2006) nor their subsequent evolution (Heger & Woosley, 2002, Nomoto et al., 2006).

Thus, understanding the IGM metal enrichment from the first galaxies is fundamental to explain both the formation and the evolution of galaxies and the Reionization history

(Barkana & Loeb, 2001, Ciardi & Ferrara, 2005). However, it remains to be assessed the evolution of the temperature and chemical state of the enriched IGM, the imprint the metal transport has on the formation of new star forming regions and its role in the transition from Pop III to the successive generation of Population II (Pop II) stars. The steady increase of availability of high redshift IGM observations (e.g. D'Odorico et al., 2013) and their interpretation can hopefully clarify the picture, by better constraining the theoretical models.

Aim of this work is the study of joint evolution of metal enrichment on galactic and intergalactic scales. The key questions driving our research are:

- What is the cosmic metal enrichment history?
- What is the link between cosmic enrichment and Reionization?
- How does feedback regulate the galaxy-IGM interplay?
- How can we devise additional strategy to detect high-z metals?
- How can we probe the signature of the Pop III - Pop II transition?

To attack these questions, we have structured the Thesis as follows:

- Chapter 1: We conclude this Chapter by reviewing the theory of structure formation (Sec. 1.1) and the introduction to numerical methods (Sec. 1.2).
- Chapter 2: We devise numerical simulations to study the history of cosmic metal enrichment from the first galaxies.
- Chapter 3: We focus on the CircumGalactic Medium (CGM), the interface that regulates the interaction between the galaxy and the IGM.
- Chapter 4: We describe how far-infrared lines can be used to characterize the first galaxies and map the metals in the surrounding CGM/IGM.
- Chapter 5: We analyze the possible first detection of Pop III stars in CR7, the brightest $z = 6.6\,\mathrm{Ly}\alpha$ emitter known to date.

Finally, in Chapter 6, we state our conclusions.

1.1 Structure formation

In the standard ΛCMD model, structure formation is initially driven by the primordial density fluctuations in the matter power spectrum. Gravitational instability allows dark matter (DM) to collapse around these fluctuations, to create the so-called cosmic web. Around the potential well of the forming DM haloes the baryonic gas can collapse and condense. Eventually the collapse and the fragmentation lead to the formation of the first stars and galaxies. This turnpoint in the history of the Universe marks the end of the Dark Ages. These first light sources change forever the environment as these stars affect their surrounding with chemical, mechanical and radiative feedback. Thus the formation process is determined by the complicate interplay between the galaxies and the the IGM.

In this Sec. we briefly review the basic notions of structure formation theory. We star by describing the smooth universe and its evolution, then we analyze linear perturbation theory, some of the analytical methods used to solve non-linear perturbations. Then we conclude by focusing on the development of perturbations and the formation of halos. These topics represent the basic foundation of physical cosmology, and they are important in introducing the required terminology and solving method used in numerical analysis, that is discussed in Sec. 1.2. The main references we follow for the present overview are Dodelson (2003), Padmanabhan (1993), Peebles (1993).

1.1.1 Cosmological background

We start by reviewing the basic notion of general relativity, specializing the theory to the cosmological case step by step. In this Sec. Latin indexes range from 1 to 3 while Greek ones span from 0 to 4. We use Einstein sum convention, such that the world line element is indicated by

$$\mathrm{d}s^2 = g_{\mu\nu}\mathrm{d}x^\mu \mathrm{d}x^\nu , \tag{1.1}$$

where $g_{\mu\nu}$ is the metric and x^ν the coordinate. We choose the flat metric signature to be $(+,-,-,-)$. The covariant derivate ∇_μ behaves as a partial derivate when applied to a scalar field f

$$\nabla_\mu f = \partial_\mu f \,. \tag{1.2a}$$

When applied to a (covariant) vector field X^ν, the covariant derivate acts as

$$\nabla_\mu X^\nu = \partial_\mu X^\nu + \Gamma^\nu_{\mu\rho} X^\rho \,, \tag{1.2b}$$

where $\Gamma^\rho_{\mu\nu}$ is the Christoffel symbol. For a tangent (countervariant) field X_ν, the action of the covariant derivate can be written as

$$\nabla_\mu X_\nu = \partial_\mu X_\nu - \Gamma^\rho_{\mu\nu} X_\rho \,, \tag{1.2c}$$

and this behavior can be generalized to a n_1 times covariant and n_2 time countervariant tensor field $X^{\nu_1 \ldots \nu_{n_1}}_{\mu_1 \ldots \mu_{n_2}}$.

Intuitively, the Christoffel symbol $\Gamma^\rho_{\mu\nu}$ describes change of base coordinates due to the derivate. Formally, $\Gamma^\rho_{\mu\nu}$ can be uniquely determined upon assuming metric compatibility (i.e. $\nabla_\lambda g_{\mu\nu} = 0$) and a torsion-free connection[1]:

$$\Gamma^\rho_{\mu\nu} = \frac{1}{2} g^{\rho\lambda} \left(\partial_\mu g_{\nu\lambda} + \partial_\nu g_{\mu\lambda} - \partial_\lambda g_{\nu\mu} \right) \,. \tag{1.3}$$

The action of gravity in general relativity is accounted by the curvature tensor. Intuitively, the curvature is the operator that quantifies the difference in following a vector along the two directions of a loop path. Formally, the curvature is defined by the commutator of two successive covariant derivate

$$\left[\nabla_\mu, \nabla_\rho \right] X^\nu = \nabla_\mu \nabla_\rho X^\nu - \nabla_\rho \nabla_\mu X^\nu = R^\nu_{\mu\rho\lambda} X^\lambda \,. \tag{1.4}$$

The curvature can be calculated from the above definition by expressing Christoffel symbol with eq. 1.3

$$R^\nu_{\mu\rho\lambda} = \nabla_\rho \Gamma^\nu_{\mu\lambda} - \nabla_\lambda \Gamma^\nu_{\mu\rho} + \Gamma^\beta_{\mu\lambda} \Gamma^\nu_{\beta\rho} - \Gamma^\beta_{\mu\rho} \Gamma^\nu_{\beta\lambda} \,. \tag{1.5a}$$

The Ricci tensor (1.5b) and the Ricci scalar (1.5c) can be formed by contraction of $R^\nu_{\mu\rho\lambda}$ as follows

$$R_{\mu\nu} = R^\rho_{\mu\rho\nu} \tag{1.5b}$$

$$R = R^\mu_\mu \,, \tag{1.5c}$$

and the Einstein tensor is defined as

$$G_{\mu\nu} = R_{\mu\nu} - \frac{1}{2} g_{\mu\nu} R \tag{1.5d}$$

The equation of motion can be derived from the action principle. Following the Einstein-Hilbert treatment, we chose a gravitational Lagrangian density of the form $\mathcal{L}_g \propto R$. The proportionality constant can be fixed *a posteriori*, by matching the relativistic description

---

[1] For a proper introduction, the term torsion-free requires additional concepts from Riemannian geometry (e.g. Wald, 1984). For this introduction, it is sufficient to state that torsion-free implies symmetric Christoffel symbol i.e. $\Gamma^\rho_{\mu\nu} = \Gamma^\rho_{\nu\mu}$.

with Newtonian gravity

$$\mathcal{L}_g = -\frac{1}{16\pi G} R \,. \tag{1.6}$$

By adding a source term $\mathcal{L}_s$, the complete action S becomes

$$S = \int \mathrm{d}x^4 \sqrt{-g} \left(\mathcal{L}_s - \frac{1}{16\pi G} R \right) \,, \tag{1.7}$$

where $\mathrm{d}x^4\sqrt{-g}$ is the invariant volume element. We are now able to solve the fixed extremes variation calculus of the action presented in eq. 1.7. The solution is known as the Einstein equation:

$$G_{\mu\nu} = 8\pi G T_{\mu\nu} \,, \tag{1.8}$$

where $T_{\mu\nu}$ is the stress-energy tensor associated with the source term $\mathcal{L}_s$

$$T_{\mu\nu} = \frac{2}{\sqrt{-g}} \left(\frac{\partial}{\partial g^{\mu\nu}} - \partial_\lambda \frac{\partial}{\partial \left(\partial_\lambda g^{\mu\nu}\right)} \right) \sqrt{-g} \mathcal{L}_s \tag{1.9}$$

The formal definitions we have introduced so far can be simplified by focusing on the cosmological case. We want to describe the primordial smooth universe, therefore we can assume homogeneity and isotropy at every fixed time t. Such assumption is equivalent to require a maximal 3-dimensional symmetric space. This in turn restrict the spatial (3-dimensional) metric to be of the form

$$\mathrm{d}x^i \mathrm{d}x_i = \frac{\mathrm{d}r^2}{1-\kappa r^2} + r^2 \mathrm{d}\Omega^2 \,, \tag{1.10}$$

where κ is a constant that depend on the spatial curvature. Then the full space-time 4-dimensional metric can be written – up to coordinate transformation – as

$$\mathrm{d}s^2 = c^2 \mathrm{d}t^2 - a^2(t) \left(\frac{\mathrm{d}r^2}{1-\kappa r^2} + r^2 \mathrm{d}\Omega^2 \right) \,, \tag{1.11}$$

where $a(t)$ is the expansion factor. This is the Robertson-Walker metric, these coordinates are called comoving. Note that in this formal context the redshift can be defined as $1 + z = a(t = 0)/a(t)$. From now on we assume to be in the $\kappa = 0$ (flat) case. From the metric (eq. 1.11) we can calculate the Christoffel symbol (eq. 1.3) and then solve the Einstein equation (eq. 1.8).

Now, eq. 1.8 describe a system of 16 partial differential equations. Since $G_{\mu\nu}$ and $T_{\mu\nu}$ are symmetric, only 10 of such equations are independent. Due to isotropy, there must be no off-diagonal term and the degree of freedom drops from 10 to 4. Because of homogeneity, the spatial part must be redundant, and therefore the equations are further reduced from 4 to 2.

Thus, the smooth universe evolution can be described by two equations. To find them, it is convenient to choose a functional form for the stress-energy tensor (eq. 1.9). In a smooth universe, $T_{\mu\nu}$ can be characterized as a perfect fluid with energy density ρ, pressure p, and velocity U^μ. In general we can therefore write

$$T^{\mu\nu} = \left(\rho + \frac{p}{c^2}\right) U^\mu U^\nu - g^{\mu\nu}\frac{p}{c^2}\,, \tag{1.12}$$

where c is the speed of light. Since the fluid has to be in rest with the comoving frame, it velocity U^μ must be $(1,0,0,0)$. Additionally, homogeneity and isotropy imply that ρ and p are constant in space.

Therefore, starting from Einstein equation (eq. 1.8), using the form from $T_{\mu\nu}$ given in eq. 1.12, and after some algebra, we are left with the Friedman equations

$$\frac{\ddot{a}}{a} = -\frac{4\pi}{3}G\left(\rho + 3\frac{p}{c^2}\right) \tag{1.13a}$$

$$\frac{\dot{a}}{a} = \sqrt{\frac{8\pi}{3}G\rho}\,. \tag{1.13b}$$

To solve the Friedman equations, the stress-energy tensor must be further specialized. $T_{\mu\nu}$ must take into account the various constituents (e.g. radiation, matter, ...) of the Universe. For simplicity, we can treat each component separately. It is useful characterize different component with the equation of state (EOS). The distinction between radiation (indicated with subscript r) and matter (m) in the perfect fluid limit can be written as

$$\left\| \begin{array}{ll} p_r = \frac{1}{3}c^2\rho_r & \quad \text{radiation} \\ p_m = 0 & \quad \text{matter} \end{array} \right.$$

Note that in the perfect fluid approximation the components interact only through gravity. It is a direct consequence from the assumptions of homogeneity and isotropy. Further, as the system is closed, conservation of energy must hold separately for each component. Using the definition of the stress-energy tensor (eq. 1.9), we can write energy conservation as[2]

$$\nabla^\mu T_{\mu\nu} = 0 \tag{1.14}$$

---

[2] Note that, the following result can be alternatively obtained by applying the metric compatibility to the Einstein equation (eq. 1.8).

Combining the above eq. 1.14 with the EOS, we can solve the scale factor dependence for the densities of radiation and matter

$$\rho_r \propto a^{-4} \tag{1.15a}$$

$$\rho_m \propto a^{-3} \,. \tag{1.15b}$$

It is useful to rewrite these equations in terms of the cosmic parameter

$$\Omega_x = \frac{\rho_x}{\rho_c} = \rho_x \frac{8\pi G}{3H_0^2} \,, \tag{1.16}$$

where H_0 is the Hubble constant, x can indicate radiation (r) or matter (m). Within this formalism we can introduce the vacuum term by allowing the existence of a fluid with the following EOS

$$p_\Lambda = -\frac{1}{3} c^2 \rho_\Lambda \,. \tag{1.17}$$

Then, the energy tensor associated to the vacuum is

$$T_{\mu\nu} = \Lambda g_{\mu\nu} \tag{1.18}$$

an its density parameter can be expressed as

$$\Omega_\Lambda = \frac{\Lambda c^2}{3H_0^2} \,. \tag{1.19}$$

From eq. 1.14 and metric compatibility, it is immediate to see that the energy density associated with the vacuum does not evolve with time. Note that it sometimes convenient to re-write Friedman equations as a function of cosmic parameters for matter, radiation and Λ and their temporal evolution. For example, eq. 1.13b would read

$$\left(\frac{H}{H_0}\right)^2 = \Omega_r a^{-4} + \Omega_m a^{-3} + \Omega_\Lambda \,, \tag{1.20}$$

where $H(t) = \dot{a}/a$ is the Hubble parameter (and $H_0 = H(t = 0)$).

1.1.2 Linear perturbation theory

Structure formation is not allowed in a pure Friedman Robertson Walker universe described through eq.s 1.13a and 1.13b. Inhomogeneity and anisotropy must be included in our description via perturbations. Then, gravitational instability will naturally lead to structure formation. Here we present the main methods used in perturbation theory, that are the base for semi-analytical treatment and are in turn used as a start for numerical simulation (see Sec. 1.2.3).

The first step is to select the kind of perturbation that affects the metric. Various theories allow different perturbations, that can be characterized by their transformation properties, i.e. scalar, vector or tensor. Such representation is helpful because the evolution of different perturbations modes is uncorrelated, due to the decomposition theorem (e.g. Dodelson, 2003).

We can restrict our study to scalar perturbation, as it is directly linked to the density perturbation. Scalar perturbations are completely determined by two functions, let them be Ψ and Φ. The perturbations can depend both on t and $\mathbf{x}$, and they modify the metric as follows

$$g_{00} = c^2\left(1 + 2\frac{\Psi}{c^2}\right) \tag{1.21a}$$

$$g_{ij} = -a^2\delta_{ij}(1 + 2\Phi) \tag{1.21b}$$

Note that, if the expansion factor is identically equal to one, the metric would describe gravity in the weak field limit. Thus, Ψ can be interpreted as a generalized Newtonian potential and Φ a perturbation accounting for spatial curvature effects. Once the perturbed stress-energy tensor is computed, the evolution can be calculated through the Einstein eq. 1.8.

Upon perturbing the smooth universe, the perfect fluid limit no longer holds. As interactions between the universe components becomes important, we must further characterize matter and radiation. Baryonic (visible) matter must be distinguish between relativistic and cold, e.g.[3] electrons and protons respectively. Both electrons and protons are coupled with radiation, e.g. photons. Baryonic matter and photons, along with neutrinos and DM are affected and in turn affect the metric. These interaction generate an autoconsistent system once the initial perturbations are known.

The Boltzmann equation is the tool to properly account for these contributions. Generally speaking, the equation describe the evolution of the distribution functions of the various components in the extended (with the temporal dimension) phase space

$$\frac{\mathrm{d}}{\mathrm{d}t} f(t, \mathbf{x}, \mathbf{p}) = C(f)\,, \tag{1.22}$$

and there is one Boltzmann equation – distribution – for each component indicated above. The left hand side of eq. 1.22 takes into account the interaction through gravity and the

---

[3] This distinction depend on the age of the Universe. In the following we assume to be at $t \gtrsim 30\,\mathrm{min}$, after the BBN.

peculiar characteristic of the chosen component. The right hand side of eq. 1.22 is the collision term, which depict the couplings with the other distribution functions. For simplicity sake, in this Sec. we use god-given unit, i.e. $G = c = 1$.

To describe structure formation, we focus on Boltzmann equation for the DM distribution f_{dm}. In the standard ΛCDM model, DM interacts only gravitationally[4]. Thus we have an identically null collision term, $C(f_{\mathrm{dm}}) = 0$, and the perturbation will be linked only to the metric. We restrict our analysis to cold (massive) DM: this gives a constraint on the relative 4-momentum

$$P^\mu = \frac{\mathrm{d}}{\mathrm{d}\lambda} x^\mu \tag{1.23a}$$

$$P^2 = g_{\mu\nu} P^\mu P^\nu = m^2_{\mathrm{dm}} \tag{1.23b}$$

where m_{dm} is the DM mass. Using the above eq.s, the DM spatial impulse and the energy can be naturally defined as

$$\left\| \begin{aligned} & p^2 = g_{ij} P^j P^i \\ & E = \sqrt{p^2 + m^2_{\mathrm{dm}}} \end{aligned} \right.$$

Using eq.s 1.21, we can express the momentum of the DM with the norm of the spatial impulse p and its direction $\hat{p}^i$.

$$P^\mu = \left(E(1-\Psi), p\hat{p}^i \frac{1-\Phi}{a} \right) \tag{1.24}$$

It is useful to write the functional dependence of the DM distribution as $f_{\mathrm{dm}} = f_{\mathrm{dm}}(t, x^i, E, \hat{p}^i)$. Inserting this in the collision-less Boltzmann equation – and after some algebra – we have

$$\partial_t f_{\mathrm{dm}} + \frac{p\hat{p}^i}{aE} \partial_{\hat{p}^i} f_{\mathrm{dm}} - \left(\frac{p^2}{E} \partial_t \log a + \frac{p^2}{E} \partial_t \Phi + \frac{p\hat{p}^i}{a} \partial_{x^i} \Psi \right) \partial_E f_{\mathrm{dm}} = 0 \tag{1.25}$$

Solution for the Boltzmann eq. can recursively be given in terms of the moments of the equation. The j-th moment is defined by integrating the Boltzmann eq. by $(p\hat{p}^i/E)^j \mathrm{d}^3p/(2\pi)^3$. Similarly to non-relativistic hydrodynamics, we can define the number density n_{dm} and the velocity v^i_{dm} as

$$\left\| \begin{aligned} & n_{\mathrm{dm}} = \int \frac{\mathrm{d}^3p}{(2\pi)^3} f_{\mathrm{dm}} \\ & v^i_{\mathrm{dm}} = \frac{1}{n_{\mathrm{dm}}} \int \frac{\mathrm{d}^3p}{(2\pi)^3} \frac{p\hat{p}^i}{E} f_{\mathrm{dm}} \end{aligned} \right.$$

---

[4] The fact that DM interacts only gravitationally is an assumption. E.g. see Cirelli et al. (2011) for a detailed analysis of DM interaction, Valdés et al. (2013) for DM effect on the epoch of Reionization, and Schön et al. (2015) for DM effect on structure formation.

By using these quantities, we can express the firsts moments of eq. 1.25. By suppressing surface terms we have

$$\left(\frac{p\hat{p}^i}{E}\right)^0 \quad \mapsto \quad \partial_t n_{\rm dm} + \frac{1}{a}\partial_{x^i} n_{\rm dm} v^i_{\rm dm} + 3\left(\partial_t \log a + \partial_t \Phi\right) n_{\rm dm} = 0 \tag{1.26a}$$

$$\left(\frac{p\hat{p}^i}{E}\right)^1 \quad \mapsto \quad \partial_t n_{\rm dm} v^i_{\rm dm} + 4\left(\partial_t \log a\right) n_{\rm dm} v^i_{\rm dm} + \frac{n_{\rm dm}}{a}\partial_{x^i}\Psi = 0 \tag{1.26b}$$

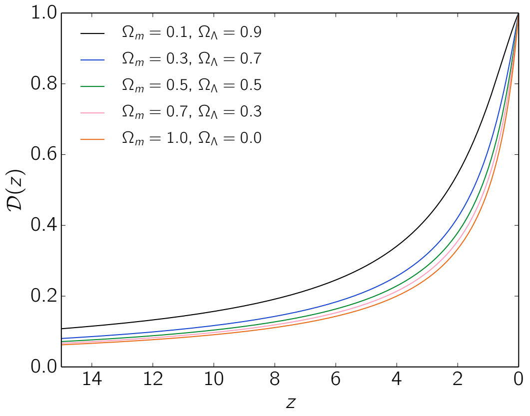

FIGURE 1.1: Growth function ($\mathcal{D}$) evolution with redshift (z). With different colors we plot the growth function obtained with different set of cosmological parameters, as indicated as an inset. Note that Ω_r would influence the early time ($z \gtrsim 100$) trend of $\mathcal{D}$ because of the steep redshift evolution for radiation (eq. 1.15a).

Here it is worth checking the behavior of the first order approximations. In the 0-th moment (eq. 1.26a), for an unperturbed universe (zero order), by dropping all high order terms we get

$$\partial_t n^0_{\rm dm} + 3\left(\partial_t \log a\right) n^0_{\rm dm} = 0\,. \tag{1.27}$$

Thus in 0-th term the zero order is equivalent to the conservation of energy for matter in eq. 1.15b, namely $n^0_{\rm dm} \propto a^{-3}$. It seems therefore natural to choose a DM number density of the form

$$n_{\rm dm} = n^0_{\rm dm}(t)(1 + \delta_{\rm dm}(t, \mathbf{x}))\,, \tag{1.28}$$

where the DM density perturbation is expressed via $\delta_{\rm dm}$, the density contrast. Using eq. 1.26a, the evolution $\delta_{\rm dm}$ at the first order (linear) can be written as

$$\partial_t \delta_{\rm dm} + \frac{1}{a}\partial_{x^i} v^i_{\rm dm} + 3\partial_t \Phi = 0\,. \tag{1.29}$$

This equation includes an additional perturbation, in the form of a velocity term $v^i_{\rm dm}$. To account for the velocity, we must turn our attention to the first moment (eq. 1.26b). Neglecting second order terms and using $n^0_{\rm dm}$ time dependence, we have

$$\partial_t v^i_{\rm dm} + \left(\partial_t \log a\right) v^i_{\rm dm} + \frac{1}{a}\partial_{x^i}\Psi = 0 \tag{1.30}$$

Note that we have no first order pressure-like term, since we assumed the DM to be cold. This final set of eq.s can be solved simultaneously once the metric perturbation is known.

Giving an explicit solution for eq.s 1.29 and 1.30 is not among our aims. However, it is important and it can be shown (e.g. Padmanabhan, 1993) that the set of equations allows two kind of solutions for $\delta_{\rm dm}$. Looking in the Fourier space, these solutions are associated with perturbations with typical scale greater or smaller than wavelength corresponding to the Hubble scale R_H, i.e. $k_H = 2\pi/R_H = 2\pi\, c\, H^{-1}$. Thus, the growth of the perturbations depend on the ratio between the wavelength and k_H, that in in turn depends on the dominant universe component that is determining the metric evolution (see eq. 1.20) and its perturbation.

In general, perturbations are written via the transfer function formalism (e.g. Dodelson, 2003)

$$\delta_{\rm dm}(k,t) \propto \mathcal{T}(k)\mathcal{D}(a)\,, \tag{1.31}$$

where $\mathcal{T}$ is the transfer function and $\mathcal{D}$ is called the growth function. $\mathcal{T}$ describes the evolution of the perturbation at the horizon (k_H) crossing, while $\mathcal{D}$ describes the late time ($z \lesssim 100$) wavelength independent evolution (e.g. Bardeen et al., 1986). An example of the evolution of the growth function is plotted in Fig. 1.1. $\mathcal{D}$ is calculated following the approximation given in Lahav et al. (1991).

1.1.3 Beyond linear theory: the growth of perturbations

The description done so far can be used to follow the evolution of small perturbations. From non-relativistic fluid dynamics, we expect that such small perturbations can leave the linear regime because of gravitational instability. In cosmology, we can expect gravitational instability to be important where the matter density contrast grows faster than the expansion of the universe. In those locations, second order terms are not negligible as the matter struggle to become pressure supported and the evolution is determined by the Jeans theory.

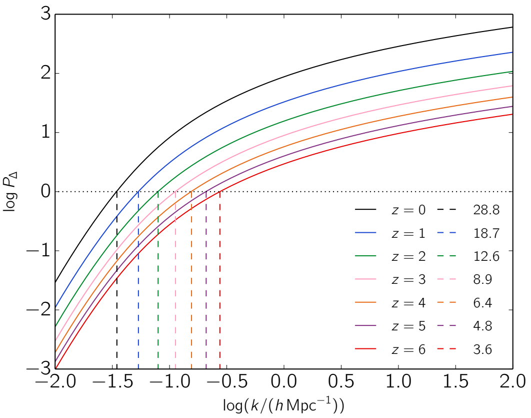

FIGURE 1.2: Dimensionless power spectrum (P_Δ, eq. 1.46b) evolution with redshift (eq. 1.31 and see Fig. 1.1). Calculations at different redshifts are plotted with different colors. With a horizontal dotted line we indicate the estimate for the non-linear scale, i.e. $P_\Delta(k = k_{nl}) = 1$. At each redshift, the corresponding non-linear scale is indicated with a vertical dashed line. Each line is labelled with $1/k_{nl}$, in unit of Mpc/h.

As perturbations grows in amplitudes, we expect that local effect becomes progressively more important. Since we are interested in effect below the horizon scale, we can analyze the scenario in the Newtonian limit. The limit can be taken by modifying the metric used so far. We assume that the energy-energy perturbation Ψ (eq. 1.21a) is due to a cosmological background plus a perturbation given by the DM component. In addition we can set the matter-matter Φ component (eq. 1.21b) to zero since it is an higher order in c respect to Ψ. Thus, the system of eq.s 1.21 retain its form, and it is further constrained by

$$\Psi = -\frac{1}{2}\frac{\partial_{t^2} a}{a}|\mathbf{x}|^2 + \delta\Psi \tag{1.32a}$$

$$\Phi = 0 \tag{1.32b}$$

Self-consistency is guaranteed by using a Poisson equation for $\delta\Psi$. Note that, as Φ is assumed to be null, in this limit the zero order velocity is given by the Hubble flow, that yields a pressure-like term. We now can combine eq.s 1.30 and 1.32, and it is convenient to express the result with $\delta(k)$, the spatial Fourier transform for the density contrast:

$$\partial_{t^2}\delta + 2\frac{\partial_t a}{a}\partial_t \delta + \frac{k^2 v^2}{a^2}\delta \simeq 4\pi G \rho^0_{\mathrm{dm}} \delta \,. \tag{1.33}$$

Note that in principle, the right hand side of the equation should account not only for the DM but for the total unperturbed energy density. For clarity sake, in this presentation we neglect these contributions. Additionally, eq. 1.33 is obtained in the Newtonian limit. We recall that this assumption translates into the impossibility of using eq. 1.33 for those perturbation with scale (wavelength) larger than the (inverse of) causal horizon scale.

Eq. 1.33 does not allow a straightforward analytical solution. However, we can qualitatively describe the evolution of structure in term of Jeans length. Note that in eq. 1.33 a damping term ($\partial_t \delta$) is present, thus the Jeans length evolve accordingly to the expansion of the universe. We expect this evolution to act against the self-gravitation of the objects considered – roughly speaking – it will contribute to the pressure support of the gas.

To have a the picture of the Jeans instability, we can further limit the analysis by adding some assumptions. Firstly, we let the initial overdensity to be spherically symmetric about a point, that is used as the origin of the spatial coordinate. The evolution of a infinitesimal shell located at $r = a\,|\mathbf{x}|$ is determined by the potential Ψ. It can be expressed in terms of the mass of the shell and the mean mass of the region inside the shell itself as

$$\frac{\mathrm{d}^2}{\mathrm{d}t^2} r = -\frac{GM}{r^2} \tag{1.34}$$

where $M(\mathbf{x}, t) = M_b(\mathbf{x}) + \delta M(\mathbf{x}, t)$ with

$$M_b = \frac{4\pi}{3}\rho^0_{\mathrm{dm}} r^3 = \mathrm{cost} \tag{1.35a}$$

$$\delta M = 4\pi\rho^0_{\mathrm{dm}} \int_0^r \delta r'^2 \mathrm{d}r' \tag{1.35b}$$

Then, we further assume that the spherical shells do not cross each other during their evolution: this guarantee that we can label each layer with increasing radii and that the order is maintained during the temporal evolution. This makes δM constant in time once r_i is chosen and, in turn, eq. 1.34 can be integrated to yield

$$\frac{1}{2}\left(\frac{\mathrm{d}}{\mathrm{d}t}r\right)^2 - \frac{GM}{r} = E\,, \tag{1.36}$$

where E is a constant of integration: its sign determines if the region can eventually collapse or if it keeps expanding. As E is constant, it can be evaluated at the time t_i chosen such that the peculiar velocities are negligible. Using the subscript i for the quantity at the time t_i we have

$$\left.\frac{1}{2}\left(\frac{\mathrm{d}}{\mathrm{d}t}r\right)^2\right|_{t_i} = \frac{1}{2}\left(H_i r_i\right) + o(v_i) \tag{1.37a}$$

$$\left.\frac{GM}{r}\right|_{t_i} = \frac{1}{2}\left(H_i r_i\right)\Omega_i(1 + \langle\delta_i\rangle) \tag{1.37b}$$

where $\langle\delta_i\rangle$ is the mean density contrast inside r_i. The condition of collapse can be therefore written as

$$\langle\delta_i\rangle > (\Omega_i^{-1} - 1) > 0\,, \tag{1.38}$$

where the last inequality holds since we are working in a flat universe. The actual region collapse is governed by eq. 1.36. Its solution can be expressed in a parametric form

$$r \propto (1 - \cos\theta) \tag{1.39a}$$

$$t \propto (\theta - \sin\theta) \tag{1.39b}$$

The picture is the following: a shell initially expand along with the background, slows down and then turn around and collapse. The constants of proportionality can be calculated by using the bound at time t_i and by additionally labelling the maximum expansion radius as r_m. In this case the problem is completely determined: it is possible to calculate collapse time, the virial radius and the other parameters of the shell given the initial conditions. In particular, the theory predicts (e.g. Padmanabhan, 1993) the perturbation collapse when the overdensity reaches the value $\delta_c \simeq 1.686$. We will get back to this point later in the Sec..

There is an another classical analytical approach to structure formation theory, the so called Zeldovich approximation. It is interesting because it is analytical and, at the same time, allows to drop the hypothesis of spherical symmetry. The approximation consists in expressing the linear theory for particles mixing the Euler and the Lagrangian description. Note that even this treatment holds only for scales below the causal horizon. We denote with $\mathbf{r} = a\mathbf{q}$ the position of particles in a smooth universe. Within linear theory, a perturbation is due to two function b and $\mathbf{p}$ such that

$$\mathbf{r}(t) = a(t)\left(\mathbf{q} + b(t)\mathbf{p}\left(\mathbf{q}\right)\right) . \tag{1.40}$$

Using the above eq. as a definition, linear theory would imply that the density contrast must satisfy

$$\delta = -b\nabla\mathbf{q} \tag{1.41}$$

The match between the linear and the Zeldovich description is obtained by expanding the initial density perturbation in the Fourier modes $A_{\mathbf{k}}$

$$\mathbf{p}\left(\mathbf{q}\right) = \sum_{\mathbf{k}} \frac{i}{k^2}\mathbf{k}A_{\mathbf{k}} \exp\left(i\mathbf{k}\mathbf{q}\right) \tag{1.42}$$

By defining the potential Φ_0 as

$$\Phi_0 = \sum_{\mathbf{k}} \frac{A_{\mathbf{k}}}{k^2} \exp\left(i\mathbf{k}\mathbf{q}\right) , \tag{1.43a}$$

we can write eq. 1.42 as

$$\mathbf{p}\left(\mathbf{q}\right) = \nabla\Phi_0\left(\mathbf{q}\right) . \tag{1.43b}$$

Therefore, the relation between the generalized Newtonian potential Φ and the Zeldovich Φ_0 is obtained using the first Friedman equation (eq. 1.13a)

$$\Phi = 3ab\Phi_0\partial_{t^2}a \tag{1.44}$$

The meaning is that Φ_0 is directly linked to the gravitational potential and $\mathbf{p}$ is proportional to the velocity field. Being $\mathbf{p}$ a gradient of the scalar function, its associated matrix is diagonalizable. Denoting with λ_i its eigenvalues, the perturbed density contrast can be formally written as

$$\delta = \left[\sum_{i=1}^{3} (1 - b(t)\lambda_i(\mathbf{q}))\right]^{-1} - 1\,. \tag{1.45}$$

In collapsing regions at least one of the bracketed term approach unity. Unlike the spherical collapse, it is sufficient for a principal axis to diverge to get to the nonlinear regime. By probability, this case is more likely to happen than a tri-axial collapse. Thus, qualitatively, we can expect that the first non-linear structure must be pancake-like, and they will be generally less dense and more numerous than 3-dimensional collapsed regions. By the same probability argument, void regions must be rare as 3-dimensional collapsed regions. This gives a glimpse of the cosmic-web structure. Finally, it is worth noting that this approximation is usually implemented to construct initial conditions in N-body simulations (see Sec. 1.2.3).

1.1.4 Statistical properties

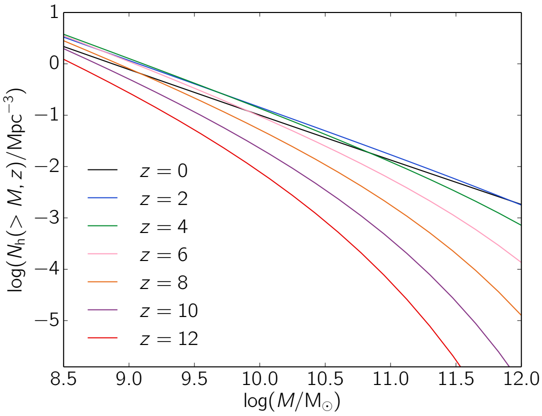

FIGURE 1.3: Cumulative halo mass function ($N_{\rm h}(> M, z)$) density as a function of halo mass (M). Calculation at different redshift are plotted with different colors. See the text for details

We can analytically infer the statistical properties of the collapsed objects (Press & Schechter, 1974). Such analysis – called Press-Schechter theory – can be conveniently given in terms of power spectrum $P(k)$, that describes the behavior of the perturbations and can be used to study the scale dependence of the growth of structure. $P(k)$ is defined as the autocorrelation function of the perturbation

$$P(k) = \left|\delta^2(k)\right|\,, \tag{1.46a}$$

where $\delta(k)$ is the Fourier transform of the density contrast. Additionally, it is convenient to define the dimensionless power spectrum

$$P^2_\Delta(k) = \frac{1}{2\pi^2} k^3 P(k) \tag{1.46b}$$

The power spectrum can calculated by solving eq.s 1.29 and 1.30. In Fig. 1.2 we plotted the solution for a WMAP7 cosmology (see later in this Sec. for a description of the redshift evolution).

To follow an analytical calculation, we eventually approximate the power spectrum with a power law of index n, i.e. $P \propto k^n$. Physically, n can be seen as related to the shape of the perturbation at the time it cross the horizon:

$$\delta_{t_{enter}}(k) \propto k^{\frac{n}{2}-2} \,. \tag{1.47}$$

For instance, if we are interested in perturbations that have developed during the radiation dominated era, these solutions grows as t for $k < k_H$ and are stable after passing the horizon. The primordial scale-free power spectrum is defined such that the dimensionless power spectrum (eq. 1.46b) is constant for $k > k_H$, i.e. $P_\Delta\left(k_H\right) = \text{const}$. The above eq. and the evolution of perturbations in the radiation dominated epoch rule that $n \simeq 1$, hence we could approximate the power spectrum as

$$P(k) \propto k \qquad \text{for} \qquad k \lesssim k_H \tag{1.48a}$$

$$P(k) \propto k^3 \qquad \text{for} \qquad k \gtrsim k_H \tag{1.48b}$$

The exact match between the two trends is given by analyzing the growth of the perturbations (see eq. 1.31) upon the passage from the radiation dominated era to the matter dominated epoch.

The estimate of the number of virialized structure can be given by smoothing the density field on the length scale corresponding to the non-linear mass. An order of magnitude estimate of this mass can be given by the mass contained in a sphere of radius the non-linear scale, i.e. $M_{nl} \sim \overline{\rho} k_{nl}^{-3}$, where k_{nl} is defined such that $P_\Delta\left(k_{nl}\right) = 1$. The non-linear scale can be seen in Fig. 1.2. Formally, the non-linear mass can be expressed by using the definition of square mass fluctuation enclosed in a sphere of radius R

$$\sigma^2 = \int \mathrm{d}^3k \widehat{W}^2(kR) P(k) \,, \tag{1.49}$$

where $\widehat{W}$ is the Fourier transform of the top hat function[5]. The mass-radius correspondence can be obtained via

$$M = \frac{4}{3}\pi\overline{\rho}R^3 \,, \tag{1.50}$$

thus the non-linear mass can be defined as

$$\sigma\left(M_{nl}\right) = \delta_c \,, \tag{1.51}$$

---

[5] Using different filter functions marginally alters the following results.

where δ_c is the density contrast of collapsed regions introduced early in this Sec.. Assuming $P \propto k^n$, then, the non-linear mass scales as

$$M_{nl} \propto t^{\frac{4}{3+n}} \tag{1.52}$$

Assuming that the initial perturbations are given by Gaussian density field (e.g. Padmanabhan, 1993), the probability P_c to have a mean overdensity higher than δ_c in the sphere of radius R is

$$P_c = \sqrt{\frac{2}{\pi}} \frac{1}{\sigma} \int_{\delta_c}^{\infty} \mathrm{d}\delta \exp\left(\frac{\delta^2}{2\sigma^2}\right) \tag{1.53}$$

and the number of collapsed object $\mathrm{d}N_\mathrm{h}$ per unit mass $\mathrm{d}M$ is thus

$$\mathrm{d}N_\mathrm{h} = \frac{\overline{\rho}}{M} \frac{\mathrm{d}P_c}{\mathrm{d}M} \mathrm{d}M \,. \tag{1.54}$$

Then, by inserting the non-linear mass (eq. 1.52), we have

$$\frac{\mathrm{d}N_\mathrm{h}}{\mathrm{d}M} = \left(1 + \frac{n}{3}\right) \sqrt{\frac{2}{\pi}} \frac{\overline{\rho}}{M^2} \left(\frac{M}{M_{nl}}\right)^{\frac{n-3}{6}} \exp\left(-\frac{1}{2}\left(\frac{M}{M_{nl}}\right)^{\frac{n+3}{3}}\right) , \tag{1.55}$$

that is the halo mass function expressed in term M_{nl}. The value of the constant $\delta_c = 1.686$ from linear theory have been successfully tested in many cosmological simulation (e.g. Norman, 2010). Eq. 1.55 can alternatively be seen in a cumulative form

$$N_\mathrm{h}(> M, z) = \int_M^{+\infty} \frac{\mathrm{d}N_\mathrm{h}}{\mathrm{d}M'} \mathrm{d}M' \,. \tag{1.56}$$

In Fig. 1.3 we have plotted the cumulative mass function for various redshift. The calculation does directly apply eq. 1.55: to compute the halo mass functions we adopted the transfer function from Eisenstein & Hu (1998) and a WMAP7 cosmology (Larson et al., 2011)

1.2 Numerical methods

Structure formation process is guided by non-linear equations, which are difficult to solve with an analytical approach. A direct method to follow the evolution of structure consist in using numerical methods. Several schemes of calculation are available in literature. Such schemes can be broadly divided into two category: particle-based and grid-based. The distinction consists in the frame of reference chosen for the dynamical equations, namely Lagrangian for particles and Eulerian for grids.

In principle, once a physical problem is chosen, different numerical implementations should yield similar results, within the numerical tolerance. As a matter of fact, to considered be reliable, codes must be tested against standard benchmarks; e.g. a code must correctly reproduce analytical solutions of gravitational problems and pass shock tube test of fluid dynamic.

However, when implementing refined physical processes in the calculations, several differences are present between the currently available cosmological codes, as analyzed in Scannapieco et al. (2012) and Kim et al. (2014). The former, the AQUILA project, is focused on the analysis of different cosmological numerical codes and their performance in large scale structure and star formation simulation. The latter, AGORA project, focus on the study of high resolution simulations of single galaxies by analyzing the differences between 9 codes.

An analysis of different implementations is beyond the aim of this Thesis. Nonetheless it is important to understand how numerical codes affects the physical problems we want to solve. Therefore, in this Sec. we give an overview of the codes mainly used in the Thesis, by reviewing their characteristics. We explain how the dynamic is solved with RAMSES (Teyssier, 2002), how we account for cooling and heating processes with ATON (Aubert & Teyssier, 2008) and how initial conditions can be generated with GRAFIC (Bertschinger, 2001).

1.2.1 Dynamical evolution

The code RAMSES (Teyssier, 2002) has a oct based Fully Threaded Tree data structure where the hydrodynamical Adaptive Mesh Refinement (AMR) scheme is coupled with improved particle mesh N-body solver, that compute the Poisson equation on a series of nested grids.

The computational space is divided in cells, and the basic elements of the code are octs. An oct is a group of 2^{dim} cells, where dim is the integer indicating the number of spatial dimensions. Octs can be labelled by the index l, which accounts for the level of refinement of the grid they belong to, being $l = 0$ the base Cartesian level. Each oct is double linked: to other octs of the same level l and to their parents and children at, respectively, the level $l-1$ and $l+1$. If a cell has children it is called a split cell, otherwise a leaf cell. To ensure a smooth transition between the different levels, for every oct to be refined its neighbors are also marked for refinement (see Fig. 1.4). Thus every children end up having $3^{dim}-1$ parents. Each particle that is inside the boundary of an oct belong to that oct and is linked to the other particles satisfying the same condition. Initially, the creation of this list is done storing the particles in the coarse grid level $l = 0$ and then recursively splitting them among the children octs up to the maximum chosen level of refinement $l = l_{max}$. This double-linked list structure is one of the main cause of memory overhead of AMR codes when compared to SPH codes.

The refinement criterion choice is based on the specific problem one wish to solve. The criteria can be characterized by requiring a certain precision for the difference of a variable between two adjacent cells (e.g. to optimize shock resolution) or by choosing a specific region to be refined. Cosmological simulations usually adopt a density threshold based refinement. It is named quasi-Lagrangian strategy, because the mass of every cell is forced to be (roughly) constant regardless of the refinement level. Alternatively single galaxy formation simulations typically use a Jeans strategy, refining a cell if its size exceed the local Jeans length.

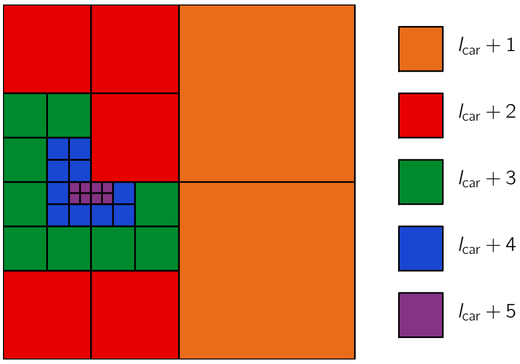

FIGURE 1.4: Example of a $dim = 2$ AMR oct tree structure. The Fig. shows a single coarse grid cell ($l = l_{\text{car}}$) as divided in finer level of refinement ($l_{\text{car}} + 1, \ldots, l_{\text{car}} + 5$). Note that only leaf cells are colored.

The time evolution is computed recursively starting from $l = 0$ to $l = l_{max}$. The first step is to generate the new refinement level $l{+}1$. This is done by interpolate conservatively level l variables: the particles are moved by testing the boundary of their parents, in this way avoiding to build the whole three from the base level at every time step. Then the time step Δt_l is chosen to be the minimum among the relevant scale. For a cosmological simulation these are the free fall time (t_{ff}), the crossing cell time and the Hubble time[6]. Additionally, the Courant Friedrich Levy (CFL) stability condition is applied, so that the time step at level l is determined by

$$\Delta t_l = \min \left\{ \begin{array}{ll} C_1 \min\limits_{l} t_{ff}, & C_2 \Delta x_l \left(\max\limits_{l} |\mathbf{v}_p| \right)^{-1}, \\ C_3 \dfrac{a}{\dot{a}}, & C_4 \Delta x_l \left(\max\limits_{l,j} v_j + c_s \right)^{-1} \end{array} \right. \tag{1.57}$$

where the C_i are order unity constants, c_s is the average sound speed. For fine level ($l > 1$) the constraint $\Delta t_l \leq \Delta t_{l-1}$ is imposed. After choosing the timestep the level $l + 1$ is advanced in time and Δt_l is synchronized with Δt_{l+1} accordingly to nature of the time step (single or adaptive). Then the boundary conditions for level l are generated. For the Cartesian mesh ($l = l_{\text{car}}$) these are determined a priori (e.g. periodic boundary conditions), while for the other levels l are recursively calculated from the solution of level

---

[6] For these conditions, only at high redshift the Hubble time is relevant, i.e. short enough.

$l-1$. Such solution is assumed to be constant during the mesh evolution. The proper reconstruction is done using an interpolation which is a generalization of the Min-Mod limiter. The conditions are stored in a temporary buffer, then the dynamic is computed, the new refinement map is constructed and the cycle is repeated.

Different techniques are used to solve the equations responsible for the baryons and the DM evolution. We can simplify the notation by dropping the level subscript, since we have seen that all the octs in a specific level are evolved at the same time. Note that, as RAMSES is thought as a multi-purpose program, the dynamical eq.s are not written directly for a cosmological environment. This setting is achieved using the so called super-moving coordinate[7]. It is a set of variable that has the property of transforming all but the Poisson equation in their relativistic counterpart without changing their functional form

$$\mathrm{d}\tilde{t} = \frac{H_0}{a^2}\mathrm{d}t \tag{1.58a}$$

$$\tilde{x}_i = \frac{1}{aL}x_i\,, \tag{1.58b}$$

where L is the size of the computational box. The computation starts by calculating the density field by using a Cloud In Cell (CIC) interpolation scheme. Particles of the level l are checked against the boundary of the mesh, then the particles of the parent octs at level $l-1$ are included if they intersect the volume considered. The density inferred in this way is equal to the density that would be obtained from a Cartesian mesh. Then, using the density, the Poisson equation can be solved

$$\Delta\tilde{\phi} = \frac{3}{2}a\Omega_m\left(\tilde{\rho}-1\right) \tag{1.59}$$

where $\tilde{\rho}$ is the density evaluated in the super-moving reference

$$\tilde{\rho} = \frac{a^3}{\Omega_m\rho_c}\rho \tag{1.60}$$

The Laplacian is approximated by a $2dim+1$ points finite difference. The solving approach used depends on the mesh level. The Cartesian ($l=l_{\mathrm{car}}$) level is solved with the fast Fourier transform, by using as Green function the Fourier transform of the approximated Laplacian. Finer levels are treated with the Gauss-Seidel relaxation method: first the potential is calculated solving the Dirichlet problem, then it is corrected using an over relaxation parameter; the cycle is repeated until the norm of the residual has been reduced by a chosen factor. The initial guess for the solution is provided by the linear

---

[7] This transformation is suitable in obtaining the general relativity eq.s of ΛCDM because the source of gravity are assumed to be non-relativistic. See e.g. Adamek et al. (2015) for a more general framework.

reconstruction of the potential for the level $l-1$. For $l > l_{\mathrm{car}}$, the computational volume may not be completely covered by the mesh, therefore a rule of thumb is used to calculate the optimal over relaxation parameter, in order to have the algorithm converging rapidly enough.

After calculating the gravitational potential, the following phase is to update each particle position (x_i^p) and their corresponding velocity (v_i^p). This is done via the following

$$\frac{\mathrm{d}}{\mathrm{d}t} x_i^p(t) = v_i^p(t) \tag{1.61a}$$

$$\frac{\mathrm{d}}{\mathrm{d}t} v_i^p(t) = -\nabla_i \phi(t) \tag{1.61b}$$

Firstly, the acceleration is computed by approximating the gradient with the 5-points finite difference. Then an inverse CIC scheme is used to interpolating back on the particles to be evolved, namely the ones whose cloud is within the level boundary.

Note that a cloud may be partially outside the volume of the mesh; for those particles the acceleration is interpolated from the coarser level. Once the acceleration at time t is known, the particles are evolved using the finite difference equivalent of eq.s 1.61. The evolution from time n to $n+1$ is obtained in two step:

$$\begin{array}{ll} \left\| \begin{array}{r} v_i^p\,(n+1/2) = v_i^p(n) - \dfrac{\Delta t}{2}\nabla_i\phi(n) \\ x_i^p(n+1) = x_i^p(n) + \Delta t\, v_i^p\,(n+1/2) \end{array} \right. & \text{prediction} \\ \quad v_i^p(n+1) = v_i^p\,(n+1/2) - \dfrac{\Delta t}{2}\nabla_i\phi(n+1) & \text{correction} \end{array}$$

It is important to note that the second step can only be completed when the new acceleration is computed. This allows to avoid an additional call of the Poisson solver, thus reducing the computational time. In the case of adaptive time step, a correct evolution implies that the evolutionary state of the particle must be known, thus requiring an additional integer in the particle data structure (which add overhead).

The fluid component is solved with the so-called MUSCL scheme, which is an acronym standing for Monotone Upstream-centered Scheme for Conservation Laws. The technique consists in discretizing the Euler eq.s of conservation

$$\partial_t \rho + \nabla_i \rho v_i = 0 \qquad \text{(mass)} \tag{1.62a}$$

$$\partial_t \rho v_i + \nabla_i \rho v_j v_i + \nabla_i P = -\rho \nabla_i \phi \qquad \text{(momentum)} \tag{1.62b}$$

$$\partial_t \rho e + \nabla_i \rho v_i \left(e + \frac{P}{\rho} \right) = -\rho v_i \nabla_i \phi \qquad \text{(energy)} \tag{1.62c}$$

where ρ, v_i, P and e are respectively the density, the velocity, the pressure and the internal energy per unit mass (for energy eq. see Sec. 1.2.2). The system closure is given by choosing an EOS

$$P = (\Gamma - 1)\left(e - \frac{1}{2}v^2\right)\rho \tag{1.62d}$$

and Γ is a constant adiabatic index. In the supermoving coordinates (eq.s 1.58) the hydrodynamical quantities must be slightly modified. The fluid density change as shown in in eq. 1.60, while the pressure and the velocity are transformed accordingly to the followings

$$\tilde{p} = \frac{a^5}{\Omega_m \rho_c H_0^2 L^2} \tag{1.63a}$$

$$\tilde{v}_i = \frac{a}{H_0 L} v_i \tag{1.63b}$$

As anticipated, using the supermoving coordinates does not modify the functional form of eq.s 1.62.

The advantage of using the conservative form is that eq.s 1.62 can be generalized as continuity equations for the variable $\mathcal{Q}$ and its associated flux $\mathcal{F}$, with the addition of a source $\mathcal{S}$ when needed (e.g. for Poisson equation): the discretization at the point j and time n of can be written as follows

$$\frac{\mathcal{Q}_j\left(n+1\right) - \mathcal{Q}_j\left(n\right)}{\Delta t} + \frac{\mathcal{F}_{j+1/2}\left(n+1/2\right) - \mathcal{F}_{j-1/2}\left(n+1/2\right)}{\Delta x} = \mathcal{S}_j\left(n+1/2\right) \, , \tag{1.64}$$

where at time $n + 1/2$ centered fluxes across cell interfaces are calculated with Godunov method (piecewise linear method). The multi-dimensionality of the calculation can be handled by directional splitting the operator of evolution.

To exemplify the concept (see Fig. 1.5), we focus on the 2 dimensional case with no source function ($\mathcal{S} = 0$, as for instance in the continuity eq. 1.62a). Then, using eq. 1.64, the temporal evolution of $\mathcal{Q}$ at the grid point (j, k) can be written as

$$\begin{aligned} \mathcal{Q}_{j,k}\left(n+1\right) = \mathcal{Q}_{j,k}\left(n\right) + & \frac{\Delta t}{\Delta x}\left(\mathcal{F}_{j+1/2,k}\left(n+1/2\right) - \mathcal{F}_{j-1/2,k}\left(n+1/2\right)\right) + \\ + & \frac{\Delta t}{\Delta y}\left(\mathcal{F}_{j,k+1/2}\left(n+1/2\right) - \mathcal{F}_{j,k-1/2}\left(n+1/2\right)\right) \end{aligned} \tag{1.65}$$

The hydrodynamic step is calculated at the end of the evolution loop. This mean that a single grid Godunov solver is used to calculate the fluxes. Each flux is computed using a iterative Riemann solver to yield the required precision at the contact discontinuity, averaged with near finer grid ones if necessary. These fluxes are used to update the variables of cell that have no children. Instead, split cells variables are calculated by averaging fluxes of the finer level.

1.2.2 Cooling and heating processes

RAMSES accounts for radiative (cooling and heating) processes via the solver ATON[8] (Aubert & Teyssier, 2008). It is important to note that this implementation does not solves simultaneously the dynamic and the radiation transfer, but rather act post processing the hydrodynamical output every time step and account for radiation by modifying the heating and cooling components in the energy equation. There are RAMSES version that have schemes coupling the dynamical evolution and radiation transfer, such as RAMSES-RT (Rosdahl et al., 2013), however these are not used in the present work.

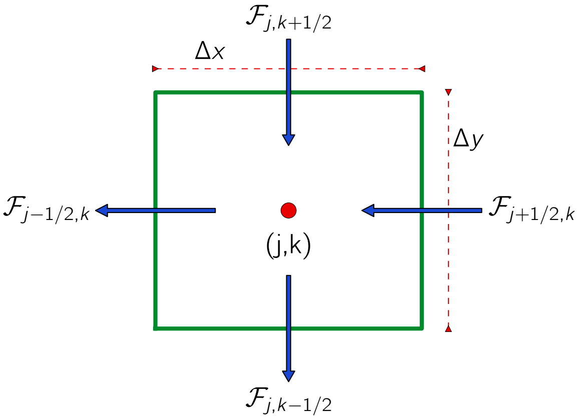

FIGURE 1.5: Sketch of the geometry for the hydrodynamic evolution in a 2-dimensional case (see eq. 1.65).

In ATON radiative transfer equation is handled by solving its moments and by adopting a closure condition. In terms of the specific intensity per unit of frequency $I^\nu = I^\nu(\mathbf{x}, \hat{n}, t)$, the equation of radiation written in the supermoving coordinate reads as in a non-relativistic environment

$$\left(\partial_t + l_i \nabla_i\right) I^\nu = -\kappa^\nu I^\nu + \frac{\mu^\nu}{\kappa^\nu} \tag{1.66}$$

where $\hat{l}$ is the line of sight versor, κ^ν the absorption coefficient and μ^ν the emission coefficient per unit of density. ATON accounts for the first two moments, that can be calculated in terms of the energy density E^ν, the flux, the K-moment and the source, i.e. μ^ν/κ^ν. If the source is isotropic, as for a diffuse UV background (e.g. Haardt & Madau, 1996, 2012) and for photons recombination, the only non vanishing term is the mean value

$$\int \mathrm{d}l \frac{\mu^\nu}{\kappa^\nu} = h\nu S^\nu = h\nu(\dot{N}_* + \dot{N}_{rec})\,, \tag{1.67}$$

where we separated the background term, $\dot{N}_*$, from $\dot{N}_{rec}$, which is due to recombination of ionized species. It is convenient to write the system in term of the photon number

---

[8] Alternative radiative and chemistry solver have been implemented for RAMSES, e.g. GRACKLE (Kim et al., 2014) and KROME (Grassi et al., 2014).

density $N^\nu = E^\nu(h\nu)^{-1}$, so that the moment eq.s can be written as

$$\hat{l}^0 \quad \mapsto \quad \partial_t N^\nu + \nabla_i F_i^\nu = -\kappa c N^\nu + S^\nu \tag{1.68a}$$

$$\hat{l}^1 \quad \mapsto \quad \partial_t F_j^\nu + \nabla_i K_{ij}^\nu = -\kappa c F_j^\nu \tag{1.68b}$$

To explain the method, it is sufficient to restrict to the case of pure hydrogen, as the scheme can be generalized to more of complicated mixtures following the same steps. We label with n^{HI} the neutral hydrogen number density and with σ^ν the photoionizzation cross section. Then, we can write the total absorption as

$$\kappa^\nu = n^{\mathrm{HI}}\sigma^\nu \tag{1.69}$$

It is therefore possible to solve the equations in term of the H I ionizing photons, namely by integrating for frequency greater than the ionizing threshold ν_{HI}

$$N^\gamma = \int_{\nu_{\mathrm{HI}}}^{\infty} \mathrm{d}\nu N^\nu \,. \tag{1.70}$$

Note that, when integrating with frequency the moment eq.s 1.68 the cross section terms are averaged one time with the number density and one with the flux, and the two are not equal in general. In our case these two average are nearly equal, by assuming a fixed reference radiation $J_0 = J_0(\nu)$ from which the averaged cross section can be precomputed

$$\sigma_\gamma = \left(\int_{\nu_{\mathrm{HI}}}^{\infty} \mathrm{d}\nu \sigma^\nu 4\pi (h\nu)^{-1} J_0\right)\left(\int_{\nu_{\mathrm{HI}}}^{\infty} \mathrm{d}\nu 4\pi (h\nu)^{-1} J_0\right)^{-1} \,. \tag{1.71}$$

Additionally we can substitute the source term $\dot{N}_{rec}$ making explicit the recombination coefficients α_A and α_B (e.g. Haehnelt et al., 2001), which take into account optically thin or thick line of sights, respectively

$$\dot{N}_{rec}^\gamma = \int_{\nu_{\mathrm{HI}}}^{\infty} \mathrm{d}\nu \dot{N}_{rec} = n_e n_{\mathrm{HII}}(\alpha_A - \alpha_B) \tag{1.72}$$

Using these relations the system 1.68 can be written as

$$\partial_t N^\gamma + \nabla_i F_i^\gamma = -n_{\mathrm{HI}}\sigma_\gamma c N^\gamma + \dot{N}_*^\gamma + n_e n_{\mathrm{HII}}(\alpha_A - \alpha_B) \tag{1.73a}$$

$$\partial_t F_j^\gamma + \nabla_i K_{ij}^\gamma = -n_{\mathrm{HI}}\sigma_\gamma c F_j^\gamma \tag{1.73b}$$

To further the analysis, we must compute the hydrogen ionization fraction. This is given by the detailed balance of the process

$$\partial_t n_{\mathrm{HI}} = \alpha_A n_e n_{\mathrm{HII}} \beta n_e n_{\mathrm{HI}} - c\sigma^\gamma N^\gamma n_{\mathrm{HI}} \,. \tag{1.74}$$

In the hydrogen only case, we are further constrained by

$$n_e = n_{\mathrm{HII}} \tag{1.75a}$$

$$n_{\mathrm{HI}} + n_{\mathrm{HII}} = n_{\mathrm{H}} \, (= \mathrm{constant}) \tag{1.75b}$$

The energy equation must be consistently accounted for. Hence we re-write RAMSES eq. 1.62c in term of the heating ($\mathcal{H}$) and the cooling rate ($\mathcal{L}$)

$$\rho \partial_t e_{int} = \mathcal{H} - \mathcal{L} \tag{1.76}$$

where e_{int} is the internal energy per unit density. Here, heating is given by the photoionizzation[9]

$$H = n_{\mathrm{HI}} hc \int_{\nu_{\mathrm{HI}}}^{\infty} \mathrm{d}\nu \, (\nu - \nu_{\mathrm{HI}}) \, \sigma N \, , \tag{1.77}$$

while cooling is given by the sum of the recombination, collisional ionization and bremsstrahlung (e.g. Maselli et al., 2003). To solve the eq.s, the momentum system must be closed. To this aim, we express the Eddington tensor with a specific functional form:

$$D_{ij} = \frac{c^2}{N} K_{ij} \tag{1.78}$$

The relevant assumption in ATON is that the radiation angular distribution is axisymmetric around the flux, which we can write as

$$F_i = (cNf) \, \hat{u}_i \tag{1.79}$$

where f is the norm of the reduced flux. Using the last eq., the Eddington tensor assumes the form

$$D_{ij} = \frac{1-\chi}{2} \delta_{ij} + \frac{3\chi - 1}{2} u_i u_j \tag{1.80}$$

where χ is a factor to be determined. The isotropic component δ_{ij} is due to diffuse radiation. This is separated from free streaming component, that is aligned with flux direction $\hat{u}$. Thus eq. 1.80 describes the intermediate case between a purely diffuse and a purely streaming radiation, by approximating the situation with a linear combination of the two components. Until this point, the functional dependence of the Eddington factor $\chi = \chi(f)$ is constrained only by

$$\frac{1}{3} \leq \chi \leq 1 \tag{1.81}$$

Here, the M1 model (Aubert & Teyssier, 2008) is further assumed. It corresponds to the angular distribution of a isotropic radiation Lorentz boosted along $\hat{u}$, that is similar to

---

[9] Additional heating processes, e.g. SN feedbacks, are considered in the following Chapters.

the case of the CMB dipole.

$$\chi = \frac{3+4f^2}{5+2\sqrt{4-3f^2}} \tag{1.82}$$

The code implementation is achieved by successive steps: first the number of ionizing photon is updated in time for every cell, then the source-less hyperbolic moment system (eq.s 1.73) is solved and finally the thermo-chemical step is computed. The latter step refers to the balancing of the right hand side of eq.s 1.73a and 1.73b, that is solved accordingly to the heating ($\mathcal{H}$) and cooling ($\mathcal{L}$) evolution.

The actual numerical implementation – e.g. operator splitting technique, etc – is similar to the discretization of fluid equation described for the hydrodynamic of RAMSES. Therefore – similarly to eq. 1.64 – the discretization of the coupled eq.s 1.73 for time n and at the point i can be written as

$$\frac{\mathcal{Q}_i\left(n+1\right)-\mathcal{Q}_i\left(n\right)}{\Delta t}+\frac{\mathcal{F}_{i+\frac{1}{2}}\left(m\right)-\mathcal{F}_{i-\frac{1}{2}}\left(m\right)}{\Delta x}=0 \tag{1.83}$$

where $\mathcal{Q}$ can represent either N or F_i, while $\mathcal{F}$ the associated flux F_i or K_{ij}, respectively. The aspect worth being highlighted is the choice for time resolution. The time m is selected accordingly to the solving scheme: it can be explicit, fixing $m=n$, or implicit, namely $m=n+1$. Choosing a scheme gives different constraint on the time step Δt and the solving method for the flux at time m.

Using the implicit scheme is computational costly and difficult to implement, while an explicit scheme yields a thigh constraint on the time step. The solution considered in ATON consist in adopting the latter scheme, by additionally using a relaxed condition for the time step selection. The flux at time n evolve at time $n+1$ following (e.g. González et al., 2007)

$$\mathcal{F}_{i+\frac{1}{2}}\left(n\right)=\frac{1}{2}\left(\mathcal{F}_{i+1}\left(n\right)+\mathcal{F}_i\left(n\right)\right)-\frac{c}{2}\left(\mathcal{Q}_{i+1}\left(n\right)-\mathcal{Q}_i\left(n\right)\right)\,, \tag{1.84}$$

where the c factor arises because the maximum speed of wave propagation has been taken equal to the speed of light. The CFL condition on the time step would imply

$$\Delta t < \frac{1}{3}\frac{\Delta x}{c}\,. \tag{1.85}$$

However, in the cosmological environment, eq. 1.85 would rule a time interval much smaller than the actual dynamical time scale (see eq. 1.57), thus greatly augmenting the computational time. The solution chosen is to replace the speed of light in all of the radiative transfer equations considered so far with effective speed of light c_{eff}, typically in the range

$$10^{-3} < \frac{c_{\rm eff}}{c} < 1$$

This approximation has been tested in various cases. For our current purpose, it gives no relevant errors respect to a more refined radiative transfer treatment. However, this condition for the time step calculation cannot be used for the energy equation. The energy equation is substituted by the system of coupled equations for the evolution of the temperature and of the ionization fraction. In order to recover the correct evolution, the calculation of the energy is performed within every radiative transfer main step as a subcycle, with a time step of the order of the cooling time scale[10].

1.2.3 Cosmological initial conditions

Cosmological initial conditions can be generated using the results of linear perturbation theory. In the past, GRAFIC (Gaussian RAndom Field Initial Conditions Bertschinger, 2001) has been the main publicly available software used to generate initial condition. Now, an updated version of the program is available, i.e. MUSIC (MUlti-Scale Initial Conditions Hahn & Abel, 2011). Both GRAFIC and MUSIC follow the same approach, differences mainly consist in code implementation. Such differences are perceivable only when generating initial conditions for zoom-in simulations. Since zoom-in simulations are outside the aim of the present work, we can restrict our overview to GRAFIC without loss of generality.

The underlying concept (see Sec. 1.1.4) is that it is possible to generate a perturbation for the matter component on various scale lengths with periodic boundary using the transfer function method (e.g. Dodelson, 2003). The perturbations are therefore calculated by convolving the transfer function $\mathcal{T}$ with a Gaussian white noise ζ

$$\delta\left(\mathbf{x}\right) = \int \mathrm{d}\mathbf{y} \zeta\left(\mathbf{y}\right) \mathcal{T}\left(\left|\mathbf{x}-\mathbf{y}\right|\right) \ . \tag{1.86}$$

As the noise is uncorrelated, the associated power spectrum is – almost by definition – given by

$$\left\langle \zeta\left(\mathbf{x}\right) \zeta\left(\mathbf{y}\right) \right\rangle = (2\pi)^3 \delta_d\left(\mathbf{x}-\mathbf{y}\right) \ , \tag{1.87}$$

whereδ_d is the three-dimensional Dirac delta function. The amplitude of the fluctuations are described by the power spectrum $P(k)$ in term of $\mathcal{T}$ as $P(k) \propto \mathcal{T}^2$ (as in eq. 1.31), and we usually adopt the transfer function described in Eisenstein & Hu (1998) (see Fig. 1.2).

---

[10] See Grassi et al. (2014) for the details of the numerical implementation and the performance analysis of complex chemical networks.

In eq. 1.31, the proportionality constant for $P(k)$ can be given in term of the value of $\sigma_8 \equiv \sigma(R = 8\,\mathrm{Mpc}\,h^{-1})$ (see eq. 1.49), namely the standard deviation of the mass distribution over 8 comoving Mpc. The evolution of the perturbations (Bertschinger, 1995) is achieved by interpolating $P(k)$ in the scale range of interest and they are evolved in time up to the starting redshift chosen for the simulation.

CHAPTER 2

SIMULATING COSMIC METAL ENRICHMENT IN HIGH REDSHIFT GALAXIES

Cosmological numerical simulations have been extensively used to study cosmic metal enrichment (Aguirre & Schaye, 2007, Johnson, 2013). However, the huge dynamical range of the underlying physical phenomena makes a true auto-consistent simulation impossible. A viable modelization can be achieved by using subgrid models. These depend both on the considered physics and code implementation. Recently, Hopkins et al. (2013) studied the impact of different star formation criteria, Agertz et al. (2013) and Vogelsberger et al. (2013) analyzed the effect of including different kind of feedback, and the AQUILA project (Scannapieco et al., 2012) compared 13 different prescriptions of the main used cosmological codes. Subgrid modelling lessens the burden of the large dynamical range, but given the currently available computational capabilities the numerical resources have to be focused toward either the small or the large scales.

Simulations of small cosmic volumes, i.e. box sizes $\lesssim$ Mpc h^{-1}, concentrate the computational power and allow the usage of highly refined physical models. Greif et al. (2010) studied the transition from Pop III to Pop II stars in a $10^8 \mathrm{M}_{\odot}$ galaxy at $z \sim 10$ assessing the role of radiative feedback; Maio et al. (2010) analyzed the same transition by varying several parameters, such as the critical metallicity $\mathrm{Z}_{\mathrm{crit}}$ that distinguishes the populations, the initial mass function (IMF), the metal yields and the star formation threshold; Xu et al. (2013) focalized on pinpointing the remnant of Pop III at high redshift, by employing the same computational scheme of Wise et al. (2012), which analyzed the impact of radiation from first stars on metal enrichment at $z \gtrsim 9$; at the same redshift, Biffi & Maio (2013), using an extensive chemical network, studied the properties and the formation of first proto-galaxies.

Large scale ($\gtrsim 5\,\mathrm{Mpc}\,h^{-1}$) cosmological simulations naturally allows for a fair comparison with the observations. Scannapieco et al. (2006) showed that observation of line of sight (l.o.s.) correlations of C IV and Si IV are consistent with a patchy IGM enrichment, confined in metal bubbles of $\sim 2\,\mathrm{Mpc}\,h^{-1}$ at $1.5 \lesssim z \lesssim 3$; by implementing galaxy outflows driven by a wind model Oppenheimer & Davé (2006) managed to reproduce the flatness of $\Omega_{\rm CIV}$ at $2 \lesssim z \lesssim 5$; Tornatore et al. (2007) found evidence of Pop III production at $z \gtrsim 4$, hinting at the possibility of observing metal-free stars; using a galactic super wind model Cen & Chisari (2011) simulated a 50 Mpc h^{-1} box finding, among other results, a good agreement with observations for $\Omega_{\rm CIV}$ and a reasonable match for $\Omega_{\rm OVI}$; by using a $(37.5\,\mathrm{Mpc}\,h^{-1})^3$ volume simulation evolved up to $z = 1.5$, and considering different IMFs and feedback mechanisms, Tescari et al. (2011) analyzed the evolution of $\Omega_{\rm CIV}$ and statistics of H I and C IV absorbers at different redshifts; simulating a box with size of $25\,\mathrm{Mpc}\,h^{-1}$ and including various feedback, Vogelsberger et al. (2013) managed to match several observations, as the SFR and stellar mass density (SMD) evolution for $z \lesssim 9$, the galaxy stellar mass function and mass-metallicity relation at $z = 0$.

The aim of this Chapter is to model the IGM metal enrichment focusing on high redshift ($z \geq 4$) by simulating a volume large enough to include a statistically significant ensemble of galaxies. Clearly, the trade off consists in a limitation of the resolution and small scale complexity that can be investigated. Our modelling approach is to limit the number of free parameters of the subgrid prescriptions and constrain them with first galaxies observations, namely both global SFR densities inferred from Ultraviolet (UV) luminosity functions (Bouwens et al., 2012, Zheng et al., 2012) and SMD from stellar energy density fitting (González et al., 2011). This method limits the uncertainty on the feedback prescriptions (e.g. Vogelsberger et al., 2013), and at the same time it allows a large scale analysis of the metal enrichment process.

The Chapter structure is the following. In Sec. 2.1, we describe the numerical implementation of the cosmological simulations whose free parameters are then calibrated by matching SFR and SMD data in Sec. 2.2. Sec. 2.3 and Sec. 2.4 contain the analysis of galactic and IGM metal enrichment, respectively. We devote Sec. 2.5 to study the effects of varying the Pop III IMF, and in Sec. 3.2 we compute and discuss mock QSO absorption spectra, in preparation for a future detailed comparison recent of high redshift ($4 \lesssim z \lesssim 6$) absorption line data (D'Odorico et al., 2013). Finally, in Sec. 3.4 we present our conclusions.

$\log(Z/Z_\odot)$	Y	R	$\epsilon_{\rm PopII}$
-4.0	0.0160	0.4680	10^{50}
-2.0	0.0192	0.4705	10^{50}
-1.0	0.0197	0.4799	10^{50}
0.0	0.0253	0.4983	10^{50}

Table 2.1: Adopted IMF-averaged Pop II metal yields and gas return fractions (van den Hoek & Groenewegen (1997) for $0.8 \leq m/{\rm M}_\odot \leq 8$ and Woosley & Weaver (1995) for $8 \leq m/{\rm M}_\odot \leq 40$); explosion energies (in ${\rm erg}\,{\rm M}_\odot^{-1}$) are taken from Woosley & Weaver (1995).

IMF	Y	R	$\epsilon_{\rm PopIII}/\epsilon_{\rm PopII}$
SALP	0.0105	0.46	1
FHN	0.0081	0.76	1
PISN	0.1830	0.45	10

Table 2.2: Adopted IMF-averaged Pop III metal yields and gas return fractions, and relative explosion energies. Data are taken from van den Hoek & Groenewegen (1997) for $0.8 \leq m/{\rm M}_\odot \leq 8$ and Woosley & Weaver (1995) for $8 \leq m/{\rm M}_\odot \leq 40$ for SALP, Kobayashi et al. (2011) for FHN, and Heger & Woosley (2002) for PISN.

2.1 Cosmological simulations

We perform cosmological simulations using a customized version of the publicly available code RAMSES (Teyssier, 2002), which is a Fully Threaded Tree (FTT) data structure in which the hydrodynamical Adaptive Mesh Refinement (AMR) scheme is coupled with a Particle Mesh (PM3) N-body solver through a Cloud-In-Cell interpolation scheme to compute the Poisson equation.

Our simulation evolves a $10\,h^{-1}$ comoving Mpc box, with 512^3 dark matter (DM) particles. The DM mass unit is $2.06 \times 10^6\,\Omega_{dm}\,h^{-1}{\rm M}_\odot$, and the baryon base grid spatial resolution is $19.53\,h^{-1}$ kpc. We allow for 4 additional refinement levels, with a Lagrangian mass threshold-based criterion. This enables us to reach a maximum resolution of $\Delta x_{\rm min} = 1.22\,h^{-1}$ kpc in the densest regions. The initial conditions are generated at $z = 199$ using GRAFIC (Bertschinger, 2001) and by adopting a WMAP7 cosmology[1]. The gas is characterized by a mean molecular weight $\mu = 0.59$ and has a primordial BBN composition ($Z = 0$) at the starting point of the simulation. We refer to metallicity as the sum of all the heavy element species without differentiating among them, as instead done, e.g., by Maio et al. (2007).

To account for heating and cooling processes RAMSES is coupled with ATON (Aubert & Teyssier, 2008), a moment-based radiative transfer code including metal cooling (Sutherland & Dopita, 1993, Theuns et al., 1998). The code allows the treatment of an external,

---

[1] Hereafter we assume a ΛCDM cosmology with $\Omega_\Lambda = 0.727$, $\Omega_{dm} = 0.228$, $\Omega_b = 0.045$, ${\rm H}_0 = 100$ h km ${\rm s}^{-1}$ ${\rm Mpc}^{-1}$, h $= 0.704$, $n = 0.967$, $\sigma_8 = 0.811$ (Larson et al., 2011).

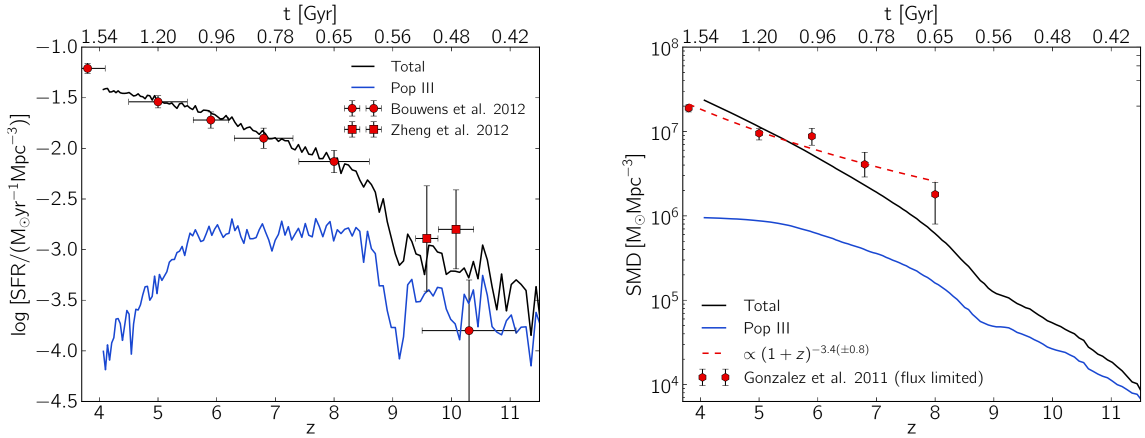

FIGURE 2.1: *Left panel:* Cosmic star formation rate density (SFR) as a function of redshift (age of the Universe) for all stellar populations (black line) and for Pop III stars only (blue line). Data points (in red) are taken from Bouwens et al. (2012) and Zheng et al. (2012). *Right:* Cosmic stellar mass density (SMD) as a function of redshift for all stellar populations (black line) and for Pop III stars only (blue line). Data points and the analytical fit (both in red) are from González et al. (2011).

redshift dependent UV background (UVB, e.g. Haardt & Madau, 1996, 2012) produced by both stars and QSOs. In the simulation we include the UVB and we neglect the radiation from sources inside the box, as the scale of ionized bubbles becomes rapidly comparable to the size of the simulation box (e.g. Wyithe & Loeb, 2004, Zahn et al., 2011) and therefore the derived reionization history could not be considered as reliable anyway. We have however verified that varying the UVB within observational limits[2] only marginally affects the enrichment history.

2.1.1 Star formation prescription

We adopt the star formation recipe described in Rasera & Teyssier (2006) and Dubois & Teyssier (2008), hereafter DT8, whose main features are recalled below. At each coarse time step, Δt, a collisionless star particle is created in every gas cell of size Δx which has a density ρ exceeding the threshold $\rho_{\rm th} \equiv 0.1\, m_H\, {\rm cm}^{-3}$ (Schaye, 2004), where m_H is the proton mass. The mass of the newborn particle is $M_{\rm s} = m_\star N$, where[3] $m_\star = \rho_{\rm th}\,(\Delta x_{\rm min})^3$ is the resolution dependent minimum mass of a star particle, and N is drawn from a Poisson distribution

$$P(N) = \frac{\langle N \rangle}{N!} \exp\left(-\langle N \rangle\right) \,, \tag{2.1a}$$

---

[2] We have used a simple analytical form of the UV background (Theuns et al., 1998) and varied its parameters.

[3] Following DT8 we impose that no more than half of a cell mass can be converted into stars, i.e. $M_{\rm s} = \min[m_\star N, 0.5\,\rho(\Delta x)^3]$. This prescription ensures the numerical stability of the code.

of mean $\langle N \rangle$ given by

$$\langle N \rangle = \frac{\rho\,(\Delta x)^3}{m_\star}\frac{\Delta t}{t_\star}\,; \tag{2.1b}$$

$t_\star$ is the local star formation timescale and represents the first free parameter of our model. The dynamical properties of the star particle formed are inherited from the spawning cell; if the gas cell metallicity is below (above) the critical metallicity, $\mathrm{Z_{crit}} \equiv 10^{-4}\mathrm{Z}_\odot$, we label the particle as belonging to the Pop III (Pop II) population. Such distinction is used when determining the metal yield and supernova explosion energy (Sec. 2.1.2).

This recipe ensures that the local SFR follows a Schmidt-Kennicutt relation (Kennicutt, 1998, Schmidt, 1959)

$$\dot{\rho}_\star = \frac{\rho}{t_\star}\Theta\left(\rho - \rho_{\rm th}\right)\,, \tag{2.2}$$

where Θ is the Heaviside function[4]. Hereafter, we define as “star forming” those cells satisfying the density criterion $\rho > \rho_{\rm th}$. As highlighted in Hopkins et al. (2013), different definitions[5] of star forming regions result in similar star formation histories, provided that stellar feedback is also included.

2.1.2 Feedback and enrichment prescriptions

The standard RAMSES feedback prescription takes into account both thermal and momentum-driven feedback, as described in DT8. Momentum-driven feedback related to supernova blastwaves is important on the typical scales ($\sim$ pc) reached by these structures (Agertz et al., 2013); similar arguments apply to radiative feedback from star forming regions. Since such small scales are not adequately resolved in our simulations, we decided to only include thermal feedback. Also, we do not include AGN feedback, which is thought to regulate the star formation of objects with masses $\gtrsim 10^{12}\mathrm{M}_\odot$ (e.g. Teyssier et al., 2011, Vogelsberger et al., 2013) that are rare or absent in our relatively small box.

Every newly-born star particle of mass $M_{\rm s}$ immediately prompts a SN event. This assumption corresponds to the so-called Instantaneous Recycling Approximation (Tinsley, 1980), in turn consistent with the adopted coarse time step ($\Delta t \sim 10$ Myr). SN explosions damp a thermal energy $E_{\rm sn}$

$$E_{\rm sn} = \eta_{\rm sn}\epsilon_{\rm sn}M_{\rm s}\,, \tag{2.3}$$

---

[4] Note that the Schmidt-Kennicutt relation is written in terms of the surface density while eq. 2.2 considers the volume density. Thus we are implicitly assuming a smoothing scale which makes $t_\star$ resolution-dependent.

[5] Other definitions generally used to identify star forming regions are based on temperature or molecular hydrogen fraction thresholds, convergent flows requirement or Jeans instability criterion.

where $\epsilon_{\rm sn}$ is the total SN energy per stellar mass formed and $\eta_{\rm sn}$ is the coupling efficiency. While $\epsilon_{\rm sn}$ depends only on the stellar population properties, $\eta_{\rm sn}$ depends on the numerical implementation and resolution; in practice, we consider $\eta_{\rm sn}$ as the second free parameter of our model. As noted in Dalla Vecchia & Schaye (2012) (see also Chiosi et al. 1992) considering purely thermal feedback is a good assumption if the gas is able to transform the additional thermal energy into kinetic energy before cooling; this can be mimicked by a sufficiently large coupling efficiency $\eta_{\rm sn} \gtrsim 0.1$.

Every explosion returns a gas mass $R\,M_{\rm s}$ and a metal mass $Y\,M_{\rm s}$, that are then removed from the star particle mass. Following Salvadori et al. (2007, 2008), and differently from DT8, we use metallicity dependent return fractions (R) and metal yields (Y):

$$R = \frac{1}{\langle\Phi\rangle}\int_{m_1}^{m_2}(m-w)\,\Phi\,{\rm d}m \tag{2.4a}$$

$$Y = \frac{1}{\langle\Phi\rangle}\int_{m_1}^{m_2} m_Z\Phi\,{\rm d}m \tag{2.4b}$$

with

$$\langle\Phi\rangle = \int_{m_1}^{m_2} m\Phi\,{\rm d}m\,, \tag{2.4c}$$

where $w = w(m, Z)$ and $m_Z = m_Z(m, Z)$ are respectively the stellar remnant and the metal mass produced by a star of mass m at a given metallicity, and $\Phi = \Phi(m)$ is the IMF. Both the IMF and the integration limits depend on the stellar population (Pop III or Pop II) considered.

The adopted Pop II (Pop III) metal yields, gas return fractions, and explosion energies are shown in Tab. 2.1 (Tab. 2.2). For Pop II stars, we adopt a Larson-Salpeter IMF (Larson, 1998), with[6] $m_1 = 0.1\,{\rm M}_\odot$, $m_2 = 100\,{\rm M}_\odot$, following Salvadori et al. (2007). The IMF of Pop III stars is very poorly constrained (e.g. Scannapieco et al., 2003). Therefore, we consider three different possibilities: (a) the same Larson-Salpeter IMF (referred to as the SALP case) as Pop II stars but with R, Y and $\epsilon_{\rm sn}$ calculated for $Z = 0$; (b) a δ-function IMF, i.e. $\Phi = \delta(m - m_0)$, with $m_0 = 25\,{\rm M}_\odot$ appropriate for faint hypernovae (FHN) (Salvadori & Ferrara, 2012); (c) a top-heavy IMF with $m_1 = 100\,{\rm M}_\odot$ and $m_2 = 500\,{\rm M}_\odot$ allowing for pair-instability SN (PISN) in the mass range $140\,{\rm M}_\odot \leq m \leq 260\,{\rm M}_\odot$ (Tornatore et al., 2007).

Throughout the Chapter we use the SALP case as the fiducial one; Sec. 2.5 is devoted to the analysis of different prescriptions IMF.

---

[6] With respect to a Salpeter IMF, a Larson IMF has an exponential cut below $m = 0.35\,{\rm M}_\odot$.

2.2 Cosmic star formation history

As explained above, our model contains two free parameters, namely the local star formation time, $t_\star$, and the supernova coupling efficiency, η_{sn}. These parameters have important effects (Rasera & Teyssier, 2006) on two observable quantities, the cosmic SFR and SMD as a function of redshift. Broadly speaking, $t_\star$ variations shift the SFR curve with respect to the horizontal axis (i.e., redshift), while η_{sn} sets the curve slope. Thus, in order to calibrate these unknowns, we require our simulation results to match the observed cosmic SFR (Bouwens et al., 2012, Zheng et al., 2012) and SMD (González et al., 2011).

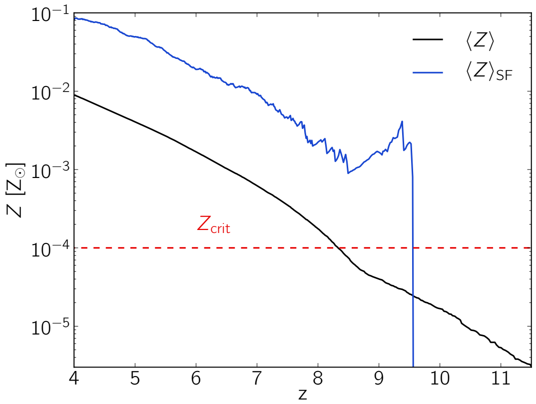

FIGURE 2.2: Redshift evolution of the mean metallicity of baryons, $\langle Z\rangle$, (black line) and the mean metallicity of star forming regions only, $\langle Z\rangle_{\rm SF}$, (blue line). The adopted value, $Z_{\rm crit} = 10^{-4}Z_\odot$, of the critical metallicity for the Pop III - Pop II transition is indicated with a dashed red line.

The evolution of the cosmic SFR and SMD for the best-fitting subgrid model parameters $t_\star = 7.5$ Gyr and $\eta_{\rm sn} = 0.25$ are shown in Fig. 2.1, where they are also compared to the above mentioned observations. The simulated SFR reproduces the data quite accurately in the range $4 \leq z \leq 8.5$; the agreement is still good at higher redshift ($9 \leq z \leq 10.5$), where, however, the limited mass resolution of our simulation yields a fluctuating SFR evolution. For the SMD evolution the agreement is good, although the predicted slope appears slightly steeper than the observed one (dashed red line). However, our predictions lie within 2-σ of the data by González et al. (2011). This level of agreement can be considered as satisfactory. In fact, while the SMD is inferred using Spectral Energy Distributions fitting of a flux-limited sample of galaxies, in our work the SMD is obtained simply by integrating the SFR. Our procedure then includes both stars and their remnants, regardless of the age.

In Fig. 2.1, we also plot separately the contribution of Pop III stars to both SFR and SMD. The Pop III SFR initially climbs to a level slightly above $10^{-3}\mathrm{M}_\odot\ \mathrm{yr}^{-1}\ (\mathrm{Mpc}\ h^{-1})^{-3}$ at $z = 9$ which is sustained until $z \simeq 6$ (which might then represent a sweet spot for experimental searches); beyond this epoch, Pop III star formation is rapidly quenched. Pop III SFR is always subdominant with respect to the Pop II one; however, at $z = 9$ the Pop III rate is smaller only by a factor $\simeq 10$. This finding offers new hope for detecting these elusive stars in the near future, and particularly with JWST which is expected to be able to probe Pop III supernovae up to $z \simeq 15$ (e.g. Whalen et al., 2013, de Souza et al., 2013).

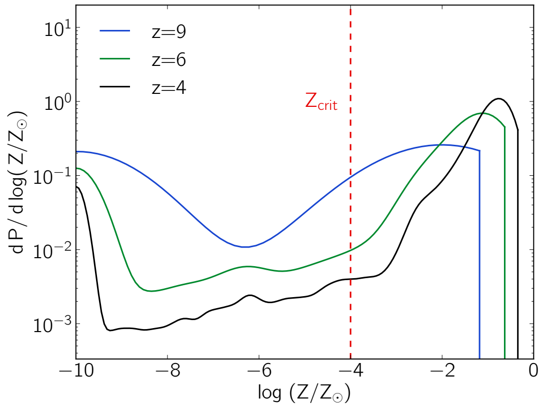

FIGURE 2.3: Stellar metallicity distribution function (MDF) at $z = 9$ (blue line), $z = 6$ (green line) and $z = 4$ (black line) for all stars in the simulation box. As in Fig. 2.2 the critical metallicity $Z_{crit} = 10^{-4} Z_\odot$ is indicated with a dashed red line. The amplitude of each curve is normalized so that its integral over the available Z range is equal to 1. Note that for display reasons we have set $Z = 10^{-10} Z_\odot$ for stars with $Z < 10^{-10} Z_\odot$.

Currently, observations of the He II λ1640 emission line, excited by the hard UV spectra of Pop III stars, can be used to infer upper bounds on Pop III star formation. Cassata et al. (2013) estimate a $\mathrm{SFR}_{\mathrm{PopIII}} \lesssim 10^{-6} \mathrm{M}_\odot\ \mathrm{yr}^{-1} \mathrm{Mpc}^{-3}$ at $z \simeq 2.5$. While our simulations cannot be carried on beyond $z = 4$ due to the limited volume, the upper limit is well above our simulated curve already at $z = 4$. Cai et al. (2011) used a WFC3/F130N IR narrowband filter to probe He II λ1640 emission in the galaxy IOK-1 at $z = 6.96$. The detected He II flux $1.2 \pm 1.0 \times 10^{-18}$ erg s^{-1} cm^{-2}, corresponds to a 1-σ upper limit on Pop III SFR of 0.5 $\mathrm{M}_\odot$ yr^{-1} in this galaxy (assuming a Salpeter IMF for this population) and representing $<$ 6% of the total star formation. If these figures are representative of the cosmic average, they would be in striking agreement with our results that predict at $z = 6.96$ a Pop III to Pop II SFR ratio of 7.8%. While this extrapolation to large scales might be unwarranted, the consistency we find might hint at the fact that current experiments are on the verge of tracing the full star formation history of metal-free stars. Resolution effects might affect Pop III SFR; they are discussed in detail in Appendix A.

The overall Pop III evolution is not dissimilar from that found by some previous dedicated studies (Johnson et al., 2013, Tornatore et al., 2007, Wise et al., 2012); however, we derive a Pop III SFR which is about one order of magnitude higher with respect to the results by Wise et al. (2012) and Johnson et al. (2013). At present the source of the discrepancy is unclear as it might be caused by numerical resolution, feedback treatment or limited volume effects. We will come back to this point in Sec. 2.3 and 2.5.

The first Pop III stars in our simulation start to form in relatively biased regions at $z \simeq 15$. We do not attach a particular significance to this epoch as it is well known that it might depend strongly on the numerical resolution adopted. Earlier studies (e.g. Fialkov et al., 2012, Gao et al., 2010, Naoz et al., 2006, Salvadori et al., 2014, Trenti &

Stiavelli, 2009) have in fact shown that the first stars in the Universe might form as early as $z \simeq 60$. Instead, it is worth noticing that in the same region after only ~ 200 Myr the star formation mode has turned into Pop II stars. This shows that even a relatively modest Pop III star formation burst is sufficient to enrich the surrounding gas above $Z_{\rm crit}$, as noted in previous works (e.g. Greif et al., 2010, Salvadori et al., 2008, Scannapieco et al., 2003, Wise et al., 2012) and further elaborated in Sec. 2.3.1.

In the following, we focus on the results specifically concerning cosmic metal enrichment. To improve the clarity of the presentation it is useful to discuss the problem separately for galaxies, the circumgalactic medium (CGM) and the intergalactic medium. The exact definitions of these components will be given in Sec. 2.4. Albeit this classification might be somewhat arbitrary, there is a clear differentiation among these environments in terms of density and physical processes. We then start by analyzing the metal enrichment of galaxies.

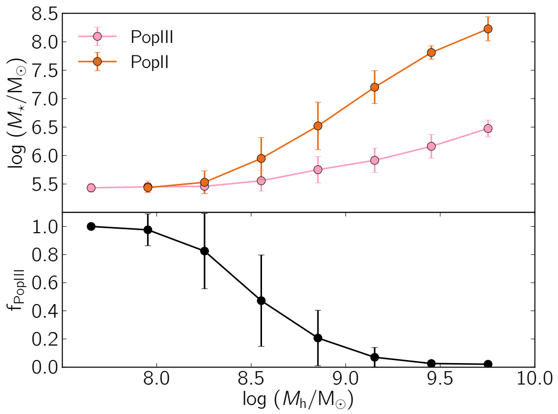

FIGURE 2.4: Stellar mass content as a function of the hosting halo mass at $z = 6$. *Upper panel*: mass in Pop II (orange line) and in Pop III (pink line) stars. *Lower panel*: the fraction of Pop III stars (black line), as defined in the text. The data has been binned in mass (log $M/\mathrm{M}_\odot \simeq 0.3$). Errorbars show the 1-$\sigma$ deviations within the bin.

2.3 Galaxies

We identify galaxies and their hosting halo in each simulation snapshot with the method detailed in Appendix C. In brief, we use a Friend-of-Friend algorithm to identify both DM halos and the associated star forming regions; the latter are characterized by the condition that the gas has on overdensity $\Delta \equiv \rho/\langle\rho\rangle > \Delta_{\rm th} \equiv \rho_{\rm th}/\langle\rho\rangle$. We checked that the inferred cumulative halo mass functions are in agreement with the analytical one (Press & Schechter, 1974, Sheth & Tormen, 1999) to better than 5% at all masses and redshifts. This is about the maximum precision achievable from halo-finder codes (e.g. Knebe et al., 2013).

As expected (Christensen et al., 2010, Wise et al., 2012), stars do not form in halos resolved with less then $\sim 10^2$ particles, i.e. $M_{\rm h} \simeq 10^{7.5}\mathrm{M}_\odot$. However, physical arguments for star formation suppression in low mass (mini) halos have been given in several theoretical (Alvarez et al., 2012, Haiman & Bryan, 2006) and numerical (Johnson et al., 2013, Wise et al., 2012, Xu et al., 2013) works. This happens because, in absence of metals, the dominant gas cooling agent is molecular hydrogen which is easily dissociated by Lyman Werner (LW) radiation. The mass of the halo determines whether its column density is high enough to self-shield against photodissociation. Hence, for unpolluted minihalos, Pop III star formation is largely suppressed. Note that the strength of the quenching is still debated (Haiman & Bryan, 2006) and in simulations it depends of the specific radiative transfer implementation (Wolcott-Green et al., 2011).

In our simulation we do not account for the LW background nor do we apply a H_2 - based star formation criterion; rather, the quenching of star formation in low mass halos is mimicked by mass resolution. This (convenient) numerical feature has also been noted by Xu et al. (2013) in comparison with the previous work by Wise et al. (2012). Xu et al. (2013) have a factor ∼ 16 better resolution allowing them to resolve halos of mass $\sim 10^6 M_\odot$. However, a proper inclusion of the LW background leads Xu et al. (2013) to conclude that the minimum mass of star forming halos is $\simeq 3 \times 10^6 M_\odot$, in almost perfect agreement with findings of Wise et al. (2012).

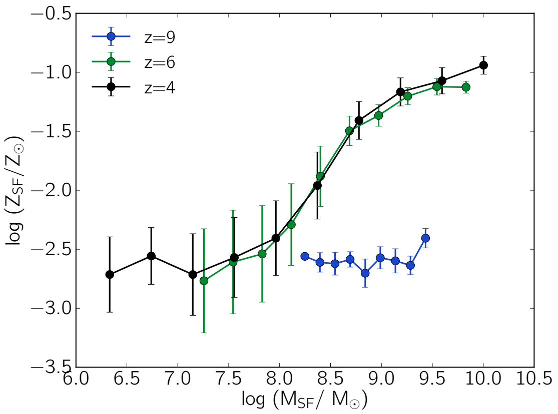

FIGURE 2.5: Gas metallicity vs. total (gas+stars) baryonic mass in star forming regions at $z = 9$ (blue line), $z = 6$ (green line) and $z = 4$ (black line). The data have been binned in mass ($\log(M/M_\odot) \simeq 0.2$). Errorbars show the 1-$\sigma$ deviations within the bin.

The SFR history is closely connected to the evolution of metal enrichment. The total amount of metals produced by star formation rises from $\Omega_Z^{\rm SFH} = 1.52 \times 10^{-6}$ at $z = 6$ to 8.05×10^{-6} at $z = 4$: this trend follows the growth of the cosmic stellar mass, as $\Omega_Z^{\rm SFH} \propto$ SMD (Ferrara et al., 2005). The metal enrichment history has been tracked on-the-fly during the simulation. Fig. 2.2 shows the predicted redshift evolution of the mean metallicity of the gas, $\langle Z \rangle$, calculated by averaging over all the baryons in the simulation volume, and the analogous one for star forming regions, i.e. $\langle Z \rangle_{\rm SF}$, obtained by averaging only over cells in which $\Delta > \Delta_{\rm th}$.

As we see, $\langle Z \rangle$ monotonically increases with time from $\sim 10^{-6} Z_\odot$ at $z = 11$ to $\sim 10^{-2} Z_\odot$ at $z = 4$. This result is consistent with Tornatore et al. (2007), Maio et al. (2010) and Davé et al. (2011) and expected given the SFR evolution discussed previously.

Instead, if we only consider star forming regions, the mean metallicity evolution of these cells presents a slightly more complex behavior, also shown in Fig. 2.2. It raises abruptly from very low values at $z \geq 10$ reaching a peak of $4 \times 10^{-3} Z_\odot$ at $z = 9.3$, consistently with the metallicity level obtained by Greif et al. (2010) in the inner part of a galaxy witnessing a single PISN explosion. After a short (100 Myr) decreasing phase, $\langle Z\rangle_{\rm SF}$ begins to increase steadily. At $z \lesssim 8$ star forming regions are roughly 10 times more metal-rich than the mean of all baryons. This peculiar trend is worth a more close scrutiny.

First, the drop of $\langle Z\rangle_{\rm SF}$ for $z \gtrsim 9.5$ is a selection effect introduced by our density-based definition of star forming cells ($\rho > \rho_{\rm th}$). In the first low-mass galaxies experiencing their first star formation event, SN feedback is sufficiently strong to completely disperse their gas and decrease the local gas density below $\rho_{\rm th}$. As at high z this situation is almost the rule, $\langle Z\rangle_{\rm SF}$ drops precipitously. This also implies that these galaxies are not able to sustain a steady star formation activity: this early flickering star formation mode is also reflected in the SFR evolution discussed in Fig. 2.1.

It is only when the feedback action becomes less violent and able to gently regulate the star formation activity of individual galaxies that the process stabilizes. This transition eventually occurs around $z \simeq 8$, after a brief (100 Myr) phase in which metals spread from the interstellar medium (ISM) into the CGM and finally into the IGM. During this phase $\langle Z\rangle_{\rm SF}$ decreases as a result of the increasing primordial gas mass into which metals are distributed. Note that as soon as a steady star formation activity can be sustained $\langle Z\rangle_{\rm SF} > {\rm Z}_{\rm crit}$. Thus, Pop III star formation must be confined to external regions of star forming galaxies or located in the remaining pristine galaxies. We further discuss this point in the next Section and in Sec. 2.5.

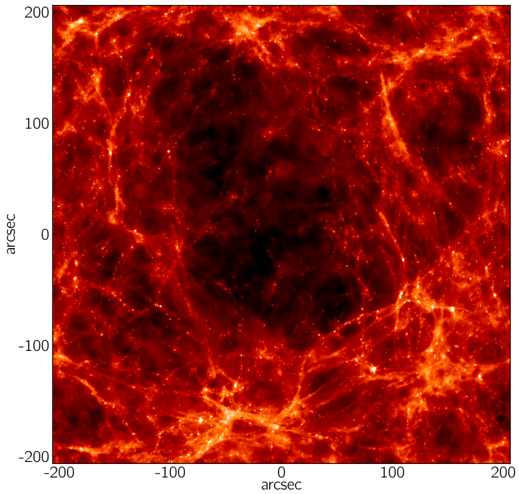

FIGURE 2.6: Rendering of the gas temperature and density fields convolution at $z = 4$ for the full 10 Mpc h^{-1} simulation box, corresponding to about 400 arcsec. Details on the rendering technique can be found in Appendix B.

To summarize, the SFR increase occurs when galaxies (on average) enter the regulated star formation regime. The exact redshift of this transition might in principle vary with numerical resolution. Such dependence is analyzed in Sec. 2.5 and Appendix A.

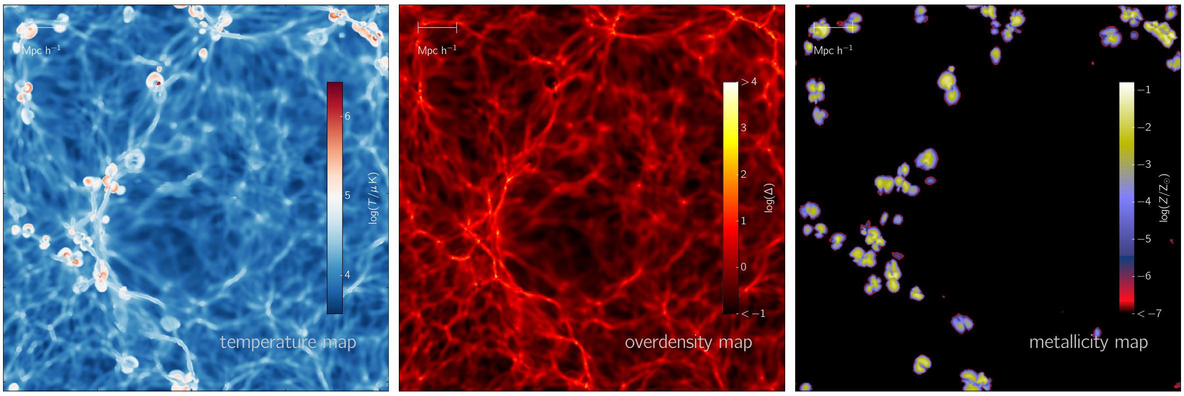

FIGURE 2.7: Maps of the simulated gas temperature (left), overdensity ($\Delta = \rho/\langle\rho\rangle$, center), and metallicity (right) at $z = 4$ in a slice of thickness $19.53\,h^{-1}$ kpc through the box.

2.3.1 Effects on stellar populations

The enrichment history of a given galaxy, among other aspects, affects the evolution of its stellar populations (e.g. Pop III vs. Pop II) and it is well quantified by the evolution of $P(Z)$, the mass-weighted stellar Metallicity Distribution Function (MDF), shown in Fig. 2.3 for three selected epochs, $z = 9, 6, 4$ and for all stars in the simulation box. Recall that we are adopting a critical metallicity for the Pop III - Pop II transition $\mathrm{Z_{crit}} = 10^{-4}\mathrm{Z}_\odot$. Since in RAMSES Z is treated as a passively advected scalar field (e.g. Dubois & Teyssier, 2007), in the following we will consider stars with $Z \leq 10^{-10}\mathrm{Z}_\odot$ as primordial to exclude spurious effects due to diffusion. When calculating MDFs, we consider all stars formed before the selected redshift.

At all redshifts shown the MDF displays a pronounced double-peak structure. The low metallicity (Pop III) peak is always centered at $Z \simeq 0$, while the Pop II peak grows with cosmic time, contemporarily shifting from $\simeq 10^{-2}\mathrm{Z}_\odot$ at $z = 9$ to $\simeq 10^{-1}\mathrm{Z}_\odot$ at $z = 4$. This evolutionary trend is induced by the monotonic increase of the mean metallicity of star forming regions that we report in Fig. 2.2; as Pop II stars dominate the stellar mass for $4 \leq z \lesssim 9$ (see Fig. 2.1) the peak position closely tracks the value of $\langle Z\rangle_{\rm SF}$ at a given redshift. It has to be emphasized that since the metallicity is mass weighted, the evolution of $\langle Z\rangle_{\rm SF}$ in Fig. 2.2 is dominated by the most massive star forming regions.

Interestingly, as time proceeds the MDF develops a characteristic low-metallicity tail which resembles the one derived from observations of metal-poor stars in the Milky Way (e.g. Caffau et al., 2011, Placco et al., 2013, Yong et al., 2012) and Local Group dwarfs (e.g. Frebel et al., 2010, Starkenburg et al., 2010). Clearly, the persisting non-detection of $Z \lesssim 10^{-6}\mathrm{Z}_\odot$ stars in current available stellar samples, supports the idea that Pop III were more massive than today forming stars, as already pointed out in Salvadori et al. (2007). However, whether the local stellar MDF can be considered as universal remains an open problem.

The MDF evolution can be used to characterize the environments in which Pop III stars formed. To this aim, we construct the indicator $R_{\rm P}$ expressing the ratio between the number of Pop III stars formed in extremely metal-poor (but not pristine; therefore these sites have already been enriched by a contiguous star formation episode to some $Z_* < {\rm Z_{crit}}$) environments and the total number of Pop III stars formed:

$$R_P = \frac{1}{N_{III}} \int_{Z_*}^{\rm Z_{crit}} \frac{{\rm d}P}{{\rm d}Z} {\rm d}Z\,, \tag{2.5a}$$

where

$$N_{III} = \int_{0}^{\rm Z_{crit}} \frac{{\rm d}P}{{\rm d}Z} {\rm d}Z\,. \tag{2.5b}$$

Assuming $Z_* \equiv 10^{-8}{\rm Z_\odot}$, from the previous formula we obtain $R_P(z=9) = 0.29$ and $R_P(z=6) \simeq R_P(z=4) = 0.19$. This result implies that Pop III stars are preferentially formed in purely pristine regions, well outside the polluted regions created by nearby/previous star forming galaxies. Only a minor fraction of Pop III is formed in inefficiently enriched sites. This scenario is in agreement with the notion of a "Pop III wave" suggested by Tornatore et al. (2007) and confirmed by Maio et al. (2010), starting from galactic centers and rapidly migrating towards more external regions where pristine gas to sustain their formation can be more easily found. Eventually, the galaxy will run out of unpolluted gas and its Pop III formation comes to a halt.

The $\simeq 1/3$ decrease of R_P from $z = 9$ to $z = 6$ indicates that galactic outflows become progressively more efficient in increasing the metallicity of polluted regions above ${\rm Z_{crit}}$, thus preventing Pop III to form in regions with very low but non-zero metal content. Finally, the negligible R_P variation between $z = 6$ and $z = 4$ is a consequence of the saturation of the Pop III SMD toward $10^6{\rm M_\odot\,Mpc^{-3}}$ at $z \simeq 5$ (see Fig. 2.1).

To understand which galaxies are the preferred sites of Pop III star formation we analyze the ~ 1600 star-forming halos at $z = 6$. In the upper panel of Fig. 2.4 we plot the Pop II and Pop III stellar mass ($M_{\rm PopII}$ and $M_{\rm PopIII}$) vs. halo mass. We define the Pop III mass fraction as $f_{\rm PopIII} = \langle M_{\rm PopIII}/(M_{\rm PopII} + M_{\rm PopIII})\rangle$, where the average is performed on the mass bin; $f_{\rm PopIII}$ is shown in the lower panel[7] of Fig. 2.4.

The Pop III mass fraction monotonically decreases with increasing halo mass, going from $\simeq 1$ at $M_{\rm h} \sim 10^{7.5}{\rm M_\odot}$ to $\lesssim 10^{-2}$ for $M_{\rm h} \gtrsim 10^{9.5}{\rm M_\odot}$. This is expected as only small ($M_{\rm h} \lesssim 10^8{\rm M_\odot}$) halos can produce Pop III stars, which are then inherited along the hierarchical formation sequence by larger descendants. The very small scattering in the stellar mass seen in the first two mass bins ($10^{7.5} \lesssim M_{\rm h}/{\rm M_\odot} \lesssim 10^8$) results form the fact

---

[7] Note that $f_{\rm PopIII} \neq \langle M_{\rm PopIII}\rangle/\langle M_{\rm PopII} + M_{\rm PopIII}\rangle$; not keeping this in mind can lead to misinterpretation when comparing the two panels.

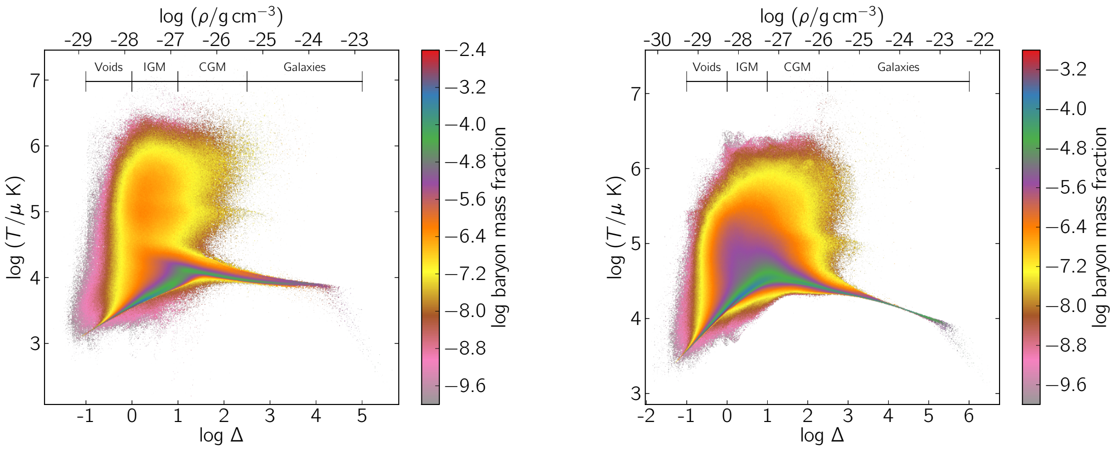

FIGURE 2.8: Equation of state (EOS) of the baryons at $z = 6$ (left) and $z = 4$ (right): the colorbar represents the differential mass weighted probability function. Temperature is expressed in molecular weight units; the density is given both in cgs units and in terms of the overdensity $\Delta = \rho/\langle\rho\rangle$.

that these small halos have essentially experienced a single (or a few at most) starburst event. As the amount of metals produced is typically sufficient to enrich the gas to values above $Z_{\rm crit}$, the subsequent star formation activity will already produce Pop II stars. In conclusion, we suggest that the most suitable halo mass range to observe Pop III stars is $10^{8.4} \lesssim M_{\rm h}/{\rm M}_\odot \lesssim 10^{8.7}$, since in these galaxies Pop III signature can be distinguished from Pop II, i.e. $f_{\rm PopIII} \simeq 0.5$, and at the same time their UV luminosities are sufficiently high to be detected in deep JWST spectroscopic surveys around $z = 6$.

2.3.2 Mass-metallicity relation

Star forming regions can be identified and associated with their parent galaxy using the technique described in Appendix C. We find a one-to-one match of star forming regions and galaxies; this is expected, since the finding algorithm does not allow to resolve substructure on scales $< 9.76\,h^{-1}$ kpc. Once the galaxy catalogue at different redshifts has been built, we can relate the gas metallicity of each star forming region, $Z_{\rm SF}$, with its total (gas+stars) baryonic mass, $M_{\rm SF}$. This relation is shown in Fig. 2.5 for various redshifts and for a mass bin size log $M/{\rm M}_\odot \simeq 0.2$. The errorbars represent the r.m.s. scattering within the mass bin.

At $z = 9$ (blue line), the metallicity is essentially independent of the stellar mass, achieving an almost constant values of $Z_{\rm SF} \simeq 10^{-2.7}{\rm Z}_\odot$ in the entire mass range, $10^8 \lesssim M_{\rm SF}/{\rm M}_\odot \lesssim 10^{9.5}$. This surprising behavior is due to the fact that at $z = 9$ star forming regions have experienced only one or few bursts. Hence, the $Z_{\rm SF} \simeq 10^{-2.7}{\rm Z}_\odot$ enrichment level is set by the dilution of the heavy elements produced by these early bursts into the surrounding ISM. This point can be clarified by the following simple argument. Suppose that a star forming region has recently formed a mass of stars $M_\star$, and consequently a mass of metals $M_Z = YM_\star$. To a first approximation the surrounding interstellar gas mass swept by the SN blast will be $M_g \propto \epsilon_{sn} M_\star$. Hence, the expected gas metallicity from a single burst is $Z_{\rm SF} = M_Z/M_g \equiv$ const., and the mass-metallicity relation shows no trend.

As star formation continues and stabilizes on larger scales a more definite trend emerges. At $z = 6$ (green line) for example, we see that metallicity increases with stellar mass up to $\rm M_{SF} \simeq 10^{9.2}$, where the relation starts to flatten. This trend becomes slightly more evident at $z = 4$, as it extends to a wider mass range.

On the other hand, for $M_{\rm SF} \gtrsim 10^7 \rm M_\odot$, the shape of the $z = 4$ curve (black line) remains almost identical to $z = 6$, with little signs of evolution over the time span of 600 Myr elapsed between the two epochs, as already pointed out by a recent study by Dayal et al. (2013). Also noticeable is the apparent invariance of the flattening scale, which might be related to the ability of systems with $M_{\rm SF} \gtrsim 10^{9.5} \rm M_\odot$ to retain most of the produced metals (e.g. Mac Low & Ferrara, 1999), in contrast to lower mass systems that are more likely to eject them into the IGM due to their shallower potential wells.

Note that at $z = 4$ the relation extends below $M_{\rm SF} \lesssim 10^7 \rm M_\odot$: this is due to the presence of satellite galaxies forming in pre-enriched regions of the CGM. Thanks to efficient cooling by metal lines gas in these low-mass systems can now become sufficiently dense to trigger star formation. Similarly to what found at $z = 9$ we see that $M_{\rm SF} \lesssim 10^7 \rm M_\odot$ regions show an almost constant metallicity, $Z_{\rm SF} \sim 10^{-2.7} \rm Z_\odot$, which is the result of the few bursts of star-formation they experienced. Such a flat metallicity trend resembles the one observed in the faintest Local Group dwarf galaxies (e.g. Kirby et al., 2013), and its physical interpretation is in agreement with the findings of Salvadori & Ferrara (2009).

At $z = 4$, we can compare our $M_\star - Z$ relation with the observed one, inferred from a sample of 40 galaxies at $3 \lesssim z \lesssim 5$ with masses $10^8 \rm M_\odot \lesssim M_\star \lesssim 10^{11} M_\odot$ (e.g. Troncoso et al., 2014). The simulated high masses ($M_{\rm SF} \gtrsim 10^{9.5} \rm M_\odot$) star forming regions contain $M_\star \simeq 10^{8.5}$. Averaging their metallicity we can convert to oxygen abundance by assuming a solar composition (e.g. Asplund et al., 2009): we find $\log(\mathrm{O}/H) + 12 = 8.19$, in agreement within 1-$\sigma$ of the values found by Troncoso et al. (2014).

2.4 Diffuse cosmic gas

We start by presenting a qualitative overview[8] of the cosmic gas distribution in Fig. 2.6. The main image shows a rendering of the gas temperature and density fields convolution

---

[8] Additional overviews of the simulations can be appreciated as movies, that are available at `https://www.researchgate.net/profile/Andrea_Pallottini`

for the whole simulation box at $z = 4$. The rendering has been obtained using the back-front imaging technique presented in Appendix B. This technique both allows to clearly identify the typical cosmic web structure made of voids, filaments, knots and clusters, and, thanks to the temperature weighting, the supernova shock structures.

More quantitative information can be gathered from the density, temperature and metallicity maps at $z = 4$ (Fig. 2.7). A comparison between the density and temperature fields allows to identify both active and/or relic star forming regions ($\Delta > \Delta_{\rm th}$) that are characterized by shock-heated hot ($T\,\mu^{-1} \gtrsim 10^5$ K) gas contained in approximately spherical bubbles, of size up to several hundred comoving kpc. The hot gas is enriched in heavy elements up to $\simeq 10^{-1}{\rm Z}_\odot$ and many of the bubbles can be identified in both maps. However, we see several bubbles with significant metallicity that contain cooler ($2 - 5 \times 10^4$ K) gas. These bubbles have been produced by earlier stellar populations and had the time to cool via adiabatic expansion and – to a lesser extent – radiative cooling. This implies that metallicity, differently from temperature, retains a fair record of the cosmic star formation activity.

An operative classification of the various cosmic environments can be made in terms of the gas overdensity. In Fig. 2.8, we show the gas mass-weighted equation of state (EOS) at $z = 6$ and $z = 4$. We can define four different environments: (a) the *voids*, i.e. regions with extremely low density ($\Delta \leq 1$); (b) the true *intergalactic medium*, characterized by $1 < \Delta \leq 10$; (c) the *circumgalactic medium* (CGM, $10 < \Delta \leq 10^{2.5}$), representing the interface between the IGM and galaxies, and (d) high density ($\Delta > 10^{2.5}$) collapsed structures, that for brevity we denote as *galaxies*.

This classification does not account for the thermal state of the gas. In fact, all the environments but galaxies are characterized by a range of temperature. For this reason, we will often call “diffuse phases” the environments (a), (b), (c). As the gas is heated either by photo-ionization ($T\,\mu^{-1} \lesssim 10^5$ K) or by shocks ($T\,\mu^{-1} \gtrsim 10^5$ K), to improve our classification we discriminate between gas colder or hotter than $T\,\mu^{-1} = 10^5$ K, thus allowing to readily get an estimate (see Fig. 2.9) of the relative importance of such heating mechanisms in the various phases.

Fig. 2.8 allows to build a complete census of the cosmic baryons. Most of the baryons reside in the diffuse phases, with galaxies accounting only for a tiny fraction of the total mass steadily increasing from $\lesssim 5\%$ at $z = 6$ to $\simeq 9\%$ at $z = 4$. Among diffuse phases, the CGM contains about 15% of the baryons, the remaining fraction being almost equally divided between voids and the IGM with little variation from $z = 6$ to $z = 4$.

At both redshifts, there is a continuous transition from voids to the IGM as both components follow a $T \propto \Delta^\gamma$ relation, with an adiabatic index $\gamma = 1/2$. This relation

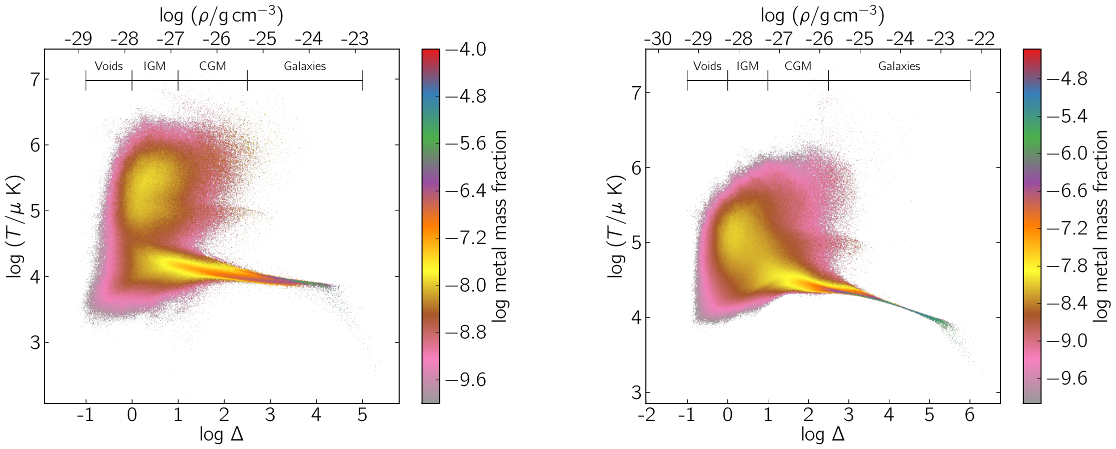

FIGURE 2.10: Metal weighted EOS at $z = 6$ (left) and $z = 4$ (right). The notation is the same as in Fig. 2.8.

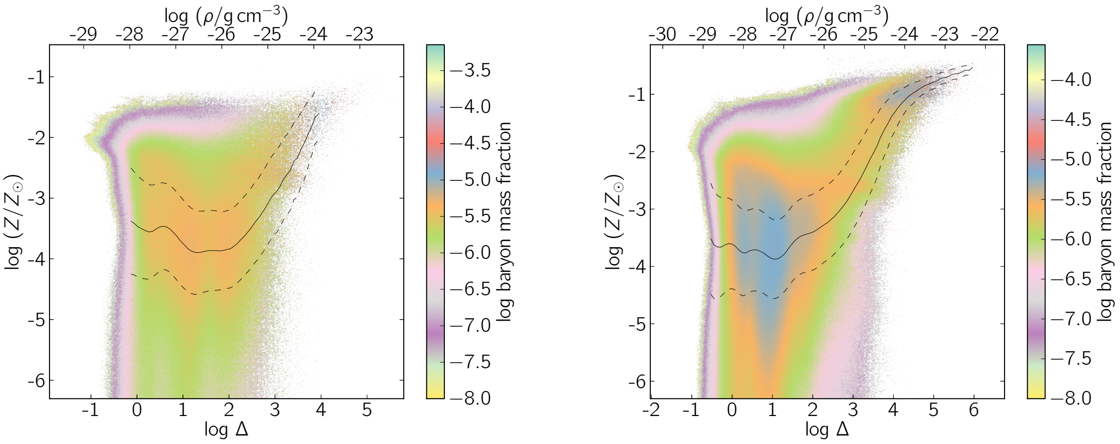

FIGURE 2.11: Mass weighted probability distribution function (PDF) of the baryons at $z = 6$ (left) and $z = 4$ (right) in the metallicity-overdensity plane. The solid (dashed) black line is the mean (r.m.s.) metallicity as a function of density.

is well known to arise from the balance between adiabatic expansion cooling and photo-heating (e.g. Theuns et al., 1998). In the CGM, however the EOS flattens as a result of the increasing importance of radiative cooling losses, driven both by a higher density and by a larger metal abundance, as we will see in the next Section. Metal cooling is important also for the shock-heated IGM. Compared to metal-free simulations (e.g. Pallottini et al., 2013, , in particular see Fig. 7), where typical values of the shock-heated gas temperature can reach $T\mu^{-1} \sim 10^8$ K, here metal cooling decreases the bulk temperature of the gas to values $T\mu^{-1} \lesssim 10^6$ K. Overall this picture is consistent with previous results found by Rasera & Teyssier (2006) and also by Cen & Chisari (2011) (in particular see their Fig. 20).

2.4.1 Metal enrichment

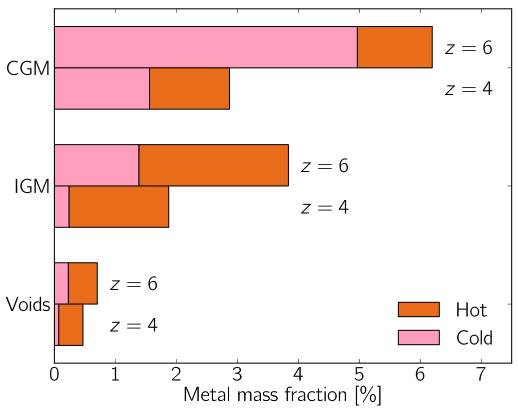

FIGURE 2.9: Phase distribution of the *enriched* intergalactic gas at $z = 6$ and $z = 4$. For every phase, the relative cold ($T\,\mu^{-1} \leq 10^{4.5}$ K) and hot ($T\,\mu^{-1} > 10^{4.5}$ K) parts are shown in pink and orange, respectively.

Contrary to baryons, which reside predominantly in the IGM, metals are found at any given redshift primarily near their production sites, i.e. in galaxies. However, while at $z = 6$ galactic metals make up to about 90% of the total heavy elements mass, at later epochs ($z = 4$) this fraction increases to 95% as a result of the increased ability of collapsed objects to retain their nucleosynthetic products thanks to their larger potential wells. Among the diffuse components (see Fig. 2.9), at $z = 6$ the CGM is more enriched than the IGM (voids) by a factor 1.6 (8.8), as metals cannot be efficiently transported by winds into distant, low-density regions. Interestingly though, even the most diffuse gas in the voids has been polluted to some extent. We will see later on that by $z = 4$ about 1/10 of the cosmic volume has been enriched to a non-zero metallicity. These results are consistent with previous studies (e.g. Oppenheimer & Davé, 2006).

In Fig. 2.10 we plot the metal mass-weighted EOS at $z = 6$ (left panel) and $z = 4$ (right panel). The temperature structure shows a clear evolution between the two redshifts. The most prominent feature is that the enriched IGM ($\Delta = 1 - 10$) at $z = 6$ is characterized by a bimodal temperature distribution, which then merges into a single thermal structure by $z = 4$. We interpret this evolution as the result of the early IGM enrichment and heating by winds from low mass galaxies followed by cooling due to radiative losses. Note that the same temperature feature is visible in the baryonic EOS (Fig. 2.8). The relative abundance of cold ($T\,\mu^{-1} \leq 10^{4.5}$ K) and hot ($T\,\mu^{-1} > 10^{4.5}$ K) gas in the various diffuse phases is shown in Fig. 2.9.

The interesting conclusion is that while in the CGM the majority of metals are found to be cold, in the IGM and in voids densities are too low to allow the enriched gas to efficiently cool. Let us then evaluate the cooling time at $z = 6$:

$$t_c(\Delta) = \frac{3}{2}\frac{k_B T}{n\Lambda(T, Z)} \simeq 4.8\left(\frac{T}{10^6\mathrm{K}}\right)\Delta^{-1}\mathrm{Gyr}, \qquad (2.6)$$

where we have assumed a value for the cooling function $\Lambda = 2 \times 10^{-23}$erg cm^{3}s^{-1} appropriate for a gas with $T\,\mu^{-1} = 10^6$ K and $Z = 10^{-2}\mathrm{Z}_\odot$. Thus, shock-heated, enriched overdensity with $\Delta > 7.6$ will be able to cool during the cosmic time interval between $z = 6$ and $z = 4$, i.e. 0.63 Gyr, consistently with the results of our simulations.

This simple argument also explains the increasing relative fraction of hot metals with decreasing density of the diffuse phases, shown in Fig. 2.9. This point has two important implications: (a) a considerable fraction of metals are hidden in a hot phase of the CGM/IGM/voids that is difficult to detect via absorption line experiments, highlighting the long-standing missing metals problem already noted by Pettini (1999) and quantified by Ferrara et al. (2005); (b) a small ($\lesssim 1\%$) but not negligible fraction of metals managed to reach very rarefied environments as the voids, and in some case also to cool. This implies that these metals must have been injected at sufficiently early epochs that they had the time to cool, i.e. as expected in a pre-enrichment scenario (Madau et al., 2001).

The $Z - \Delta$ distribution of the cosmic gas provides additional insights in the metal enrichment process (Fig. 2.11). At $z = 6$ (left panel) baryons are nearly uniformly distributed in $10^{-1} \lesssim \Delta \lesssim 10^{2.5}$ and the cosmic gas is characterized by a broad range of metallicities ($10^{-6} \lesssim Z/\mathrm{Z}_\odot \lesssim 10^{-2}$). Besides containing most of the metals, galaxies ($\Delta \gtrsim 10^{2.5}$) show high metallicities ($10^{-2} \lesssim Z/\mathrm{Z}_\odot \lesssim 10^{-1}$) and a loose $Z - \Delta$ correlation. At $z = 4$ (right panel) the distribution evolves and the $Z - \Delta$ correlation at high density becomes tighter and steeper, additionally extending to lower overdensities. Both the IGM and the CGM become preferentially enriched at $10^{-4.5} \lesssim Z/\mathrm{Z}_\odot \lesssim 10^{-2.5}$, i.e. around the critical metallicity for the Pop III transition. The overall shape of the distributions at different z agree well with those found by Gnedin & Ostriker (1997), Oppenheimer et al. (2012) and with the observed IGM metallicities (e.g. Meiksin, 2009).

As time evolves, metals are not only produced at an increasing rate but they are transported by winds away from the production sites. To see this it is useful to derive the fraction of the cosmic volume, V, filled with heavy elements at a metallicity larger than a given value, Z_{cut}. Formally, this can be written as

$$Q(> Z_{\mathrm{cut}}) = \frac{1}{V} \int \Theta(Z - Z_{\mathrm{cut}}) \mathrm{d}V. \tag{2.7}$$

The behavior of Q for different values of Z_{cut} has been traced on-the-fly in the simulation. The result is shown in Fig. 2.12, which highlights interesting features of the enrichment process.

As we have already seen (Fig. 2.2), the typical metallicity of star forming regions at $z \simeq 4$ is $\simeq 10^{-1}\mathrm{Z}_\odot$ and corresponds to the lowermost curve in Fig. 2.12. Even at the lowest redshifts, star forming regions fill a very small fraction ($\simeq 10^{-5}$) of the volume; however, these sites represent the metal production factories, out of which metals are ejected and distributed by outflows in the CGM and IGM. As a matter of fact, the non-monotonic behavior at $z \lesssim 6.5$ of $Q(> 10^{-1}\mathrm{Z}_\odot)$ is related to the increasing ability of galaxies to retain their metals as they become on average more massive (see Fig. 2.5).

For lower values of $Z_{\rm cut}$, $Q(> Z_{\rm cut})$ increases rapidly: already the region encompassing a mean metallicity $Z > 10^{-2}\,{\rm Z}_{\odot}$ fills a volume $\gtrsim 10^3$ times larger (corresponding to a physical scale $\gtrsim 10$ times larger than the star forming regions). This region corresponds roughly to the CGM, i.e. the transition region surrounding the galaxy that is strongly influenced by the energy and mass input from the latter.

Finally, the $10^{-8} \leq Z_{\rm cut}/{\rm Z}_{\odot} \leq 10^{-3}$ range corresponds to the IGM (see Fig. 2.11), where the metal abundance is largely diluted by intergalactic hydrogen. Note that the $Q(> Z_{\rm cut})$ curves for $Z_{\rm cut}$ in the IGM range show little variation, indicating that the IGM metallicity is relatively constant at a value $10^{-3.5}{\rm Z}_{\odot}$. However, only a fraction $< 10\%$ of the cosmic volume has been ever polluted by heavy elements.

Overall, the filling factor evolution is consistent with the one found by Johnson et al. (2013) for $6 \leq z \lesssim 10$. Additionally, we found an evolution for $10^{-3} \leq Z_{\rm cut}/{\rm Z}_{\odot} \leq 10^{-2}$ similar to previous works (Cen et al., 2005, Oppenheimer & Davé, 2006, Oppenheimer et al., 2009). However, we find $Q(\geq 10^{-1}{\rm Z}_{\odot})$ is roughly ~ 10 times smaller than the corresponding one quoted in Oppenheimer et al. (2009). This is somehow expected, since high metallicity regions correlate with density peaks (see Fig. 2.11); therefore such discrepancy likely arises from variations in the feedback prescriptions (e.g. Scannapieco et al., 2012) and intrinsic differences between AMR and SPH (e.g. Kim et al., 2014, Power et al., 2014). The filling factor of metals has important implications for the relative evolution of Pop III stars and the local transition to a Pop II star formation mode that we will discuss in Sec. 2.5.

2.4.2 The circumgalactic medium

We devote this Section to some additional points concerning the CGM. We restrict the analysis to $z = 6$ because of the importance of this epoch for reionization (e.g. Pentericci et al., 2011, Schroeder et al., 2013) and because it represents the current limiting redshift for QSO absorption line statistical studies (e.g. D'Odorico et al., 2013). The CGM plays a key role in galaxy evolution as it represents the interface between galaxies and the IGM; moreover, ought to its relatively large overdensity and metallicity, it is more readily observed and may serve as a laboratory to study supernova feedback. Supernova winds carve large, hot, metal enriched bubbles in the CGM surrounding their host galaxies, as it is visually represented in Fig. 2.7.

It is then natural to ask whether relations exist between the properties of these bubbles and their parent galaxy. To answer this question, we first identify a galaxy and the associated metal bubble with the method described in Appendix C, based on a metallicity threshold criterion, i.e. the gas inside a bubble must have $Z > Z_{\rm th} = 10^{-7}{\rm Z}_{\odot}$. Choosing a

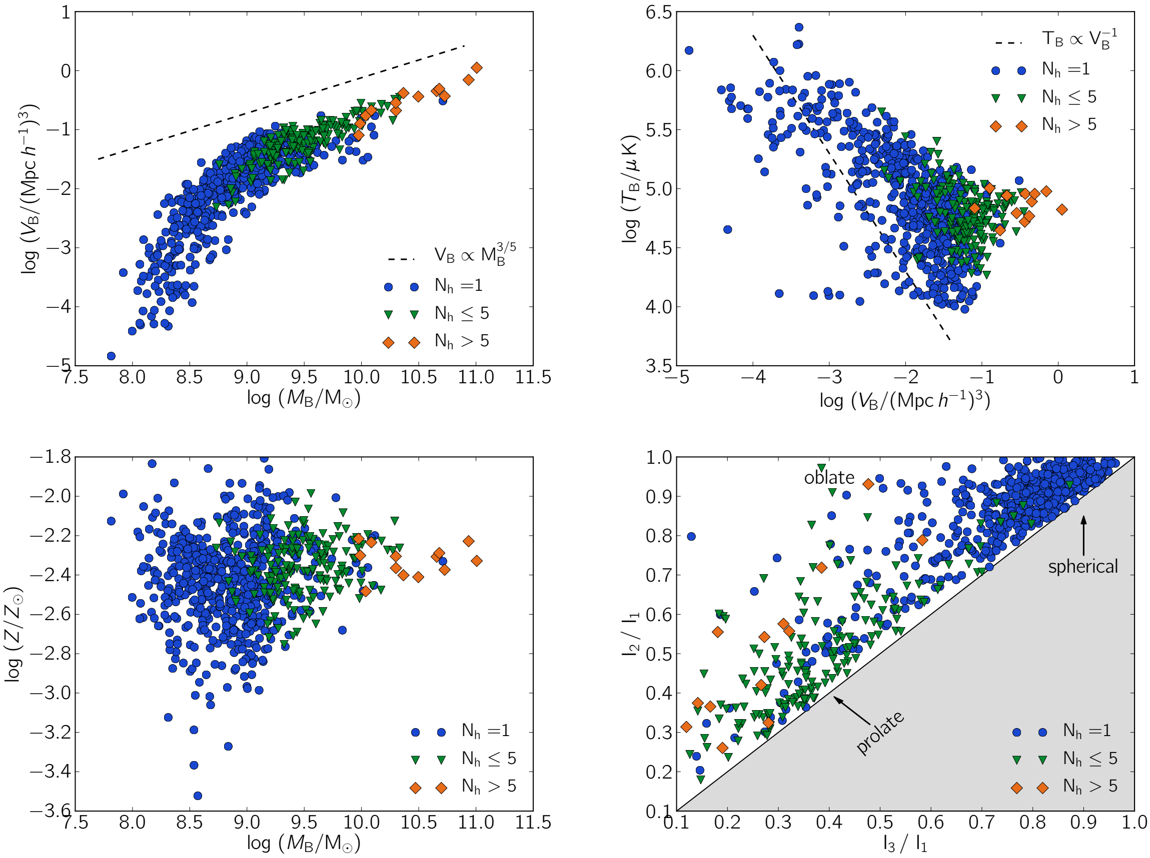

FIGURE 2.13: Physical and geometrical properties of metal bubbles at $z = 6$. *Upper-left panel:* bubble volume vs. enclosed gas mass; *Upper-right:* mean bubble temperature vs. volume; *Lower-left:* mean bubble metallicity vs. enclosed gas mass; *Lower-right:* bubble shape parameters. The number of halos (N_h) inside the bubble is also indicated. See Appendix C for the details on the definitions. Dashed black lines are the analytical relations inferred from the Sedov-Taylor blast solution (see text).

different Z_{th} would somewhat change the inferred bubble properties; however, the correlations we are going to discuss are insensitive to normalization constants. As a first step we classify metal bubbles on the basis of the number of galaxies present in their interiors: in Fig. 2.13 we use different symbols to differentiate bubbles according to the number of halos they contain, i.e. $N_h = 1$ (blue circle), $1 < N_h \leq 5$ (green triangle), and $N_h > 5$ (orange squares). Broadly speaking, one can think of the N_h parameter as an indicator of merging activity experienced by the bubble. The detailed definitions of the physical quantities characterizing the bubbles are given in Appendix C.

As we will see in the following, to a first order metal bubble properties can be very well described by the Sedov-Taylor adiabatic blast solution. It is then useful to recall its functional form:

$$V_B(t) = \zeta \left(\frac{E}{\rho_e}\right)^{3/5} t^{6/5} \tag{2.8}$$

where V_B is the bubble volume, $E = \sum_i^{N_\mathrm{h}} E_i$ is the total SN energy produced by the N_h halos inside the bubble, ρ_e is the mean density of the environment, t is the bubble age and ζ is a dimensionless factor of order unity. In the simplest case, E_i is proportional to the stellar mass formed and hence, for a fixed star formation efficiency (see eq. 2.2), to the baryonic mass of the i-th star forming region, $M_{\mathrm{SF},i}$. It follows that $E \propto \sum_i^{N_\mathrm{h}} M_{\mathrm{SF},i} \propto M_B$, having further assumed a universal radial density profile within each bubble. In addition, as the post-shock gas temperature is $T_B \propto v_B^2$, where v_B is the expansion velocity of the bubble, we also find, using eq. 2.8

$$T_B \propto \left(\frac{E}{\rho_e}\right) V_B^{-1}. \tag{2.9}$$

We can directly compare the predictions from these simple formulae with the simulation results. The upper-left panel of Fig. 2.13 shows that the volume of bubbles generally increases with the mass of the galaxies they contain; however, the largest ones result for the coherent action of ≥ 2 galaxies powering them. The $V_B - M_B$ relations follows nicely the $M_B^{3/5}$ analytical form, but smaller bubbles which are still in the initial phases of their evolution deviate from this simple law and have smaller volumes with respect to the mass of the galaxies they contain. The Sedov-Taylor relation accounts well also for the gas temperature within bubbles (upper-right panel) providing a good fit to the slope of singly-powered bubbles, while those with $N_\mathrm{h} \geq 2$ tend to have hotter bubbles as a result of the larger energy input and replenishment rate of hot gas. Small ($V_B \lesssim 10^{-2}(\mathrm{Mpc}\, h^{-1})^3$) bubbles are typically hotter and reach $T_B\mu^{-1} \gtrsim 10^5$ K. Viceversa, in bubbles with $V_B \sim 10^{-1}(\mathrm{Mpc}\, h^{-1})^3$ the temperatures can be as low as $T_B\mu^{-1} \sim 10^4$ K, i.e. they contain metals that had the time to cool and are currently purely advected with the expansion.

We find no clear correlation between Z and M_B (lower-left panel). This degeneracy mainly depends on the temporal evolution and the geometry. The elapsed time from the last SN explosion characterizes the metallicity spread, as injected metals are diluted into the surrounding medium (Madau et al., 2001). Additionally, the relative outflow-galaxy geometry affects the pollution. As shown by Recchi & Hensler (2013) using 2D chemo-dynamical simulations, the surrounding gas distribution can change the enriched gas metallicity by a factor ~ 10. This is particularly relevant at high masses ($M_B \gtrsim 10^9 \mathrm{M}_\odot$) where the bubbles tend to merge, thus shape effects are dominant. The absence of correlation could have been also expected from the smooth distribution of the CGM/IGM ($\Delta \lesssim 10^{2.5}$) in the $Z - \Delta$ plane (left panel of Fig. 2.11).

The geometry of the bubbles is influenced by the topology of the cosmic web. The shape of the bubbles can be described in terms of the eigenvalues I_i of the inertia tensor, where $I_1 \geq I_2 \geq I_3$. The ratios of the principal axis are used as index of sphericity (I_3/I_1), prolateness (I_3/I_2) and oblateness (I_2/I_1). The geometry of the bubbles can be analyzed in the sphericity-oblateness plane, i.e. I_3/I_1 vs. I_2/I_1, shown in the lower-right panel and obtained directly from the actual shape of bubbles in the simulation output. Almost 40% of the bubbles are in the spherically symmetric region ($I_3/I_1 \simeq 1$); most of them ($\sim 90\%$) correspond to bubble around isolated galaxies. Another $\sim 30\%$ of the bubbles conserves at least a cylindrical symmetry and populates the $I_3/I_1 \simeq I_2/I_1$ diagonal (prolate) and the $I_2/I_1 \simeq 1$ stripe (oblate). These region contains $\sim 70\%$ bubbles which have experienced few ($1 < N_\mathrm{h} \leq 5$) merging events. Because of the elongated shapes, the merging must have occurred along filaments of the cosmic web. The rest ($\sim 35\%$) have lost any kind of symmetry, and almost all ($\sim 90\%$) bubbles with large N_h values are located in this region. They correspond to metal polluted bubbles stretching along filaments and linking various knots of the cosmic density field.

2.5 Effects of Pop III IMF variations

To understand the interplay between cosmic metal enrichment and the Pop III - Pop II transition leading to a progressive disappearance of Pop III stars, we have performed an additional set of simulations. The suite is composed of three runs, solely differing in terms of the values adopted for the Pop III stellar parameters (R, Y, ϵ_sn), as summarized in Tab. 2.2. The single runs are named after the Pop III type selected, i.e. SALP, FHN and PISN.

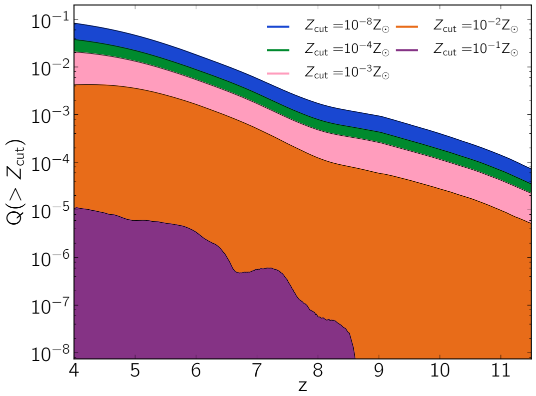

FIGURE 2.12: Redshift evolution of the metal volume filling factor, $Q(> Z_\mathrm{cut})$, for different values of the metallicity cut, Z_cut. See eq. 2.7 for the definition.

These simulations, similarly to the fiducial case examined here so far, evolve a 10 Mpc h^{-1} box; however, to limit the computational cost they are made with 256^3 DM particles. Consequently, the mass (spatial) resolution is lower by a factor 8 (2). The reduced resolution must be compensated with a more efficient star formation, and the best fit parameters of the subgrid prescription are now $t_\star = 1.5$ Gyr and $\eta_\mathrm{sn} = 0.3$. Again, the free parameters are fixed by matching the SALP run to the SFR observations (Bouwens et al., 2012) at low ($z \leq 7$) redshift. Note that these parameters are then kept fixed for all the Pop III star choices.

Fig. 2.14 shows the resulting SFR for the three runs. By comparing with the 512^3 fiducial run presented in Fig. 2.1, we notice that the lower resolution affects the SFR at

$z \gtrsim 8$. However for the comparison purposes of different Pop III properties this should not represent a major problem, and we also refrain from draw conclusions from $z \gtrsim 8-9$. The lower resolution causes the total SFR to be dominated by Pop III stars up to $z \sim 9$, as feedback is artificially more effective.

Note that there is weak dependence of the redshift at which galaxies become (on average) able to sustain a steady star formation process (see Sec. 2.3) on resolution. For the fiducial simulation this occurs at $z \simeq 8$, while in the rest of the suite it happens at $z \simeq 7.5$. Such epoch roughly coincides with the start of Pop III formation quenching. The two effects are obviously linked as follows from the discussion in the present Section.

Let us start by considering the evolution of Pop III SFR. Rather surprisingly, different prescriptions make essentially no differences on Pop III star formation history, apart from a slightly faster drop of PISN SFR below $z = 6$. This more rapid fading can be understood as a result of the $\simeq 10\times$ higher PISN energy input and metal yield resulting in a more widespread pollution of the volume above Z_{crit}. This can be visually appreciated from Fig. 2.15, featuring metallicity maps at $z = 4$ for the different runs.

Independently of z, the filling factor of regions enriched above the critical metallicity, $Q(> Z_{crit})$, in the PISN run is $\simeq 3$ times larger than for the SALP/FHN runs; in addition, the maximum metallicity is about 10 times higher. Based on this evidence one would expect a much more pronounced suppression of Pop III stars in the PISN case, which however is not observed, apart from the above mentioned small relative drop at $z < 6$. The results instead point towards a different interpretation. The key point is that enriching to $Z > Z_{crit}$ levels low density regions in the periphery of galaxies or the CGM does not produce a major effect in the SFR history of Pop III stars because the bulk of active Pop III formation sites is localized in newly forming halos far from the ones already hosting star formation. This is consistent with the previously discussed outcome of the fiducial run (see Fig. 2.3 and corresponding text) that Pop III stars are preferentially formed in a metal-free (rather than with $Z \neq 0$ but below Z_{crit}) environment; using semi-analytic models, Crosby et al. (2013) showed that for $z \lesssim 10$ Pop III formation takes

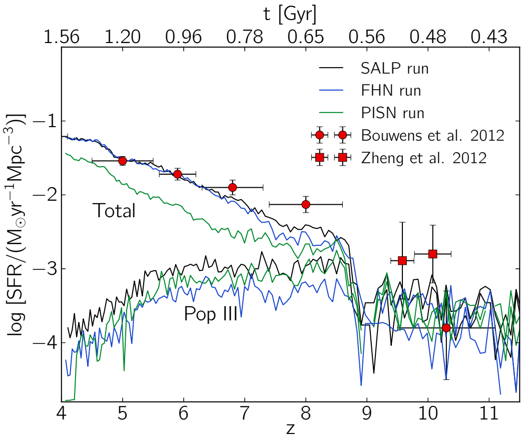

FIGURE 2.14: Simulation suite result of cosmic SFRs as a function of redshift (age of the Universe). Different colors correspond to different runs and distinguish the total and Pop III only SFR. See Tab. 2.2 for the reference values of the adopted assumptions for the Pop III.

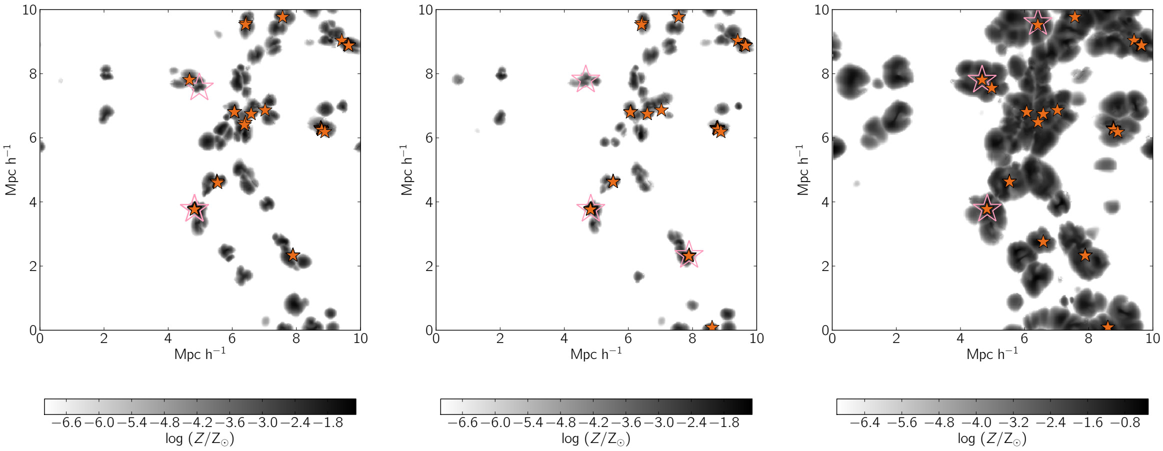

FIGURE 2.15: Metallicity maps at $z = 4$ for the SALP (left), FHN (middle), PISN (right) runs. Filled orange small (empty pink large) stars indicate the positions of Pop II (Pop III). The slice thickness is $39.06\,h^{-1}$ kpc.

place in pristine regions separated by sufficiently large distances.

To better substantiate the last statement we point out that the Pop III quenching strength is related to the ratio between the typical size of metal bubbles, $\langle R_B \rangle = \langle V_B^{1/3} \rangle$ (see Sec. 2.4.1 and Appendix C), and $r_{\rm SF}$, the correlation length of star forming regions[9]. In our simulations, we find that $r_{\rm SF} \simeq 2\,{\rm Mpc}\,h^{-1}$ at both $z = 6$ and $z = 4$. At the same time, the mean size of the bubbles goes from $\langle R_B \rangle \simeq 0.3\,{\rm Mpc}\,h^{-1}$ at $z = 6$ to $\simeq 0.5\,{\rm Mpc}\,h^{-1}$ at $z = 4$, thus quenching Pop III star formation. In fact, we can see from Fig. 2.1 that the fiducial model predicts ${\rm SFR}_{\rm PopIII}(z = 6) \simeq 10^{1.3}\ {\rm SFR}_{\rm PopIII}(z = 4)$.

In conclusion, the similar evolutionary trend of a flat Pop III SFR, persisting at a level of about $10^{-3}{\rm M}_\odot\ {\rm yr}^{-1}{\rm Mpc}^{-3}$, up to $z = 6$ and followed by a rapid drop thereafter, appears to be a solid feature of our model and to be independent of the details of Pop III IMF.

This physical interpretation implies that chemical feedback might be artificially enhanced in simulations when the mean pollution radius $\langle R_B \rangle$ becomes comparable to the simulation box size. We further discuss how resolution and box-size effects affect this issue in Appendix A. Note that additional uncertainties might come from the treatment of radiative feedback. A proper investigation of resolution and box size effects would require a suite of simulations with increasing box size and fixed resolution and a convergence study with fixed box-size and increasing mass resolution. We defer this study to a future work.

---

[9] The correlation length is defined as the scale at which the two point correlation function of star forming regions $\xi_{\rm SF}(r_{\rm SF}) = 1$ (e.g. Reed et al., 2009).

The effects of Pop III IMF variations have instead a larger impact on Pop II (and hence total) SFR. From Fig. 2.14 we see that, as for the Pop III case, the differences between a SALP or FHN IMF are minor: using Fig. 2.15 they can be quantified by $\langle |\log Z_{\rm FHN}/{\rm Z}_\odot - \log Z_{\rm SALP}/{\rm Z}_\odot|/\log Z_{\rm SALP}/{\rm Z}_\odot\rangle \simeq 0.01$, where the average is calculated on the slice. This difference is produced by the yields of Pop III SALP bs. FHN (Tab. 2.2) and from the stochasticity of star formation prescription (eq. 2.1).

On the other hand, differences are noticeable if a PISN IMF is assumed. In this case, the total SFR is depressed by a factor $\simeq 5$ for $z \gtrsim 5$. Because of the higher $\epsilon_{\rm sn}$ value, a pair-instability supernova can reach and disrupt a nearby potential star formation site, as also noted by Greif et al. (2010). Instead, less energetic hyper- or supernovae can only pollute their immediate surroundings, failing to reach other more distant and denser environments. Under the assumption of similar local star formation time scales ($t_\star$) for both Pop II and Pop III, the PISN scenario is difficult to be reconciled with the observed global SFR history, as feedback from these stars is probably too effective.

2.6 Synthetic spectra

We compute mock QSO absorption spectra along several l.o.s. drawn through the simulated box. The details of the adopted technique to compute the H I optical depth are given in Gallerani et al. (2006). Here, we also consider metal absorption lines due to ionic species such as Si IV, C IV, Si II, C II and O I. For these species, we compute the Doppler parameter according to the following expression $b_i = \sqrt{2k_BT/m_i}$, where m_i is the mass of the i-th species. In Tab. 2.3, we report the wavelengths and oscillator strengths (Prochaska et al., 2004) adopted for the considered species.

In order to compute the number density of different ionic species, we have built a grid of model calculations using CLOUDY (Ferland et al., 1998) version 10. We consider a plane parallel slab of gas in pressure equilibrium, illuminated by a Haardt-Madau ionizing background (Haardt & Madau, 1996, 2012). The intensity of the ionizing field at 1 Ryd has been normalized so that the photoionization rate, $\Gamma_{\rm HI}$ (units: s^{-1}), matches the values predicted by the two reionization models presented in Gallerani et al. (2008a,b), namely an Early Reionization Model (ERM) and a Late Reionization Model (LRM), predicting a reionization redshift of $z_{\rm rei} \simeq 7$ (ERM) and $z_{\rm rei} \simeq 6$ (LRM), respectively.

We point out that the ionizing background values predicted both by the ERM ($\log\Gamma_{\rm HI} = -12.46$) and LRM ($\log\Gamma_{\rm HI} = -12.80$) are consistent within 1-σ with the measurement of the UVB at $z = 6$ through the flux decrement technique ($\log\Gamma_{\rm HI} = -12.74 \pm 0.30$, Wyithe & Bolton, 2011); moreover, the ERM (LRM) is consistent within 2.1-σ (0.3-σ) with the

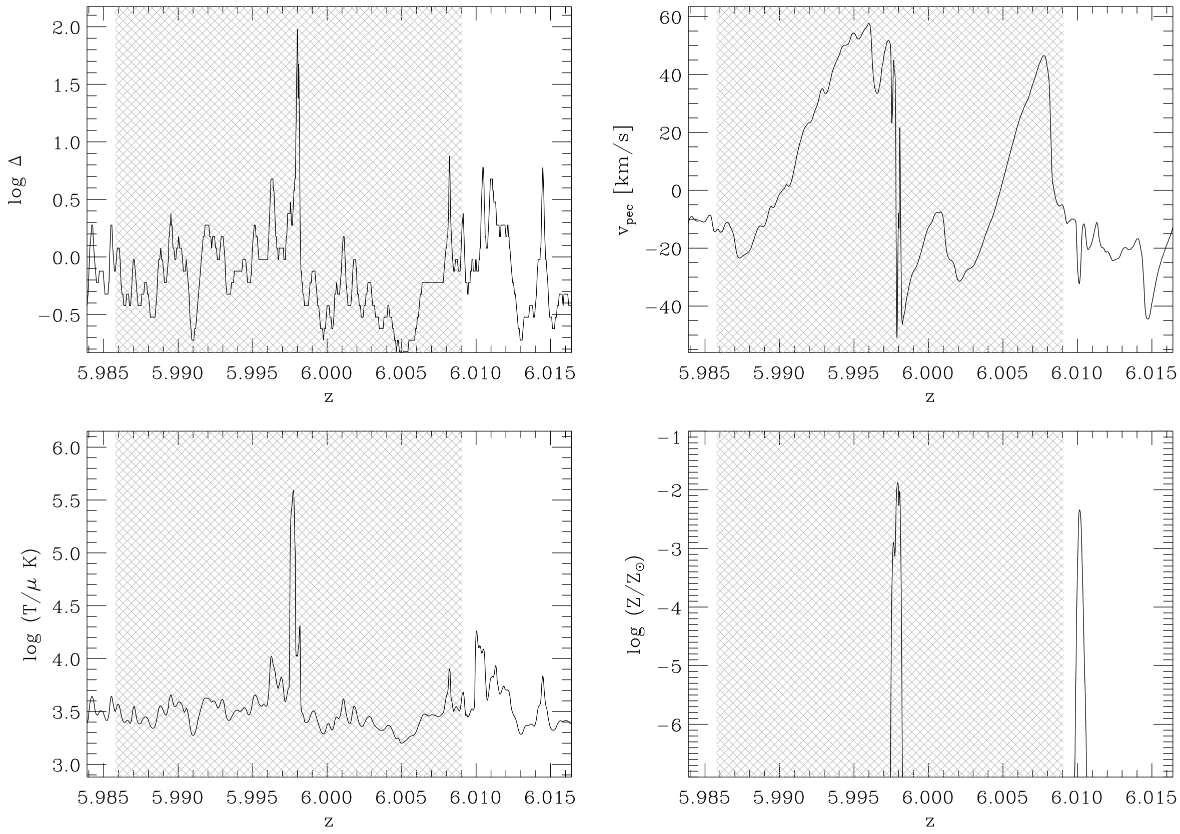

FIGURE 2.16: Distribution of the gas density (upper-left panel), peculiar velocity (upper-right panel), temperature (lower-left panel), metallicity (lower-right panel) along a random l.o.s. drawn through the simulated box at $z = 6$.

results obtained through the proximity effect technique ($\log \Gamma_{\rm HI} = -12.84 \pm 0.18$, Calverley et al., 2011). Each CLOUDY model is characterized by a gas metallicity, density and a constant temperature. As for the chemical composition, we adopt the solar elemental abundance ratios provided in CLOUDY. Calculations are stopped when the depth of the slab reaches our cell resolution.

We interpolate CLOUDY results with the gas properties predicted by the simulation. In Fig. 2.16, we show the distribution along a random l.o.s. of several quantities, namely: gas density (upper-left panel), peculiar velocity (upper-right panel), gas temperature (lower-left panel), and metallicity (lower-right panel).

Although a detailed, quantitative comparison with observations is beyond the aim of the present Chapter, we include observational artifacts in our simulated spectra, following D'Odorico et al. (2013), a work based on X-shooter spectra. For species with absorption features in the wavelength range $\lambda_i < 1440$ A ($\lambda_i > 1440$ A), since the absorption systems of interest at $z = 6$ are redshifted in the VIS (NIR) region of the X-Shooter spectrum, we smooth the synthetic spectra to a resolution $R = 8800$ ($R = 5600$), we add to each pixel a Gaussian random deviate, yielding a signal-to-noise ratio $S/N = 50$ ($S/N = 10$),

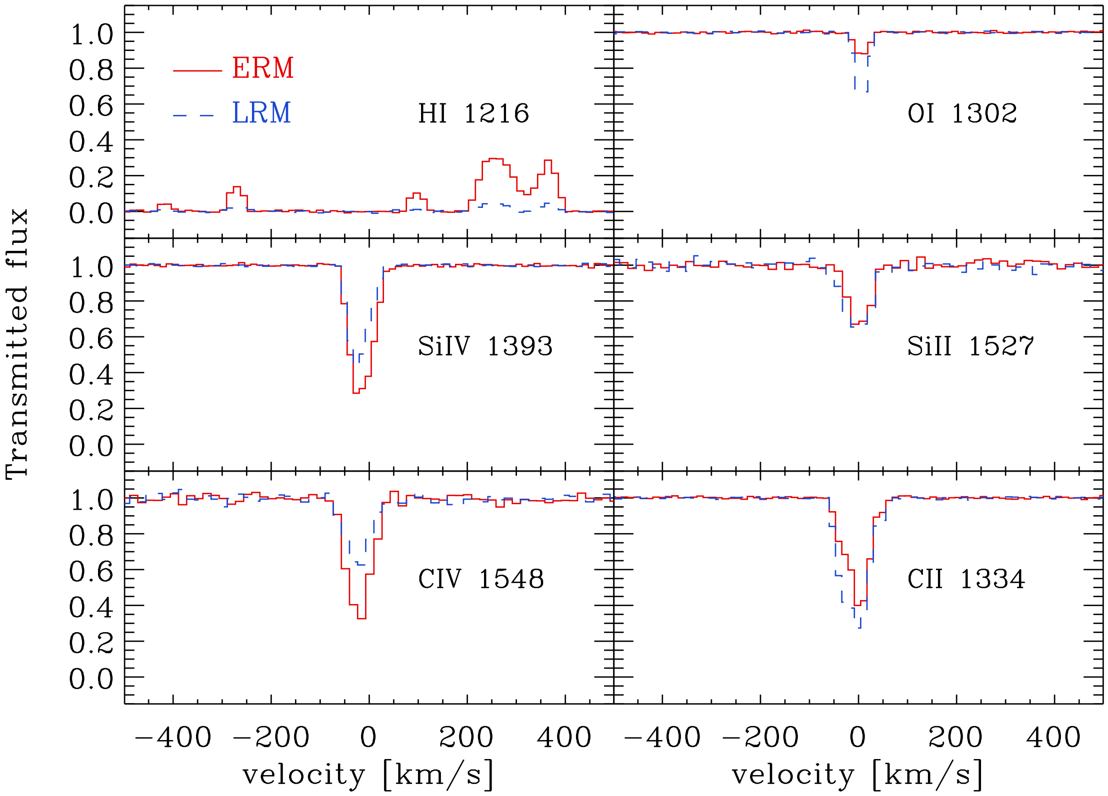

FIGURE 2.17: Synthetic spectra extracted from the l.o.s. drawn through the simulated box with physical properties shown in Fig. 2.16. The spectra are calculated using an Early Reionization Model (ERM, red solid line) and a Late Reionization Model (LRM, blue dashed line) for Lyα forest (upper-left panel) and metal absorption lines (O I, upper-right panel; Si IV and Si II, middle-left and middle-right panel; C IV and C II, lower-left and lower-right panel, respectively). See the text for the definitions.

and we finally rebin the simulated transmitted flux in channels of width 0.4 A (0.6 A).

An example of the simulated spectra obtained through this procedure is shown in Fig. 2.17, where the velocity interval corresponds to the redshift range marked through gray hatched regions in Fig. 2.16. Metal absorption lines show up preferentially in correspondence of metal-rich ($Z \gtrsim 10^{-2}$ Z$_\odot$), IGM/CGM regions ($\Delta \gtrsim 1-10$), characterized by mean temperatures $T\mu^{-1} \simeq 10^{4.5}$ K, as the ones occurring at $z \simeq 5.997$ in our sample l.o.s.. As expected, absorption lines due to atoms at high ionization levels (e.g. C IV and Si IV) are more pronounced with respect to low-ionization absorption lines (e.g. Si II and O I) in the case of the ERM, which predicts a higher ionizing background at the redshift of the absorption system. The above relations are reversed in the LRM case.

To get further insight, for each species and reionization model we compute $N_{\rm los}^{\rm tot} = 300$ synthetic spectra as the ones shown in Fig. 2.17 and we analyze them in terms of the PDF of the transmitted flux ($F_{\rm tr}$). The result is shown in Fig. 2.18. We divide the transmitted flux in four bins, and for each of them we show the PDF values predicted for

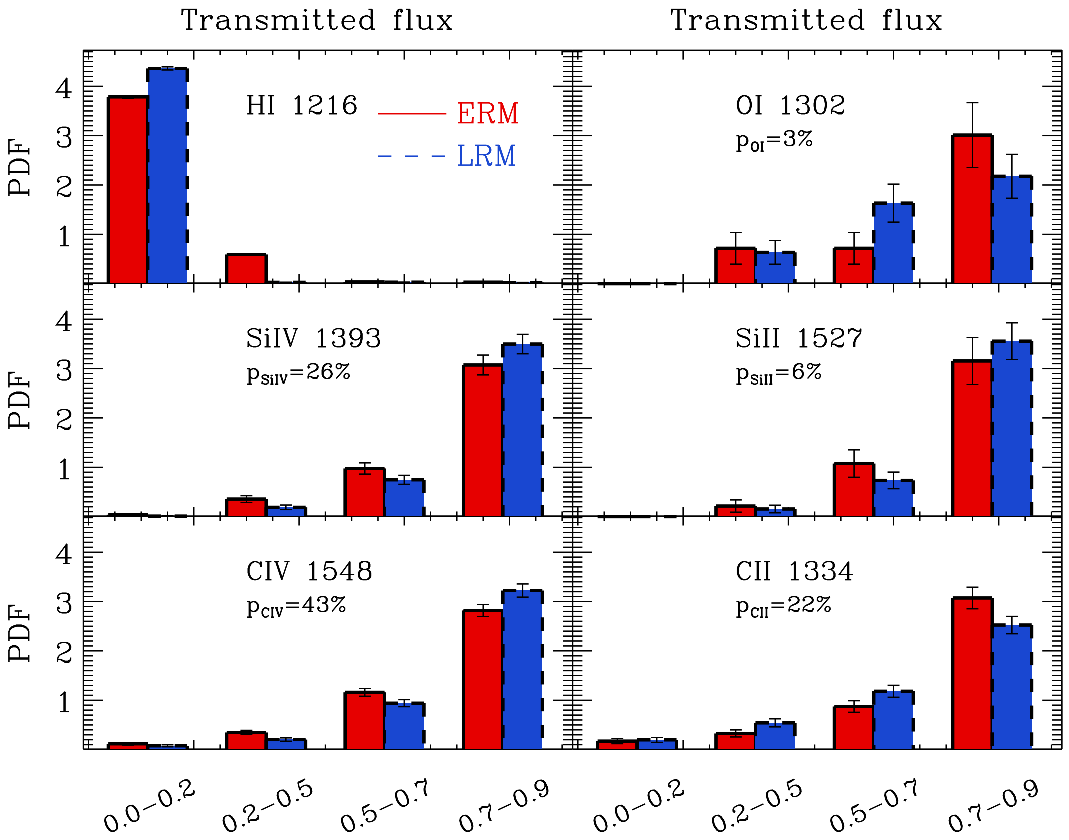

FIGURE 2.18: PDFs of the transmitted flux for the species considered in Fig. 2.17. The solid line (red shaded region) represents our predicted PDF in the case of the ERM, while the dashed line (blue shaded region) denotes LRM results. For each bin, we report the corresponding poissonian error bars. For each ion, we indicate the probability of encountering its corresponding absorption line in the l.o.s. sample, as defined in the text.

the ERM (solid line, red shaded region), LRM (dashed line, blue shaded region), with the corresponding poissonian error bars. For metal absorption lines, we restrict our analysis to those spectral regions characterized by $F_{\rm tr} < 0.9$. For each species considered, we also report the probability to find at least one absorption line per l.o.s., $p_i = N_{\rm los}^{\rm abs,i}/N_{\rm los}^{\rm tot}$, where $N_{\rm los}^{\rm abs,i}$ is the number of l.o.s. in which we find at least one absorber of the i-th species.

Fig. 2.18 confirms that, in the case of the Lyα forest, the PDF analysis does not provide a fair diagnostics of the IGM ionization level at $z \sim 6$ (Fan et al., 2006, Gallerani et al., 2006, 2008a). In fact, from the upper-left panel, it is clear that in both reionization models, most of the pixels are characterized by $F_{\rm tr} \simeq 0.1$, meaning that this statistics is basically dominated by noise.

The same figure shows that, instead, the PDF obtained from metal absorption lines contains a wealth of information, and may provide strong constraints on the ionizing background intensity. It is also interesting to note that the presence of strong O I absorbers

($F_{\rm tr} \simeq 0.3$) does not exclude the possibility that the IGM/CGM is ionized, since these absorption systems are also found in the ERM, which predicts a small neutral hydrogen fraction ($x_{\rm HI} \simeq 10^{-4}$) at $z \simeq 6$. Observations of O I absorption systems at these redshifts are useful tools for understanding the metal enrichment and cosmic reionization processes (Finlator et al., 2013, Keating et al., 2014, Oh, 2002).

Finally, as a consistency check, we compute the $\Omega_{\rm CIV}$ predicted by our simulation at $z = 6$. The cosmic density parameter relative to the i-th species can be written as (e.g. D'Odorico et al., 2013)

$$\Omega_i(z) = \frac{H_0 m_i}{c\rho_c} \int N_i f_i {\rm d}N_i \,, \tag{2.10a}$$

where ρ_c is the critical density and $f_i(N_i, z)$ is the PDF of the i-th column density N_i. For a discrete set of absorbers indexed by j, the integral can be approximated as (Storrie-Lombardi et al., 1996)

$$\Omega_i(z) \simeq \frac{H_0 m_i}{c\rho_c} \frac{\sum_j N_i^j}{\Delta X} \,, \tag{2.10b}$$

where ΔX is the cosmological path length of the l.o.s. that can be computed using the following relation:

$${\rm d}X = (1+z)^2 \left(\Omega_\Lambda + \Omega_m (1+z)^3\right)^{-1/2} {\rm d}z \,. \tag{2.10c}$$

Additionally, the statistical error, $\delta\Omega_i$, is given by

$$\frac{\delta\Omega_i}{\Omega_i} = \frac{\sqrt{\sum_j (N_i^j)^2}}{\sum_j N_i^j} \,. \tag{2.10d}$$

Using eq.s 2.10, $N_{\rm los}^{\rm tot} = 300$, and taking into account the C IV column density provided by CLOUDY, we find $\Omega_{\rm CIV}^{\rm ERM} = (3.8 \pm 0.1) \times 10^{-8}$ and $\Omega_{\rm CIV}^{\rm LRM} = (3.1 \pm 0.1) \times 10^{-8}$. We also compute $\Omega_{\rm CIV}$ only considering those systems which produce observable absorption lines ($F_{\rm tr} < 0.9$), and which are characterized by $10^{13.4} < N_{\rm CIV}/{\rm cm}^{-2} < 10^{15}$. In this case, we find $\Omega_{\rm CIV}^{\rm ERM} = (2.9 \pm 0.3) \times 10^{-8}$ and $\Omega_{\rm CIV}^{\rm LRM} = (2.3 \pm 0.3) \times 10^{-8}$. Considering the total produced metals ($\Omega_Z^{\rm SFH}$ in Sec. 2.3) and assuming solar abundances, it results $\Omega_{\rm CIV}/\Omega_{\rm C}^{\rm SFH} \simeq 1.6 \times 10^{-2}$. In other words, we predict that through C IV absorption line experiments it is possible to probe $\simeq 2\%$ of the total carbon present in the IGM/CGM.

We note that the $\Omega_{\rm CIV}$ values resulting from our calculations are a factor $\simeq 3-4$ greater then the ones found by D'Odorico et al. (2013). This discrepancy is not surprising, since we are not properly comparing simulations and observations. While our calculations take into account the actual C IV distribution in the simulated box, the observed $\Omega_{\rm CIV}$ is inferred from absorption lines spectra through a Voigt profile fitting procedure. Moreover, we restate that our simulations do not account for radiative transfer effects. This is a crucial point, since the ionizing flux which determines the ionization level of atomic

	Si IV	C IV	Si II	C II	O I
λ_i	1393.7550	1548.1950	1526.7066	1334.5323	1302.1685
f_i	0.5280	0.1908	0.127	0.1278	0.0488

TABLE 2.3: Rest frame wavelengths λ_i and oscillator strengths f_i (Prochaska et al., 2004) for the transition considered in the simulated QSO spectra with metal absorption lines.

species can be dominated by the presence of local sources, rather than the background. In particular, this is relevant for the CGM, which is closer to galaxies and is responsible of strong absorption features.

Constraining the ionization level of the IGM at $z \sim 6$ through metal absorption lines requires both the proper inclusion of radiative transfer effects and an extended statistical analysis (e.g. equivalent width and column density distribution, etc) of the synthetic spectra. We defer to a future study a comprehensive comparison between observations and absorption spectra extracted from our simulations.

2.7 Summary

We have studied cosmic metal enrichment via a suite of ΛCDM hydrodynamical simulations using a customized version of the adaptive mesh refinement code RAMSES to evolve a $(10\ \text{Mpc}\ h^{-1})^3$ volume up to $z = 4$ with 512^3 dark matter (DM) particles, a corresponding number of coarse grid cells and allowing for 4 additional levels of refinement. The subgrid prescription for star formation is based on a local density threshold criterion ($\Delta > \Delta_{\rm th}$) and on a critical metallicity criterion ($Z_{\rm crit} = 10^{-4} Z_\odot$), allowing us to follow the transition from Pop III to Pop II stars. To assess the impact of variations in the unknown Pop III IMF we have investigated three different choices: (a) a standard Larson-Salpeter IMF (SALP), (b) a δ-function describing faint hypernovae (FHN), and (c) a top-heavy IMF allowing for pair-instability supernovae (PISN). We account for thermal feedback from supernovae and implemented a metal-dependent parameterization of stellar yields and return fractions.

This set-up enables the resolution of DM halos masses of $10^{7.5} M_\odot$ with $\simeq 100$ particles and to build a statistically significant sample of galaxies at all redshifts of interest. The two free parameters of our subgrid model (star formation timescale and supernova coupling efficiency) have been fixed by reproducing the observed cosmic star formation rate (SFR, Bouwens et al., 2012, Zheng et al., 2012) and stellar mass densities (SMD, González et al., 2011) at $4 \leq z \lesssim 10$.

By constructing halo catalogues and identifying the associated stars and star forming regions ($\Delta > \Delta_{\rm th}$), it has been possible to analyze the evolution of metal enrichment on galactic scales at two representative redshifts, $z = 6$ and $z = 4$. Galaxies account for $\lesssim 9\%$ of the baryonic mass; the complementary fraction resides in the diffuse medium, which we have classified according to the environmental overdensity into: (a) *voids*, i.e. regions with extremely low density ($\Delta \leq 1$), (b) the true *intergalactic medium* (IGM, $1 < \Delta \leq 10$) and (c) the *circumgalactic medium* (CGM, $10 < \Delta \leq 10^{2.5}$), representing the interface between the IGM and galaxies.

We have computed synthetic spectra of metal absorption lines through the simulated box at $z = 6$. The number density of different ionic species are calculated in post-processing with CLOUDY and by considering two physically motivated and observationally constrained reionization models, i.e. an Early Reionization Model (ERM, $\log(\Gamma_{\rm HI}/{\rm s}^{-1}) = -12.46$ at $z = 6$) and a Late Reionization Model (LRM, $\log(\Gamma_{\rm HI}/{\rm s}^{-1}) = -12.80$).

We have tried to analyze separately the metal enrichment properties of galaxies and diffuse medium for sake of clarity, but obviously the intimate connection between these two components makes it impossible to separate their description completely. Readers mostly interested in galaxies/stars (diffuse gas) can directly refer to Sec. 2.3 (Sec. 2.4); those specifically interested in Pop III stars should also find Sec. 2.5 relevant. The summary of the main results given below is organized in points attempting to keep these distinctions.

1. Between $z = 9$ and $z = 6$ a galactic mass-metallicity relation is established. For star forming regions of mass $M_{\rm SF} \gtrsim 10^{7}{\rm M}_{\odot}$, such relation shows little evolution from $z = 6$ to $z = 4$. In particular, at $z = 4$, galaxies hosting a stellar mass $M_{\star} \simeq 10^{8.5}{\rm M}_{\odot}$ show a mean oxygen abundance of $\log({\rm O}/H) + 12 = 8.19$, consistent with observations (Troncoso et al., 2014).

2. At $z = 4$ such relation extends to $M_{\rm SF} \lesssim 10^{7}{\rm M}_{\odot}$: these are satellite galaxies forming whose star formation has been enabled by the progressive enrichment of the diffuse gas out of which they form. For $10^{6} \lesssim M_{\rm SF}/{\rm M}_{\odot} \lesssim 10^{7}$ the metallicity trend is flat and resembles the one observed in the faintest Local Group dwarf galaxies (e.g. Kirby et al., 2013).

3. The total amount of heavy elements produced by star formation rises from $\Omega_{Z}^{\rm SFH} = 1.52 \times 10^{-6}$ at $z = 6$ to 8.05×10^{-6} at $z = 4$. Metals in galaxies make up to $\simeq 0.89$ of such budget at $z = 6$; this fraction increases to $\simeq 0.95$ at $z = 4$. At $z = 6$ ($z = 4$) the remaining metals are distributed in the three diffuse phases, CGM/IGM/voids, with the following mass fractions: 0.06/0.04/0.01 (0.03/0.02/0.01).

4. In all the diffuse phases a considerable fraction of metals is in a warm/hot ($T\,\mu^{-1} > 10^{4.5}K$) state. In particular, a small but not negligible mass fraction ($\simeq 0.003$) of metals in voids shows $T\,\mu^{-1} \leq 10^{4.5}K$. This implies that these metals must have

been injected at sufficiently early epochs that they had the time to cool as expected in a pre-enrichment scenario.

5. Analogously to the mass-metallicity relation for star forming regions, at $z = 4$ a density-metallicity ($\Delta - Z$) relation is in place for the diffuse phases. Independently of Δ, the IGM/voids show an uniform distribution around $Z \sim 10^{-3.5}\mathrm{Z}_\odot$, while in the CGM Z steeply rises with density up to $\simeq 10^{-2}\mathrm{Z}_\odot$.

6. The geometry of metal bubbles is influenced by the topology of the cosmic web. At $z = 6$, $\sim 40\%$ are spherically symmetric and are mostly found around isolated galaxies; 30% show instead a cylindrical shape which mainly results from merging of bubbles aligned along filaments.

7. The cosmic Pop III star formation history is almost insensitive to the chosen Pop III IMF. Pop III stars are preferentially formed in pockets of pristine ($Z = 0$) gas, well outside polluted regions created by nearby/previous star formation episodes. This supports the "Pop III wave" scenario suggested by Tornatore et al. (2007) and confirmed by Maio et al. (2010).

8. In the PISN case, the Pop II SFR is suppressed by a factor of $\simeq 5$ with respect to the SALP/FHN cases. Because of the higher energy deposition, a pair-instability SN can reach and disrupt a nearby potential star formation site, quenching Pop II formation. Assuming the same star formation timescales for Pop II and Pop III, a PISN scenario is difficult to be reconciled with the observed SFR history, as the feedback from these stars is probably too effective.

9. Metal absorption line spectra extracted from our simulations at $z \sim 6$ contain a greater wealth of information with respect to the Lyα forest. Given the prevailing thermodynamical/ionization conditions of the enriched gas, C IV absorption line experiments can only probe up to $\simeq 2\%$ of the total carbon present in the IGM/CGM. However, metal absorption lines are very effective tools to study reionization.

10. The occurrence of low-ionization metal systems (e.g. O I and C II) in $z \sim 6$ quasar (gamma-ray burst) absorption spectra does not exclude the possibility that the IGM/CGM is on average highly ionized at these epochs. In fact, such systems, although with a lower incidence than in a Late Reionization Model, are also detectable in the Early Reionization Model, which predicts a lower H I fraction ($x_{\mathrm{HI}} \sim 10^{-4}$) at $z \simeq 6$.

As a final remark, we have highlighted the potential problem that chemical feedback might be artificially enhanced in a simulation when the box size becomes smaller or comparable to the pollution radius $\langle R_B \rangle$. Although the box size and resolution have a significant impact on the determination of Pop III cosmic SFR, additional uncertainties come from the treatment of radiative feedback. A proper demonstration would involve a suite of simulations with increasing box size and fixed resolution and a convergence study with fixed box-size and increasing mass resolution. The situation may be worth a closer scrutiny, which we defer to future work.

CHAPTER 3

THE CIRCUMGALACTIC MEDIUM OF HIGH REDSHIFT GALAXIES

The circumgalactic medium (CGM) is the extended interface between the interstellar medium (ISM) of a galaxy and the surrounding intergalactic medium (IGM). This component plays a key role in galactic evolution as it represents a mass reservoir and a repository of the mechanical and radiative energy produced by stars. Due to its low density, the CGM can be almost uniquely traced by absorption line experiments towards background sources, typically quasars. The intervening CGM associated with a foreground galaxy then leaves a characteristic spectral feature. Provided that a sufficiently large sample of galaxies are available it is then possible to statistically determine the Equivalent Width (EW) of a given absorption line as a function of the line of sight (l.o.s.) impact parameter (b).

The CGM has been probed so far up to $z \sim 3$ using absorption lines of both H I (e.g. Pieri et al., 2014, Rudie et al., 2012, 2013) and heavy elements (e.g. Borthakur et al., 2013, Churchill et al., 2013, Liang & Chen, 2014, Nielsen et al., 2013, Steidel et al., 2010). These observations show that the CGM extends up to $b \simeq 10\, r_{\rm vir}$, where $r_{\rm vir}$ is the virial radius of the parent dark matter (DM) halo. An anticorrelation between EW and b is observed; moreover, the EW profiles appear to be self-similar once scaled with $r_{\rm vir}$. Finally Chen (2012) suggested that CGM absorption profiles show no signs of evolution from $z \simeq 2$ to $z \simeq 0$.

In the framework of a ΛCDM cosmological model, the CGM properties can be derived from numerical simulations simultaneously accounting for both large scale ($\simeq$ Mpc) structure and small scale ($\simeq$ kpc) galactic feedback. While such a huge dynamical range makes a truly self-consistent simulation impossible, these difficulties can be overcome by following the unresolved physical scales with subgrid models.

Along these lines, some numerical studies have focused on testing CGM metal enrichment models (e.g. Barai et al., 2013, Crain et al., 2013, Shen et al., 2013); others have investigated the imprint of the last phases of reionization on the IGM/CGM (e.g. Finlator et al., 2013, Keating et al., 2014) or the ISM/CGM overdensity-metallicity (Δ-Z) relation as a function of redshift (see Sec. 2.4.1, in particular Fig. 2.11). Surprisingly, little attention has been devoted so far to understand the physics beneath the observed CGM profile self-similarity and redshift independence.

In this Chapter we show that the previously found Δ-Z relation naturally arises from self-similar nature of the CGM density/metallicity profiles. We use this result to derive an analytical expression for $\mathrm{EW}_{\mathrm{HI}}(b)$ which we then test against synthetic spectra extracted from the simulations and available observational data.

3.1 Numerical simulations

We adopt the simulations described in Sec. 2.1, that – for convenience – are briefly summarized here. Starting from cosmological initial conditions generated at $z = 199$, we use the AMR code RAMSES (Teyssier, 2002) to evolve a $(10\ \mathrm{Mpc}\ h^{-1})^3$ volume until $z = 4$. The DM mass resolution is $6.67 \times 10^5\, h^{-1}\mathrm{M}_\odot$, and the adaptive baryon spatial resolution ranges from $19.53\, h^{-1}$ kpc to $1.22\, h^{-1}$ kpc.

We include subgrid prescriptions for star formation, accounting for supernova (thermal) feedback and implementing metal-dependent stellar yields and return fractions. Our simulation reproduces the observed cosmic star formation rate (Bouwens et al., 2012) and stellar mass densities (González et al., 2011) for $4 \leq z \lesssim 10$.

We define a galactic environment as a connected patch of enriched gas with metallicity exceeding a chosen threshold, i.e. $Z > Z_{\mathrm{th}} \equiv 10^{-7}\mathrm{Z}_\odot$. Within such regions, following a common classification, we identify three different phases according to their gas overdensity: IGM ($\Delta = \rho/\bar{\rho} \leq 10$), CGM ($10 < \Delta \leq 10^{2.5}$), and ISM ($\Delta > 10^{2.5}$).

In Sec. 2.3 (see also App. C), we show how to construct a complete catalogue of galactic environments at a given redshift. To each galactic environment we associate the group of DM halos, of total mass M_{h}, inside its boundary. We denote as "central halo" the most massive halo in each group and "satellites" the remaining ones. Since the central halo dominates the local dynamics, we use its mass (M_{c}) to compute the virial radius of the structure (r_{vir}).

3.1.1 Self-similar Δ and Z profiles

We focus our attention at $z = 4$, the lowest redshift reached by the simulation. At this epoch a Δ-Z relation for the gas is already in place. Fig. 3.1 shows the spherically-averaged radial profiles of the overdensity (upper panel) and metallicity (lower panel), as a function of $x \equiv r/r_{\rm vir}$, for various ($\simeq$ 300) simulated galactic environments characterized by $10^{8.5} \lesssim M_{\rm h} \lesssim 10^{11.5} {\rm M}_{\odot}$.

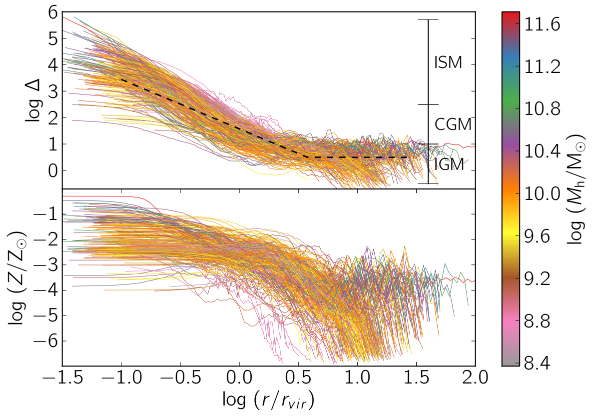

FIGURE 3.1: Overdensity (Δ, upper panel) and metallicity (Z, lower panel) radial profiles of $\simeq$ 300 simulated galactic environments at $z = 4$. Each line refers to a selected environment, and its color corresponds to the associated total DM halo mass ($M_{\rm h}$), as shown in the colorbar. The distance is normalized to $r_{\rm vir}$, the virial radius of the central halo. In the upper panel the black dashed line is the analytical fit to the data (see eq. 3.1).

The overdensity trend is very similar for all galactic environments. In particular, the ISM is located at $x \lesssim 10^{-0.5}$, the CGM spans the radial range $10^{-0.5} \lesssim x \lesssim 10^{0.5}$ and the IGM extends beyond $x \simeq 10^{0.5}$. Hence, the adopted density definition for different gas phases is equivalent to a distance classification[1], similarly to the proposal by Shull et al. (2014).

Generally, one might expect that the shape of the relation depends somewhat on feedback prescriptions (Oppenheimer et al., 2012). However, we note that feedback has been accurately calibrated in to reproduce globally averaged galactic properties (see Sec.s 2.1.1 & 2.2, and Fig. 2.1).

The gas density profile can then be written in terms of the self-similar variable x as a piecewise power-law of index α:

$$\rho_{\rm pp}(x)/\rho_{\rm vir} = \Theta(x_{\rm IGM} - x)x^{-\alpha} + \Theta(x - x_{\rm IGM})x_{\rm IGM}^{-\alpha}\,, \tag{3.1}$$

where $\rho_{\rm vir}$ is the gas density evaluated at the virial radius, Θ is the Heaviside function and $x_{\rm IGM}$ denotes the location where the density approaches a constant value typical of the IGM in the proximity of galactic systems. The best fit values for the parameters are: $\alpha = 1.87 \pm 0.05$, $\rho_{\rm vir}/\bar{\rho} = 37.5 \pm 4.7$ and $x_{\rm IGM} = 3.8 \pm 0.2$. From the fit, we also find the relation $(\rho_{\rm vir}/\bar{\rho})x_{\rm IGM}^{-\alpha} \simeq 3$. In the upper panel of Fig. 3.1, $\Delta_{\rm pp} = \rho_{\rm pp}/\bar{\rho}$ is shown by the black dashed line.

The metallicity (Fig. 3.1, lower panel) is essentially flat in the ISM and rapidly declines in the CGM; this result is independent from the selected environment. The trend is

---

[1] Therefore we will use interchangeably overdensity and distance definitions for the three phases.

however not universal in the IGM, as expected from the results of Sec. 2.4.1, where we showed that Z is only weakly correlated with Δ in the IGM (see Fig. 2.11). Environments associated with massive DM halos ($M_{\rm h} \gtrsim 10^{9.5}{\rm M}_{\odot}$) show an enriched ($Z \simeq 10^{-3.5}{\rm Z}_{\odot}$) IGM up to $x \simeq 10^{1.5}$. Instead, halos with $M_{\rm h} \lesssim 10^{9.5}{\rm M}_{\odot}$, which contain small galaxy groups or even isolated galaxies, only manage to pollute the IGM within $x \lesssim 10$. This trend is discussed in detail in Fig. 13 of P14.

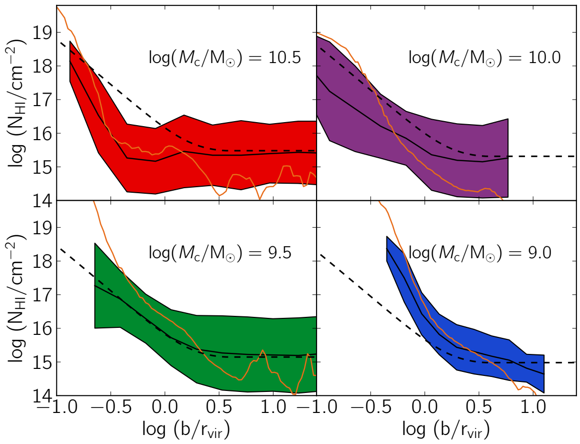

FIGURE 3.2: Neutral hydrogen column density ($N_{\rm HI}$) as a function of the normalized impact parameter ($b/r_{\rm vir}$) for a set of galactic environments with central halo mass $M_{\rm c}$. The mean and the r.m.s. $N_{\rm HI}$ values inferred from the absorption spectra are shown through solid black lines and colored shaded regions, respectively. The solid orange lines represent the average $N_{\rm HI}$ inferred from the simulation (see footnote 3), while the dashed black lines denotes the $N_{\rm HI}$ resulting from the analytical model (eq. 3.2) calculated for $\log(T_{\rm eff}/{\rm K}) = 5$.

Finally, galaxies hosted in halos with masses lower than $\simeq 10^{8.5}{\rm M}_{\odot}$ only show up as satellites (see Sec. 2.3.2, in particular Fig. 2.5). Their effect is perceivable in Fig. 3.1 as a local perturbation to the global Δ and Z trends at $x \gtrsim 1$. The satellite positions resulting from our simulation are in broad agreement with the outcome of the numerical simulation by Khandai et al. (2015), who find a flat satellite distribution at $x \gtrsim 1$ for $M_{\rm h} \sim 10^{10}{\rm M}_{\odot}$ (see their Fig. 10).

3.1.2 Modeling H I absorption

From the fit to the simulated density profile, $\rho_{\rm pp}(x)$, we build a simple analytical model that describes the H I absorption properties (N$_{\rm HI}$ and EW$_{\rm HI}$) of the CGM/IGM.

The H I column density along a l.o.s. is defined as $N_{\rm HI} = \int n\, x_{\rm HI}\, {\rm d}l$, where n is the total hydrogen density, and $x_{\rm HI}$ is the H I fraction. Assuming spherical symmetry, we express $N_{\rm HI}$ through the following relation:

$$N_{\rm HI}(b) = \frac{2}{m_{\rm H}} \int_{b}^{l_{\rm max}} \rho_{\rm pp} x_{\rm HI} \frac{r}{\sqrt{r^2 - b^2}}\, {\rm d}r\,, \tag{3.2}$$

where $\rho_{\rm pp}$ is given in eq. 3.1, b is the impact parameter, $m_{\rm H}$ is hydrogen mass, $l_{\rm max} = \sqrt{b^2 + (\Delta v/H)^2}$, $H = H(z)$ is the Hubble constant and Δv is the velocity window sampled by observations. Assuming local photoionization equilibrium (e.g. Dayal et al., 2008), the H I fraction can be written as $x_{\rm HI} = (1+\xi) - \sqrt{(1+\xi)^2 - 1}$, where

$\xi \equiv (\Gamma_{\rm HI} m_{\rm H})/(2\,\rho_{\rm pp}\alpha_{\rm rec})$, $\alpha_{\rm rec}$ is the recombination rate and $\Gamma_{\rm HI} = \Gamma_{\rm HI}(z)$ is the UV background photoionization rate. Consistent with the simulations (see Sec. 2.1), we use the UV intensity from Haardt & Madau (2012).

The H I Lyα equivalent width can be expressed as follows:

$$\mathrm{EW}_{\rm HI}(b) = \frac{c}{\nu_0^2}\int_0^\infty (1 - \exp(-N_{\rm HI}\sigma_0\phi))\,\mathrm{d}\nu\,, \tag{3.3}$$

where c is the speed of light, ν_0 is the frequency of the Lyα transition, $\phi = \phi((\nu - \nu_0)/\Delta\nu, \Delta\nu)$ is the Voigt profile (e.g. Meiksin, 2009), $\Delta\nu = (\nu_0/c)\sqrt{2K_B T/m_{\rm H}}$ is the thermal Doppler broadening and $\sigma_0 = \pi e^2 f/m_e c$, where f is the oscillator strength, e and m_e are the electron charge and mass, respectively. By combining eq.s 3.1-3.3, we obtain the trend of $\mathrm{EW}_{\rm HI}$ with b, for different values of $r_{\rm vir}$ and T.

The $\mathrm{EW}_{\rm HI}(b)$ dependence on $r_{\rm vir}$, entering through the density dependence on $x = r/r_{\rm vir}$, results in a stretching/compression of the density profile. The temperature T, entering in the expressions for $\alpha_{\rm rec}$ and $\Delta\nu$, regulates both H I at $x \gg x_{\rm IGM}$ and the slope of the $\mathrm{EW}_{\rm HI}$ profile for $x \lesssim x_{\rm IGM}$. For increasing (decreasing) T values, H I is shifted downward (upward) while the slope becomes steeper (shallower). It is worth noticing that we are assuming a single temperature value both for the IGM and CGM. Moreover, we are neglecting turbulence, which may affect the Doppler broadening of CGM absorbers (e.g. Iapichino et al., 2013). Therefore, T must be regarded as an "effective temperature"; to make it clear we will use $T_{\rm eff}$ to indicate this quantity.

3.2 Testing the H I absorption model

We are now ready to test our model both against simulated QSO absorption spectra and real data.

3.2.1 Synthetic H I absorption spectra

We compute mock QSO absorption spectra along several l.o.s. drawn through the simulated box. The technique adopted to compute the H I optical depth is detailed in Gallerani et al. (2006). In order to reproduce the mean transmitted flux observed at $z = 4$ ($F_{\rm mean} = 0.41$, Becker et al. (2013)) the intensity of the UV ionizing background (Haardt & Madau, 2012) assumed in the simulation is rescaled upwards by a factor 6.6, resulting into a photoionization rate $\log(\Gamma_{\rm HI}/\mathrm{s}) = -12$. We also include observational artifacts in our simulated spectra, following Rudie et al. (2013), a work based on HIRES spectra. We smooth the synthetic spectra to a resolution $R = 45000$, add to each pixel

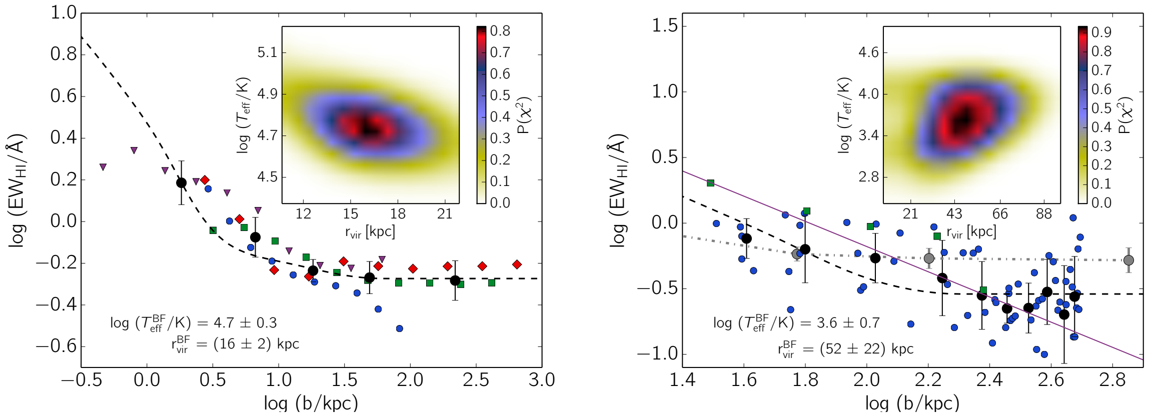

FIGURE 3.3: Neutral hydrogen equivalent width (EW$_{\mathrm{HI}}$) profiles. **Left panel**: *simulated vs analytical profiles*. Simulated profiles for different galactic environments are indicated through red diamonds, purple downwards triangles, green squares, and blue circles for $M_c/M_\odot = 10^{10.5}, 10^{10}, 10^{9.5}$ and 10^9, respectively. Black circles with errorbars indicate the rebinned simulated data (see the text for the details). The black dashed line indicates the best fit analytical model, whose parameter ($T_{\mathrm{eff}}^{\mathrm{BF}}$ and $r_{\mathrm{vir}}^{\mathrm{BF}}$) values are given. The inset shows the χ^2 probability of the analytical model (eq.s 3.1-3.3) as a function of T_{eff} and r_{vir}. **Right panel**: *simulated vs observed profiles*. Observations from Liang & Chen (2014, $z \simeq 0.01$, blue circles) and Steidel et al. (2010, $z \simeq 2.2$, green squares). The solid violet line represents the model by Chen et al. (1998, 2001), and the grey circles linked by the dashed-dotted line show the rescaled EW$_{\mathrm{HI}}(b)$ profile obtained from synthetic spectra at $z = 4$ (see the text for details). Additional notation is as in the left panel.

a Gaussian random deviate, yielding a signal-to-noise ratio $S/N = 100$, and we finally rebin the simulated transmitted flux in channels of width 0.4 A.

Among the l.o.s. extracted from the simulations, we select the ones passing through a specific galactic environment, defined by its central halo M_c and its corresponding r_{vir}. The sample of l.o.s. considered encompasses a wide range of impact parameters, namely 10^{-1}-10^2 r_{vir}.

3.2.2 Largest gap statistics

Along each l.o.s, we identify the CGM absorption feature with the largest spectral gap[2] found in the corresponding synthetic spectrum (Gallerani et al., 2008a,b). In order to check that largest gaps correctly identify CGM absorption features, we compute the N_{HI} along their corresponding l.o.s. paths, for different b values, and for a set of galactic environments characterized by $M_c/\mathrm{M}_\odot = 10^{10.5}, 10^{10}, 10^{9.5}$ and 10^9, that correspond at $z = 4$ to $r_{\mathrm{vir}}/\mathrm{kpc} = 21, 14, 9.6$ and 6.5, respectively.

---

[2] Spectral gaps are defined as contiguous regions of the spectrum having an optical depth $\tau > 2.5$ over rest-frame intervals > 1 A (Croft, 1998).

The results from a sample of 3000 l.o.s. are shown in Fig. 3.2. Superimposed to the $N_{\rm HI}$ profiles obtained from the synthetic spectra analysis, are the average $N_{\rm HI}$ values inferred from the simulations[3] and the column density resulting from the analytical model (eq. 3.2) calculated for $\log(T_{\rm eff}/{\rm K}) = 5$. Fig. 3.2 shows that the largest gap statistics properly identifies CGM absorption features in H I absorption spectra.

This technique is particularly promising for studying the CGM absorption properties for high-z ($z > 4$) quasar spectra. At these redshifts, the maximum observed transmitted flux drops below 50% in the Lyα forest (Songaila, 2004). The resulting large uncertainties in the continuum determination may therefore hamper a proper Voigt profile analysis.

3.2.3 Comparison with simulations

As a next step, we compute the EW$_{\rm HI}$ of the absorption features identified through the largest gap statistics as a function of the b parameters, for the galactic environments presented in Fig. 3.2. The results are shown in the left panel of Fig. 3.3 through red diamonds, purple downwards triangles, green squares, and blue circles for $M_c/M_\odot = 10^{10.5}, 10^{10}, 10^{9.5}$ and 10^9, respectively. In the same figure, black circles and corresponding error bars represent mean and r.m.s. values obtained by averaging the EW$_{\rm HI}$ profiles of the 4 different galactic environments into bins of width δb such that $\log(\delta b/{\rm kpc}) \simeq 0.5$. As expected (see eq. 3.3), the EW$_{\rm HI}$ profiles follow the $N_{\rm HI}$ trend (Fig. 3.2), namely EW$_{\rm HI}$ decreases with b.

Finally, we fit the averaged EW$_{\rm HI}$ profile resulting from the synthetic spectra analysis through our analytical model, finding the following best fit parameters: $\log({\rm T}_{\rm eff}^{\rm BF}/{\rm K}) = 4.7 \pm 0.3$ and $r_{\rm vir}^{\rm BF} = 16 \pm 2$ kpc. The inferred $T_{\rm eff}^{\rm BF}$ value agrees with typical values of the CGM/IGM temperature (see Sec. 2.4.1, in particular Fig. 2.8) and $r_{\rm vir}^{\rm BF}$ is consistent with the average virial radius of the galactic environments considered, namely $r_{\rm vir}^{\rm mean} = 13 \pm 6$ kpc. This result represents a solid consistency check of our model which allows us to repeat the same experiment on real data.

3.2.4 Comparison with observations

In the right panel of Fig. 3.3, we compare our model with observations. Blue circles are the EW$_{\rm HI}$ derived at $z = 0.01$ by Liang & Chen (2014); black circles and corresponding error bars represent mean and r.m.s. values obtained by averaging the same observational data into bins ~ 40 kpc large.

---

[3] For each l.o.s., $N_{\rm HI} = \int n\, x_{\rm HI}\, dl$, where the integration limits correspond to the borders of the environment, which in turn depend on $Z_{\rm th}$. Changing the metallicity threshold marginally affects the results: using $Z_{\rm th} = 10^{-6}{\rm Z}_\odot$ yields a variation of $\delta N_{\rm HI} \lesssim 10^{14}{\rm cm}^{-2}$ for the inferred column density. The orange lines are obtained by averaging $N_{\rm HI}$ over $\sim 10^5$ l.o.s..

For this comparison the model is calculated with $\log(\Gamma_{\rm HI}/{\rm s}) = -13$, i.e. the value at $z = 0.01$ given by Haardt & Madau (2012). By fitting[4] observations with our analytical model we find $\log(T_{\rm eff}^{\rm BF}/K) = 3.6 \pm 0.7$ and $r_{\rm vir}^{\rm BF} = 52 \pm 22$ kpc. $T_{\rm eff}^{\rm BF}$ provides only an indicative value for the average temperature of the CMG/IGM. Although $r_{\rm vir}^{\rm BF}$ is consistent within $1.2\,\sigma$ with the mean virial radius $r_{\rm mean} = 144 \pm 74$ kpc quoted by Liang & Chen (2014), we note that our model favors smaller $r_{\rm vir}$ values.

The dashed black line in the right panel of Fig. 3.3 represents our best fit model, while the violet solid line shows the model from Chen et al. (1998, 2001, hereafter C-model). Both the C-model and our best fit are in agreement with Liang & Chen (2014) observations up to $b/{\rm kpc} \sim 10^2$, i.e. in the CGM range ($b \sim 4\,r_{\rm vir}^{\rm BF}$). On the other hand, for $b/{\rm kpc} \gtrsim 10^{2.5}$, the C-model declines more steeply than data, while our best fit model properly reproduces the observed flat trend.

The gray circles linked by the dashed dotted line show the ${\rm EW}_{\rm HI}(b)$ profile obtained from $z = 4$ synthetic spectra, once rescaled to the $r_{\rm vir}^{\rm BF}$ of the model which reproduces $z = 0.01$ observations. The good agreement between the synthetic and observed ${\rm EW}_{\rm HI}$(b) profiles, both shows that our modelling of the CGM reproduces observations, and favors the scenario suggested by Chen (2012) of a redshift independent CGM profile. As a further support to this idea we also show (green squares) CGM observations at $z \simeq 2.2$ by Steidel et al. (2010), which are perfectly consistent both with $z = 0.01$ observations and with the ${\rm EW}_{\rm HI}(b)$ profile obtained from $z = 4$ synthetic spectra.

3.3 Projected Δ-Z relation

Inspired by the Δ-Z relation found in the ISM/CGM, we investigate whether the mean metallicity along a simulated l.o.s. $\langle Z\rangle$ correlates with the $N_{\rm HI}$ distribution of our galactic environments. We compute $\langle Z\rangle$ through the following equation: $\langle Z\rangle = N_{\rm HI}^{-1}\int n\,x_{\rm HI} Z\,{\rm d}l$.

In Fig. 3.4, we plot the probability distribution function (PDF) of $N_{\rm HI}$ and $\langle Z\rangle$ for a simulated environment characterized by $M_{\rm h} \simeq 10^{11}{\rm M}_{\odot}$. Consistently with observations of the CGM in the proximity of $M_{\rm h} \simeq 10^{11}{\rm M}_{\odot}$ halos (i.e. Liang & Chen, 2014), we find an upper limit of $\langle Z\rangle < 10^{-1}{\rm Z}_{\odot}$ in the simulated CGM.

Fig. 3.4 shows that $\langle Z\rangle$ tightly correlates with $N_{\rm HI}$ only in the ISM, which displays both high column density ($N_{\rm HI} \gtrsim 10^{19}{\rm cm}^{-2}$) and high mean metallicity ($\langle Z\rangle \gtrsim 10^{-1.5}{\rm Z}_{\odot}$) values. However, for the CGM/IGM, the underlying tight Δ-Z correlation is somewhat blurred, once projected into the $N_{\rm HI}$ and $\langle Z\rangle$ variables, which present larger dispersions.

---

[4] Supported by the lack of evolution of CGM profiles from $z = 2$ to $z = 0$ (Chen, 2012), we assume $\rho_{\rm pp}$ to be redshift independent in eq. 3.1.

This result implies that H I absorption studies do not allow to precisely constrain the CGM metallicity, as a consequence of a strong $N_{\rm HI} - \langle Z \rangle$ degeneracy.

Such a degeneracy can only be broken by adding metal absorption line information. In this case, proximity effect of ionizing sources may turn out to be crucial in determining the different ionization levels of metal atoms. We defer to a future work a proper inclusion of these radiative transfer effects in our simulation. This will allow us to correctly interpret high-z CGM/IGM metal absorption line observations (e.g. D'Odorico et al., 2013, Díaz et al., 2014).

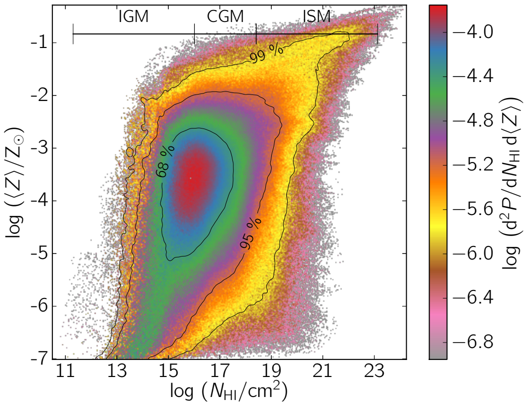

FIGURE 3.4: Probability distribution function (PDF) of mean metallicity ($\langle Z \rangle$) and column density ($N_{\rm HI}$) for a $M_{\rm h} \simeq 10^{11}{\rm M}_{\odot}$ galactic environment. The color bar quantifies the PDF weighted by the l.o.s. number. The black solid lines indicate $68\%, 95\%$ and 99% confidence levels.

3.4 Summary

We have used the cosmological metal enrichment simulation presented in Chapter 2 to study the CGM/IGM properties of high-z galaxies, by analyzing the H I absorption profiles of the simulated galactic environments. The main results can be summarized as follows:

1. At $z = 4$, the gas radial density profiles in galactic environments are self-similar once scaled with the virial radius of the system, and can be fitted by a piecewise power-law ($\rho_{\rm pp}$, eq. 3.1). We have used this result to predict the H I equivalent width (EW$_{\rm HI}$) as a function of the impact parameter b (eq.s 3.2 and 3.3).

2. Using simulations, we have produced mock H I absorption spectra which are then analyzed using the largest gap statistics to identify CGM absorption features. As a consistency check of the EW$_{\rm HI}$ model, we have verified that it can reproduce the analogous profile deduced from the synthetic spectra.

3. Our analytical model (calibrated at $z = 4$) successfully reproduces CGM/IGM observations both at $z \simeq 0$ (Liang & Chen, 2014) and at $z \simeq 2.2$ (Steidel et al., 2010), possibly suggesting that the density profiles evolve very weakly with redshift.

4. We have investigated the relation between the mean metallicity along a simulated l.o.s. $\langle Z \rangle$ and the $N_{\rm HI}$ distribution of galactic environments. Consistently with

metal absorption line observations of Liang & Chen (2014), we find $\langle Z \rangle < 10^{-1}\mathrm{Z}_\odot$ in the CGM; however, the strong $N_{\mathrm{HI}} - \langle Z \rangle$ degeneracy does not allow to constrain the CGM metallicity through H I absorption studies alone, and metal absorption line information is required to this goal.

CHAPTER 4

MAPPING METALS AT HIGH REDSHIFT WITH FAR-INFRARED LINES

In spite of the impressive progresses produced by deep optical/IR surveys (Bouwens et al., 2014, Dunlop, 2013b, Madau & Dickinson, 2014) in identifying galaxies well within the Epoch of Reionization, very little is known about the metallicity and other properties of these systems, including feedback (e.g. Dayal et al., 2014) and interactions with their environment (e.g. Barnes et al., 2014). The situation is slightly better for what concerns the IGM, where metal enrichment is typically studied by measuring the abundance of heavy elements at different cosmic times with quasar (QSO) absorption line spectroscopy (e.g. Becker et al., 2009, D'Odorico et al., 2013, Ryan-Weber et al., 2009, Simcoe et al., 2011, Songaila, 2005) and – more recently – with gamma-ray bursts soft X-ray absorption (e.g. Behar et al., 2011, Campana et al., 2010, 2015). These observations show that the diffuse IGM is enriched at metallicity $Z \gtrsim 10^{-3.5} \mathrm{Z}_{\odot}$ at any overdensity (Δ) and z probed so far (Meiksin, 2009). As the gas left over by the Big Bang is (virtually) metal-free, understanding how and when the first metals were produced holds the key of many structure formation processes.

As a consequence of the paucity of standard luminous lighthouses prior to reionization (Barkana & Loeb, 2001, Ciardi & Ferrara, 2005), the enrichment at $z \gtrsim 6$ cannot be efficiently studied with absorption line experiments. Additionally, at high-z the detection of most metal tracers becomes increasingly difficult. For example, C IV metal absorption line detections at high-z are rare since the C IV doublet shifts into the near-infrared. In this spectral regions observations become challenging because of increased OH emission from the sky and severe telluric absorption.

The above situation is going to change very soon thanks to the advent of the Atacama

Large Millimeter-submillimeter Array (ALMA). This observatory gives us access to far-infrared (FIR) and sub-mm spectroscopy, where metal lines carrying information about the energetics of the interstellar medium and outflows are found. FIR emission lines are a powerful tool to study high-redshift (z) galaxies, since – unlike Lyα – they are not affected neither by the increasing IGM neutral fraction at $z \gtrsim 6$ nor by the presence of dust.

In particular, the [C II] $(^2P_{3/2} \rightarrow {}^2P_{1/2})$ line at 157.74 μm is the brightest FIR emission line, i.e. it can account for $\sim 1\%$ of the total infrared luminosity of galaxies (e.g. Crawford et al., 1985, Madden et al., 1997). Therefore, [C II] emission can be used to trace and characterize $z \sim 6$ galaxies (e.g. Carilli & Walter, 2013). Thanks to its resolution and sensitivity, ALMA offers the unique opportunity to search for [C II] emission from the first galaxies. Understanding the links between star formation, ISM structure and metal enrichment, also provides key insights in the environments in which these early galaxies formed.

In addition to tracing the ISM of galaxies, FIR resonant lines correspond to transitions that are excited via a resonant scattering process of Comic Microwave Background (CMB) photons on heavy element atoms present in the IGM (e.g. Maoli et al., 1996, de Bernardis et al., 1993). These resonant transitions are available for essentially all the most abundant species, e.g. C, N, O, Si, S and Fe, in the mid-IR and FIR wavelength ranges (e.g. Basu et al., 2004).

As a result, IGM metals can produce CMB spectral distortions and spatial fluctuations that can be used to extract unique information on the cosmic metal enrichment process, like, for example, spatial distribution maps of a given metal species. Conceptually, this experiment is similar to QSO absorption line studies, but it uses the CMB as a background source; however, the method has the enormous advantage that every pixel in a sky map can act as a source against which metal lines may appear either in emission or absorption.

Various works (e.g. Basu, 2007, Maoli et al., 2005, Schleicher et al., 2008) have proposed CMB fluctuations/distortions as a tool to trace the smooth distribution of metals and molecules in the post-recombination Universe ($z \gg 10$). These fluctuations typically affect the first CMB multipoles – at $l \lesssim 10^2$, large angular scales ($\theta \sim 1\,\mathrm{deg}$) – and they will be hopefully seen by *Planck* successors (e.g. Chluba, 2014). On smaller scales – $\theta \sim 10''$ ($l \gtrsim 10^5$) – CMB fluctuations in the FIR can be used to map the enriched IGM surrounding the first galaxies ($z \gtrsim 10$).

Here we present a model based on detailed Adaptive Mesh Refinement hydrodynamical cosmological simulations, that allows us to simultaneously compute both the [C II] line emission from early galaxies and the expected level and statistical properties of CMB fluctuations arising from intergalactic C II resonant scattering.

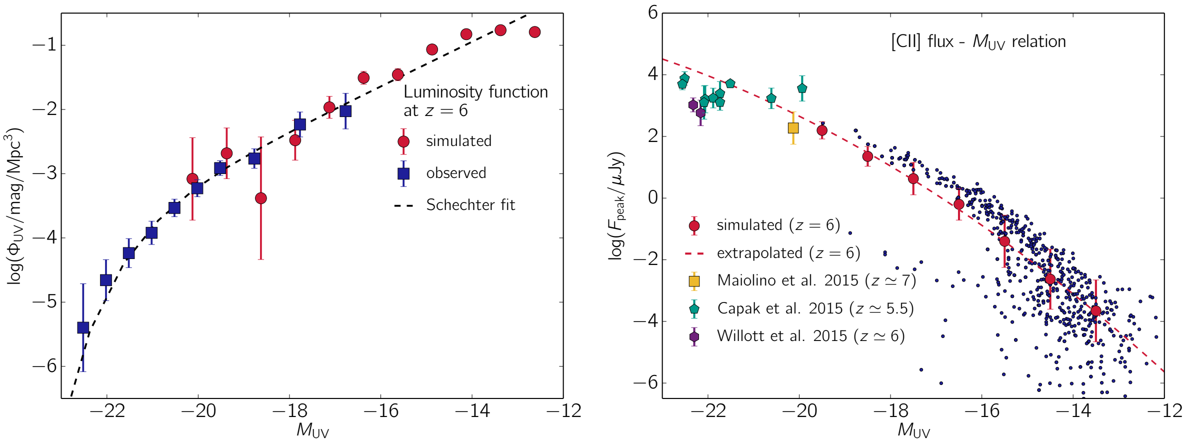

FIGURE 4.1: **Left panel**: UV luminosity function, Φ_{UV} at $z = 6$. Red circles represent the simulated Φ_{UV}; blue squares denote the observed Φ_{UV}, inferred from a composite collection of HST datasets (Bouwens et al., 2014); black dashed lines are the Schechter fit (Bouwens et al., 2014) to the observations. **Right panel**: [C II] flux as a function of M_{UV} at $z = 6$ (blue small circles); the same relation binned in $\Delta M_{UV} = 1$ intervals is shown by red circles. The red errorbars correspond to the r.m.s. variance within the magnitude intervals; The red dashed line is the best fit to the relation. Also plotted are the data from recent high-z observations from Capak et al. (2015), Maiolino et al. (2015), Willott et al. (2015) with yellow squares, green pentagons and violet hexagons, respectively.

The Chapter is organized as follows. In Sec. 4.1, we describe our model, introducing the adopted high-z cosmic metal enrichment simulation (Sec. 4.1.1). We postprocess the simulation to account for [C II] galaxy emission (Sec. 4.1.2) and CMB fluctuations (Sec. 4.1.3), and analyze the properties of the simulated CMB fluctuations in Sec. 4.2. Then, we construct and analyze mock ALMA observations of [C II] galaxy emission and CMB fluctuations (Sec. 4.3). Finally, we propose and discuss an observational strategy for the detection of [C II] galaxy emission and metal-induced CMB fluctuations (Sec. 4.4). Conclusions are given in Sec. 4.5.

4.1 Model

4.1.1 Cosmological simulations

We start from the suite of cosmological hydrodynamical metal enrichment simulations presented in Sec. 2.1.

Here we recall that, to compute the ionization state of the various atomic species, we postprocess the simulation outputs using the photoionization code CLOUDY (Ferland et al., 1998). We account both for the UVB intensity at 912 A (J_ν), and the density (n), kinetic temperature (T_k), and metallicity (Z) of the gas.

We adopt the following classification for the baryonic gas: (i) the interstellar medium (ISM) defines highly overdense gas ($n/n_{\rm mean} = \Delta \geq 10^3$); (ii) the *true* intergalactic medium (IGM) is characterized by $\Delta \leq 10$; (iii) the circumgalactic medium (CGM) represents the interface between the IGM and ISM ($10 < \Delta < 10^3$). In Sec. 3.1.1 we have shown that the adopted classification is consistent with the one proposed by Shull (2014), based on the distance r between the gas and the center of the galaxy. Specifically (i) the ISM is located within the galaxy virial radius ($r_{\rm vir}$), (ii) the IGM at $r/r_{\rm vir} \gtrsim 5$ and (iii) the CGM at $1 \lesssim r/r_{\rm vir} \lesssim 5$.

We showed that galaxies develop a stellar mass-metallicity ($M_\star$-$Z_\star$) relation by $z = 6$. For $M_\star > 10^7 {\rm M}_\odot$, the stellar metallicity ($Z_\star$) increases with increasing stellar mass, while for $M_\star \lesssim 10^7 {\rm M}_\odot$, $Z_\star$ is constant. This means that, while massive galaxies are able to retain most of their metals, low mass galaxies are prone to metal ejection because of their swallower potential well. This indicates that at high-z low mass galaxies are the main driver of metal enrichment in the IGM (e.g. Ferrara, 2008). In agreement with previous numerical studies (e.g. Dayal et al., 2013), the $M_\star$-$Z_\star$ relation shows little evolution from $z = 6$ to $z = 4$, for galaxies with $M_\star \simeq 10^7$. Our results are consistent with the metallicity evolution suggested by recent observations of $3 < z < 5$ star forming galaxies (Troncoso et al., 2014).

We find that (i) most of the gas resides in the IGM, (ii) the denser CGM contains about 15% of the baryons and (iii) the ISM accounts only for a small fraction of the total mass ($\simeq 7\%$). On the other hand, at any given redshift the enriched gas is mostly found near the metal production site, i.e. in the ISM; less than 10% in mass of the produced metal can reach the IGM/CGM. In particular, at $z = 4$, a Δ-Z relation is in place: the IGM shows an uniform distribution around $Z \simeq 10^{-3.5} {\rm Z}_\odot$, in the CGM Z steeply rises with Δ up to $10^{-2} {\rm Z}_\odot$ and the ISM has $Z \simeq 10^{-1} {\rm Z}_\odot$. A considerable fraction ($\gtrsim 50\%$) of the enriched IGM/CGM is in an hot state ($T_k \gtrsim 10^{4.5}$K), meaning that most of the carbon is in C IV. Our analysis shows that C IV absorption line experiments can only probe $\simeq 2\%$ of the total produced carbon.

Our results are in agreement with previous numerical studies in terms of the baryon thermodynamical state (e.g. Cen & Chisari, 2011, Rasera & Teyssier, 2006), the evolution of the metal filling factor (e.g. Johnson et al., 2013, Oppenheimer et al., 2009) and the Δ-Z relation (e.g. Gnedin & Ostriker, 1997, Oppenheimer et al., 2012). Additionally, the preliminary analysis of synthetic spectra extracted from the simulation is consistent with recent observations of metal absorption lines (D'Odorico et al., 2013).

As a further consistency check, we test the UV luminosity function ($\Phi_{\rm UV}$) extracted from Chapter 2 simulation against observations of $z = 6$ galaxies. For each galaxy in our simulation, $M_{\rm UV}$ is calculated with STARBURST99 (Leitherer et al., 2010), using $Z_\star$

and the stellar age as input parameters. In the left panel of Fig. 4.1, we plot the simulated and observed $\Phi_{\rm UV}$ with red circles and blue squares, respectively. The observations are taken from a composite collection of HST datasets (Bouwens et al., 2014), and we additionally plot the Schechter fit to such observations with a black dashed line. The simulated $\Phi_{\rm UV}$ well matches the observed UV luminosity function for $-20 \lesssim M_{\rm UV} \lesssim -16$. Additionally, the simulated $\Phi_{\rm UV}$ is in fair agreement with the Schechter fit extrapolated at $-16 \lesssim M_{\rm UV} \lesssim -12$. Note that, for the simulated $\Phi_{\rm UV}$, the bright end is around $M_{\rm UV} \sim -19$, where the large scatter is due to the limited simulated volume.

4.1.2 [C II] emission from the ISM of high-z galaxies

Starting from Chapter 2 simulations, we compute the [C II] emission at 157.74 μm due to the $^2P_{3/2} \rightarrow {}^2P_{1/2}$ forbidden transition of ionized carbon in the ISM of galaxies. The [C II] line is the dominant coolant of the galaxy interstellar medium and can be collisionally excited under conditions present in different ISM phases, e.g. in the cold and warm neutral medium (CNM, WNM), in high density photodissociation regions (PDRs), and even in the ionized gas (Abel, 2006, Tielens & Hollenbach, 1985, Vallini et al., 2013, Wolfire et al., 1995, 2003).

In our cosmological hydrodynamic simulations, we cannot resolve sub-kpc scales, that are typical for different ISM structures (CNM, WNM and PDRs). To overcome this problem, we account for [C II] emission[1] from the ISM of high-z galaxies by adopting the model presented by Vallini et al. (2013, 2015, V15 hereafter). V15 predicts the [C II] emission from CNM, WNM and PDRs within individual galaxies as a function of their metallicity ($Z_\star$) and star formation rate (SFR). The V15 model is based on the radiative transfer simulation of a high-z galaxy; it includes a subgrid treatment for computing the thermodynamical equilibrium of the diffuse neutral medium (on $\simeq 60\,$pc scales); it allows to localize molecular clouds within the galaxy (on $\simeq 1-10\,$pc scales) and to compute the corresponding [C II] emission by means of the PDR code UCL_PDR (Bell et al., 2005).

---

[1] In the present Chapter, we focus on [C II] emission from $z \simeq 6$ galaxies. However, we note that the V15 model can be readily extended to compute the emission of fine structure lines from other heavy elements, such as, e.g. [N II] at 122 μm and [O I] at 63 μm (Vallini et al., 2013).

According to the V15 model[2], the [C II] galaxy luminosity ($L_{\rm CII}$) depends on the galaxy SFR and metallicity through the following fitting formula:

$$\log\left(L_{\rm CII}\right) = 7.0 + 1.2\,\log({\rm SFR}) + 0.021\,\log(Z_\star) + 0.012\,\log({\rm SFR})\log(Z_\star) - 0.74\log^2(Z_\star)\,, \tag{4.1}$$

where $L_{\rm CII}$, SFR and $Z_\star$ are in units of $L_\odot$, ${\rm M}_\odot\,{\rm yr}^{-1}$ and ${\rm Z}_\odot$, respectively. The V15 predictions are consistent with [C II] observations of local metal-poor dwarf galaxies (De Looze et al., 2014) and have been used to interpret high-z LAEs and LBGs [C II] observations (e.g. González-López et al., 2014, Ota et al., 2014). For each galaxy in the simulation we calculate $L_{\rm CII}$ by using $Z_\star$ and SFR mass averaged values provided by the simulation (see also Yue et al., 2015).

We calculate the relation between [C II] and UV emission. In the right panel of Fig. 4.1, we show the [C II] flux as a function of $M_{\rm UV}$ for the simulated galaxies at $z = 6$ and for various $z = 5 - 7$ ALMA observations (Capak et al., 2015, Maiolino et al., 2015, Willott et al., 2015). The simulated relation is shown as a scatter plot and binned in $\Delta M_{\rm UV} = 1$ intervals. The plot shows a clear correlation between [C II] flux and UV magnitude for the simulated galaxies, with a Spearman correlation coefficient of $\simeq -0.78$. The best fit formula for the relation is

$$\log(F_{\rm peak}/\mu{\rm Jy}) = -27.205 - 2.253\,M_{\rm UV} - 0.038\,M_{\rm UV}^2. \tag{4.2}$$

Using eq. 4.2 we can slightly extrapolate the simulated relation to $M_{\rm UV} < -20$, and directly compare it with recent ALMA observations (right panel of Fig. 4.1), i.e. a [C II] detection in a $z \simeq 7$ LBG (Maiolino et al., 2015, yellow square), observations of several "normal" ($\sim L_\star$) galaxies at $z \simeq 5 - 6$ (Capak et al., 2015, green pentagons) and 2 LBGs at $z \simeq 6$ (Willott et al., 2015, violet hexagons). Our model is in good agreement with the observations and local determinations ($z \simeq 0$) of the $L_{\rm CII}$-SFR relation (De Looze et al., 2014), as we discuss in more details in Sec. 4.4.

4.1.3 CMB scattering from intergalactic metals

The IGM and CGM are not seen in emission, since their typical densities are too low ($n < 0.1$ cm^{-3}) for the upper levels of the [C II] transition to be efficiently populated

---

[2] The V15 model assumes that H II regions provide only a negligible contribution to the [C II] emission (González-López et al., 2014, in particular see Fig. 8). However, the relative fraction of [C II] emission arising from H II regions is not clearly known. As an indicative value, Vasta et al. (2010) observe a median contribution of $\simeq 30\%$. For a more detailed discussion, we address the interested reader to Yue et al. (2015).

through collisions with electrons and/or protons (Gong et al., 2012, Suginohara et al., 1999). In this case the spin temperature of the transition approaches the CMB one[3].

As a result a C II ion at rest with respect to the CMB cannot show up in emission or absorption against this background (e.g. Maoli et al., 1996, da Cunha et al., 2013, de Bernardis et al., 1993). However, if the ion has a peculiar velocity, for example approaching with a velocity $v_{\rm p}$, it will receive a larger (i.e. Doppler-boosted) CMB photon flux in the direction of its motion. As CMB photons are resonantly scattered (e.g. Basu, 2007, Basu et al., 2004, Schleicher et al., 2008) by an atomic transition of frequency $\nu_0 \simeq 1901$ GHz the result is an emission feature in the CMB spectrum at $\nu_{\rm obs} = \nu_0/(1+z)$. In the case of a receding C II ion, the opposite situation occurs, resulting into an absorption feature. Therefore, C II ions in the IGM and CGM are expected to generate CMB spectral distortions whose intensity depends both on the their abundance and peculiar velocity, the latter being of the order of $\sim 50\,{\rm km\,s^{-1}}$.

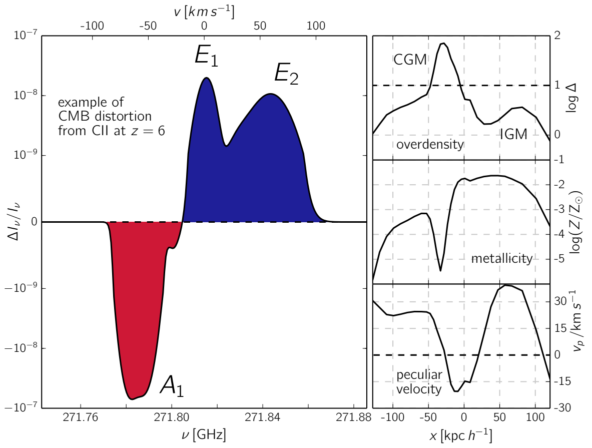

FIGURE 4.2: [C II] CMB spectral distortions/fluctuations from a simulated line of sight (l.o.s.) at $z = 6$. **Left panel**: intensity fluctuations ($\Delta I_\nu/I_\nu$) as a function of frequency (ν, lower axis) and velocity (v, upper axis). Absorption and emission features are highlighted in red and blue, respectively, and the corresponding peaks are labelled with A_i and E_i. Note that integration in the shown bandwidth ($\Delta\nu \simeq 0.1$ GHz) yields $\Delta I/I \simeq -7\times10^{-7}$. **Right panel**: overdensity (Δ, top), metallicity (Z, center) and peculiar velocity (v_p, bottom) for the [C II] metal patch responsible for the fluctuations ($|\Delta I_\nu/I_\nu| > 0$) as a function of comoving distance (kpc h^{-1}). In the overdensity plot our Δ based IGM/CGM definition is marked with a dashed black line. In the peculiar velocity plot $v_p = 0$ is marked with a dashed black line. The origins of both the velocity (left panel) and distance (right panel) axis are shifted for displaying purpose.

The differential amplitude ΔI_ν of the signal with respect to the CMB intensity I_ν is given by (Maoli et al., 1996):

$$\Delta I_\nu/I_\nu = \left(1 - e^{-\tau_\nu}\right)(3-\alpha_\nu)(v_{\rm p}/c) \quad (4.3)$$

where $\alpha_\nu = \nu({\rm d}I_\nu/{\rm d}\nu)/I_\nu$ is the CMB spectral index and the optical depth (τ_ν) can be written as (e.g. Gallerani et al., 2006, , see also Sec. 3.1.2):

$$\tau_\nu = f_{\nu_0}\left(\pi e^2/m_e\nu_0\right) N_{\rm CII}\psi\,, \quad (4.4)$$

---

[3] Gong et al. (2012) have shown that the IGM/CGM spin temperature of the [C II] transition is close to the CMB temperature up to $z \simeq 2$. At lower z, the soft UV background pumping effect may be sufficiently strong to decouple the spin temperature from the CMB temperature.

where f_{ν_0} is the oscillator strength of the [C ii] transition (e.g. Basu et al., 2004), e and m_e are the electron charge and mass, $N_{\rm CII}$ is the [C ii] column density[4], $\psi = \psi((\nu - \nu_0)/\Delta\nu_D)$ is the normalized line profile (e.g. Meiksin, 2009), $\Delta\nu_D = (\nu_0/c)\sqrt{2k_B T_k/m_{\rm C}}$ is the thermal Doppler broadening, k_B the Boltzmann constant, $m_{\rm C}$ the carbon atom mass and c the speed of light. We specify that we are focusing on CMB fluctuations produced by C ii ions, but the same formalism can be extended to other fine structure lines.

In Fig. 4.2 we show an example of [C ii]-induced CMB distortions/fluctuations[5] for a single line of sight (l.o.s.) extracted from a simulation snapshot centered at $z = 6$. In the left panel we plot $\Delta I_\nu/I_\nu$ as a function of frequency (ν, lower axis) and velocity (v, upper axis); in the right panel, the metal patch responsible for the fluctuations is depicted by plotting the relevant physical characteristics (from top to bottom Δ, Z and v_p) as a function of comoving distance (kpc h^{-1}) along the simulated l.o.s.. The origins of the velocity (left panel) and distance (right panel) axis are shifted for displaying purpose.

Absorption ($\Delta I_\nu/I_\nu < 0$) and emission ($\Delta I_\nu/I_\nu > 0$) features are highlighted with a filled red and blue region, respectively. At $\nu \simeq 271.78$ GHz we can see a single absorption peak (labelled A_1 in the Figure); the emission is instead characterized by a double peaked structure: E_1 at $\nu \simeq 271.81$ GHz and E_2 at $\nu \simeq 271.85$ GHz. Both A_1 and E_1 have FWHMs of order $\simeq 20\,{\rm km\,s^{-1}}$, while the FWHM of E_2 is larger, $\simeq 40\,{\rm km\,s^{-1}}$. The l.o.s. intersects the metal patch for $\simeq 0.2\,{\rm Mpc}\,h^{-1}$. The CMB interacts with a CGM peak ($\Delta \simeq 10^2$) at $x \simeq -30\,{\rm kpc}\,h^{-1}$ and an IGM peak ($\Delta \simeq 10^{0.5}$) at $x \simeq +75\,{\rm kpc}\,h^{-1}$.

The CGM is responsible for both the absorption A_1 and emission E_1 features. The change from absorption to emission is caused by the change of sign in v_p. As $N_{\rm CII} \propto Z\Delta$, the maximum of the CGM signal is produced rightwards of the Δ maximum, i.e. at $x \simeq -5\,{\rm kpc}\,h^{-1}$. At this location $v_p < 0$, thus the CGM absorption feature (A_1) is stronger than the emission (E_1). The broader emission peak E_2 is caused by the IGM. Because of the lower density, this emission is an order of magnitude lower than the CGM absorption, and of the same order of the emission E_1.

The cumulative effect of the patch can be calculated by integration over the shown bandwidth of $\Delta\nu = 1$ GHz. This yields a net absorption, with intensity $\Delta I/I \simeq -7\times10^{-7}$. The order of magnitude of the cumulative effect is comparable with the amplitude of the fluctuations due to up-scattering of CMB photons with hot electrons ($T > 10^4$ K) produced by first stars/galaxies radiation, supernova feedback and structure formation shocks at redshifts $z > 10 - 20$ (e.g. Chluba, 2014).

---

[4] Note within our formalism the ISM does not contribute to τ_ν in eq. 4.4, since ISM emission is accounted via the V15 model (see Sec. 4.1.2).

[5] In the CMB terminology, *distortions* indicate spectral variations, while *anisotropies* refer to spatial variations. In this Chapter we study spectral distortions that are induced by a non-uniform distribution of metals. Throughout the Chapter, we refer to them as *fluctuations*.

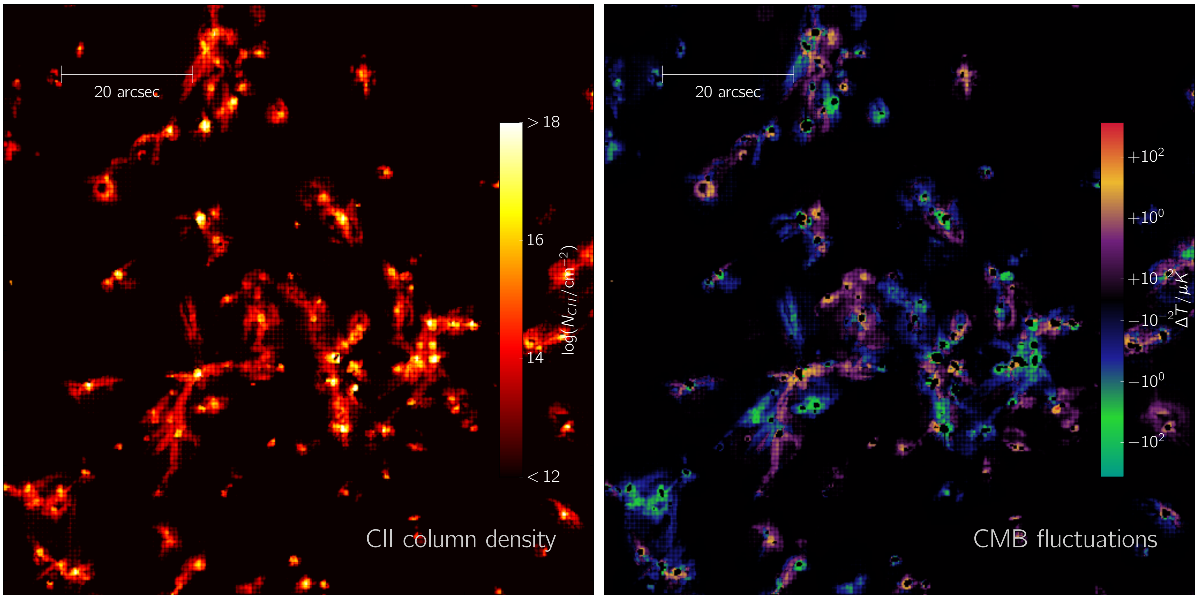

Figure 4.3: [C ii] column density map (left panel) and corresponding CMB fluctuations map (right panel) from a simulated field of view (FOV) of $\simeq (90'')^2$ at $z = 6$. **Left panel**: map of the [C ii] column density ($N_{\rm CII}$) responsible for the CMB fluctuations. The column density is shown for the range $12 < \log(N_{\rm CII}/{\rm cm}^2) < 18$ for displaying purposes. **Right panel:** the [C ii] CMB fluctuations map is shown as the brightness temperature $\Delta T \equiv \Delta I c^2/(2\nu^2 k_B)$ integrated on the simulation maximum available bandwidth, i.e. $\Delta\nu \simeq 2.6$ GHz. Note that the black spots inside the fluctuation patches ($|\Delta T| > 0$) are caused by the ISM masking. In both panels, the angular scale is indicated as an inset.

4.2 CMB fluctuations maps

We select a sample of $\simeq 4 \times 10^6$ l.o.s. extracted from a snapshot of the simulation at $z = 6$ to compute maps of CMB metal fluctuations. At this redshift, the simulation is characterized by a maximum field of view (FOV) of $\simeq (350'')^2$ and an adaptive spatial resolution up to $\simeq 500\,{\rm pc}$, implying that maps are resolved at angular scales of $\theta_{\rm res} \simeq 0.2''$.

Fig. 4.3 shows the [C ii] column density map (left panel) and the corresponding CMB fluctuation map (right panel) for a FOV $\simeq (90'')^2$. The [C ii] column densities are due to projection of the metal bubbles that originate around galaxies, pollute the IGM/CGM and extend in the cosmic web filaments. The density profiles around galaxies are self-similar once scaled with the virial radius of the parent dark matter halo (see Sec. 3.1.1), and metals usually extend out to $\simeq 10\, r_{\rm vir}$. Thus, extended patches with high $N_{\rm CII}$ values are found nearby older (more massive) galaxies, which have more time to increase the metallicity of the central CGM part and pollute the surrounding IGM environment. As a reference, the ISM typically has $\log(N_{\rm CII}/{\rm cm}^{-2}) \gtrsim 18$, the CGM (IGM) can be enriched up to $\log(N_{\rm CII}/{\rm cm}^{-2}) \gtrsim 16$ ($\log(N_{\rm CII}/{\rm cm}^{-2}) \gtrsim 12$).

In the right panel of Fig. 4.3, CMB fluctuations are expressed in terms of differential brightness temperature, $\Delta T \equiv \Delta I c^2/(2\nu^2 k_B)$, where ΔI is obtained by integrating ΔI_ν

(see eq. 4.3) on the total bandwidth of the simulation, i.e. $\Delta\nu \simeq 2.6$ GHz. The signal ranges from emissions up to $\Delta T \simeq +10^2 \mu$K down to absorptions of order $\Delta T \simeq -10^2 \mu$K. The signal is negligible ($|\Delta T| \lesssim 10^{-3} \mu$K) in $\simeq 60\%$ of the selected FOV, consistently with the analysis of the metal filling factor at this redshift (see Sec. 2.4.1, in particular Fig. 2.12).

The morphology of CMB fluctuations follows the $N_{\rm CII}$ distribution. The lack of an exact match between the respective maps is due to the dependence of ΔT from the peculiar velocity field. Absorption and emission features can arise from the differential velocity structure inside a single metal bubble. This is the spatial analogous of the emission/absorption features as a function of ν for the l.o.s. shown in Fig. 4.2.

Fluctuations are preferentially located in correspondence of $\log(N_{\rm CII}/{\rm cm}^{-2}) > 12$ patches, characterized by typical sizes $\theta \simeq 20''$; local maxima of the fluctuations ($|\Delta T| > 10^2 \mu$K) are usually found in smaller spots ($\theta \simeq 1''$) characterized by $\log(N_{\rm CII}/{\rm cm}^{-2}) \simeq 17$. This result is confirmed through the analysis of the CMB fluctuations power spectrum that peaks at angular scale $\theta \simeq 1''$, as detailed in App. D.

CMB fluctuations on large ($\simeq 10''$) and small ($\simeq 1''$) scales arise from the enriched IGM and CGM, respectively. Smaller scales correspond to the ISM of galaxies. These regions have been masked[6], since they do not contribute to CMB fluctuations, while possibly shining as [C II] emitters.

4.3 Mock observations

Starting from our model for [C II]-induced CMB fluctuations and [C II] emission from $z = 6$ galaxies, we generate mock observations specifically suited for comparison with ALMA data. The [C II] line at 157.74 μm from $z = 6$ is redshifted in ALMA BAND6 ($1.1 - 1.4$ mm). At this wavelengths the FOV (primary beam) of ALMA antennas is $\simeq 20''$, and the angular resolution (synthesized beam) ranges from $1.8''$ to $0.14''$, for the most compact and the most extended configuration, respectively (e.g. Maiolino, 2008)[7].

We account for ALMA angular resolution by convolving our maps with the synthesized beam, that can be characterized as a 2D-Gaussian. We assume a major axis of $1.4''$, a minor axis of $0.9''$, and a position angle of 91.6 deg. We choose this angular resolution setting because CMB fluctuations are expected to peak at $\simeq 1''$ (see Sec. 4.2 and App. D). Note that this resolution is sub-optimal for galaxy detection. A resolution of $\lesssim 0.5''$ would minimizes the surface-brightness bias for galaxy detection, thus maximizing the

---

[6] The ISM masking interests less than 0.5% of the total FOV.

[7] For further details, please refer to the ALMA handbook https://almascience.eso.org/documents-and-tools/cycle-0/alma-technical-handbook/at_download/file

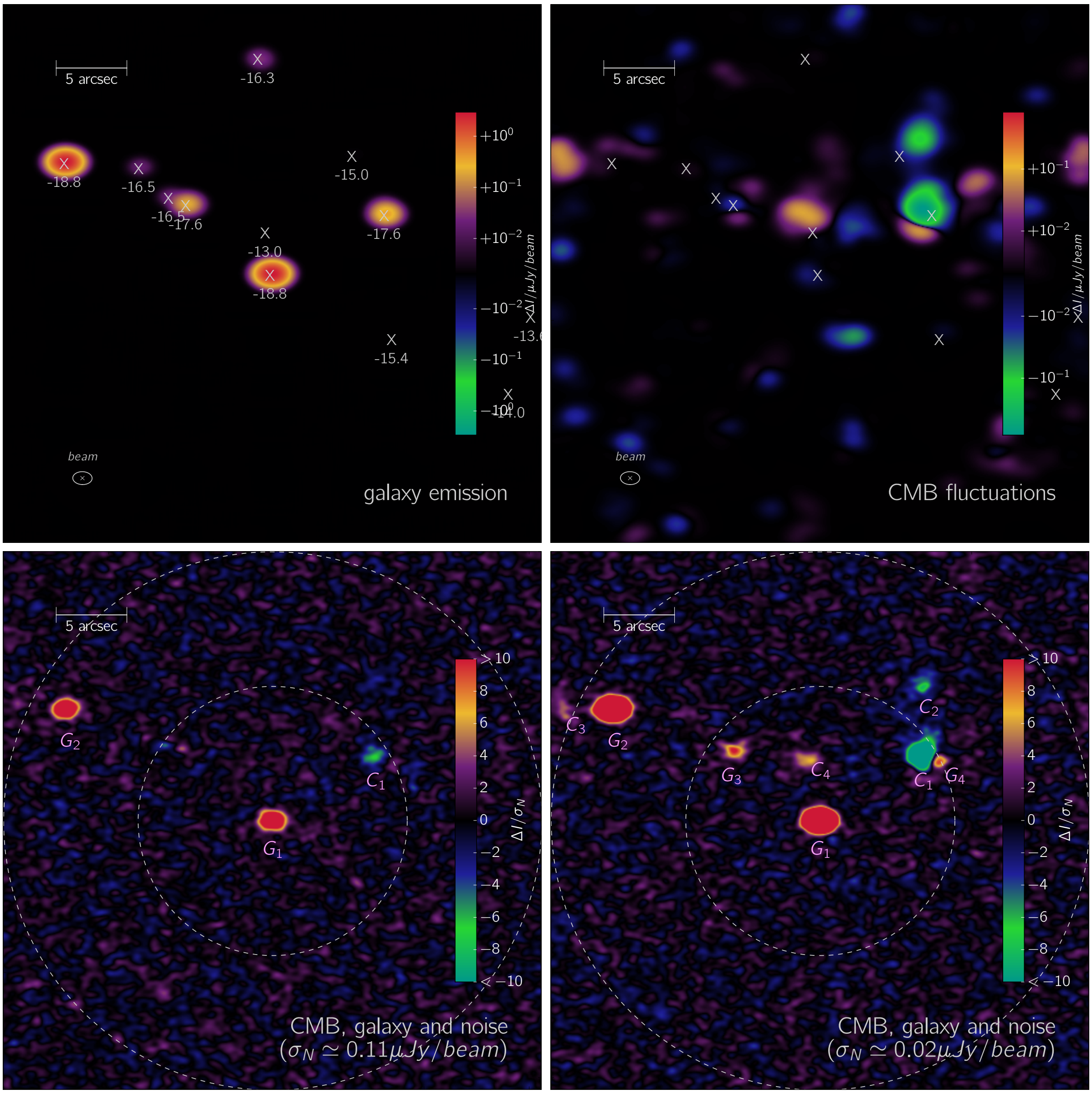

FIGURE 4.4: Mock ALMA [C II] continuum ($\Delta\nu = 8$ GHz) map observed with BAND6 with a synthesized beam of $\simeq (1'')^2$. The maps are shown for a total FOV of $(38.04 \simeq as)^2$, twice BAND6 primary beam. In each panel, the map, the angular scale and the synthesized beam are indicated as insets. In the upper panels we separately plot the contribution for galaxy emission and CMB fluctuations. In the lower panels two mock observations (galaxy emission and CMB fluctuations and noise) for two different noise levels are shown. **Upper left panel**: [C II] signal from galaxy emission. The positions of galaxies are indicated with an 'X' and labelled with the corresponding UV magnitude ($M_{\rm UV}$, details in the text). The intensity is expressed as μJy/beam and, to better appreciate the presence/absence of the signal, the intensity is in symmetric logarithmic scale. **Upper right panel**: [C II] signal from CMB fluctuations from the same field of view. As for emission from galactic ISM, the intensity scale is nonlinear. **Lower left panel**: mock observation, obtained by summing the contributions from CMB fluctuation, galaxy emission and noise. The noise distributions fit a Gaussian with r.m.s. $\sigma_N \simeq 0.11\mu$Jy/beam. To augment the readability of the map, the intensity is rescaled with σ_N and the scale is limited to $|\Delta I| < 10\,\sigma_N$. To help the description in the text, detections of CMB fluctuations and galaxy emission are indicated with C_i and G_i, respectively. For reference, we plot the ALMA primary beam and twice the primary beam with dashed lines. **Lower right panel**: as in the lower left panel but with $\sigma_N \simeq 0.02\mu$Jy/beam.

sample completeness (e.g. Grazian et al., 2011). This different setup is discussed in Sec. 4.4.

CMB fluctuations and galaxy emission maps are generated by integrating on $\Delta\nu = 8$ GHz, i.e. the maximum bandwidth available for continuum observations. This is done in order to maximize both the sensitivity and the possibility of finding CMB signal in the selected FOV. The simulation size limits the maximum available bandwidth to $\Delta\nu = 2.6$ GHz (see Sec. 4.2). We generate a longer light-cone by replicating the $z = 6$ simulation box. To avoid spurious periodicity effects, we randomize the simulation box by applying translations, rotations and reflections (e.g. Blaizot et al., 2005). Then, the signal from the light-cone is integrated over $\Delta\nu = 8$ GHz, by taking into account that ALMA continuum band is not contiguous, i.e. it is composed of two 4 GHz bands, separated by 10 GHz.

Finally, mock maps are combined with noise maps generated with ALMAOST (Heywood et al., 2011). Within the primary beam, the noise map has a Gaussian distribution with zero mean and r.m.s. σ_N; the r.m.s. accounts for instrumental uncertainties and atmospheric conditions. We assume 0.913 mm of water vapor for our fiducial observational setting. Using the ALMA full array, we have a continuum sensitivity of $\sigma_N \simeq 11.09\,(t/\mathrm{hr})^{-1/2}(\Delta\nu/8\ \mathrm{GHz})^{-1/2}[\,\mu\mathrm{Jy/beam}]$ for an observational time t at $\nu_{\rm obs} \simeq 271$ GHz.

In Fig. 4.4 we plot mock maps all centered on the same $M_{\rm UV} \simeq -19$ galaxy. In the upper panels, we plot separately the galaxy emission (left) and CMB fluctuations (right) signals, expressed in μJy/beam. The angular scale and the synthesized beam are indicated in the inset. In the galaxy emission map, the symbol ‘X’ indicates locations of galaxies, which are labelled according to their $M_{\rm UV}$. Galaxies are mostly found clustered in the upper region, and the plot shows a clear correlation between galaxy UV magnitude and [C II] emission (see the right panel of Fig. 4.1 in Sec. 4.1.2). In fact, brighter [C II] emitters ($\Delta I \simeq \mu$Jy/beam) correspond to brighter UV galaxies ($M_{\rm UV} \simeq -19$), characterized by a total [C II] flux of the order of $\Delta I \simeq 100\ \mu$Jy; dimmer galaxies ($M_{\rm UV} \simeq -16.5$) are identified through [C II] emission peaks of the order of $\Delta I \simeq 10^{-1}\mu$Jy/beam; the faintest galaxies in the map ($M_{\rm UV} \simeq -15$) show very low [C II] emission, $\Delta I \lesssim 10^{-2}\mu$Jy/beam.

The CMB fluctuations map (upper left panel of Fig. 4.4) shows various peaks both in absorption and emission. The signal due to CMB fluctuations result to be more extended and offset with respect to galaxy emission (indicated as ‘X’). This is expected from our analysis of $N_{\rm CII}$ and CMB fluctuations maps (see Fig. 4.3). Typically, emission/absorption features range between $10^{-2} \lesssim |\Delta I|/(\mu\mathrm{Jy/beam}) \lesssim 10^{-1}$, with local intensity maxima comparable to the emission signal of a $M_{UV} \simeq -17$ galaxy. The strongest peak occurs in absorption and it characterized by $\Delta I \lesssim -10^{-1}\mu$Jy/beam.

In the lower panels of Fig. 4.4, we plot the total signal, i.e. including the contribution from CMB fluctuations, galactic emission and two different noise levels: $\sigma_N \simeq 0.1\mu$Jy/beam (left) and $\sigma_N \simeq 0.02\mu$Jy/beam (right) that correspond to $t \simeq 1.3 \times 10^4$hr and $t \simeq 3.1 \times 10^5$hr observing time, respectively. In these panels, the intensity of the signal is rescaled to the noise r.m.s.; additionally, detections of CMB fluctuations and galaxy emission are indicated with C_i and G_i, respectively.

For $\sigma_N \simeq 0.11\mu$Jy/beam, the noise covers most of the CMB fluctuations and all the faint peaks of the galactic emission map ($M_{UV} \gtrsim -17$). Detectable signals arise from the two $M_{UV} \simeq -19$ galaxies (G_1 and G_2) and from the peak of the CMB fluctuations (C_1); the galaxies show $> 10\sigma_N$ emission peaks, and the fluctuation appears as a $\simeq 7\sigma_N$ absorption signal.

In the case of the deeper mock observation, for $\sigma_N \simeq 0.02$ μJy/beam, $M_{\rm UV} \simeq -17.6$ galaxies are detectable (G_3 and G_4) at $> 6\sigma_N$ as [C ii] emitters within the primary beam. Note that G_3 is a $> 10\sigma_N$ peak, while G_4 show an emission $\simeq 6\sigma_N$, as its signal is partially suppressed by the nearby absorption from CMB fluctuations at C_1. Three more CMB fluctuations peaks are visible on the map: a $\simeq 6\sigma_N$ absorption arising outside the primary beam (C_2), and two extended $\simeq 5\sigma_N$ emissions (C_3 and C_4) located within $2.5''$ from the $M_{UV} \simeq -19$ galaxies.

Note that CMB fluctuations in emission can be mistaken for signals arising from galaxies. In principle, the origin of the signal can be distinguished by analyzing its spectral properties. Typically, galaxy [C ii] emission lines have FWHMs $\gtrsim 50 - 100\,{\rm km\,s^{-1}}$ (e.g. Cormier et al., 2015, Decarli et al., 2014, Vallini et al., 2013), while CMB fluctuations usually show a double-peak structure in the spectra (see Sec. 4.1.3, in particular Fig. 4.2), with narrower lines (FWHM$\simeq 30 - 40\,{\rm km\,s^{-1}}$) both in absorption and emission.

A more robust discriminant for the nature of the signal can be provided by multi-wavelength analysis. By comparing the [C ii] map with UV imaging of the field, we can distinguish between the emission from CMB fluctuations and galaxies. Knowing the location and UV luminosity of galaxies in the field, we can infer the expected [C ii] flux (see Sec. 4.1.2, in particular right panel of Fig. 4.1). JWST will have a reference limiting magnitude of $M_{\rm UV} \simeq -16$ at $z = 6$, thus it seems to be perfectly suited for such comparison.

4.4 Observational prospects

The amplitude of [C ii]-induced CMB fluctuations is expected to be $|\Delta I| \lesssim 1\mu$Jy/beam, as discussed in the previous section. With the aim of defining the optimal observational strategy for detecting such weak signals, we first consider the feasibility of a blind survey

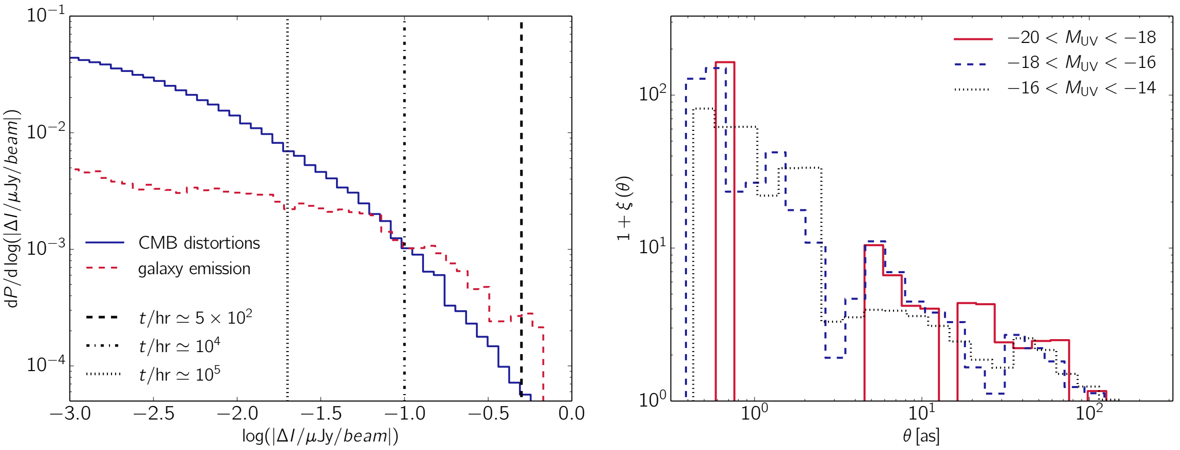

FIGURE 4.5: **Left panel**: PDFs of the absolute value of the signal from CMB fluctuations (blue solid line) and galaxy emission (red solid) are plotted. Both signals account for the assumed ALMA synthesized beam (see Sec. 4.3). The PDF integral is normalized to unity, and the plot is cut at $|\Delta I| = 10^{-3}\mu$Jy/beam for displaying purpose. As a reference, with vertical lines we plot several flux detection limits: the corresponding ALMA observational time is indicated in the legend. **Right panel**: Angular cross-correlation (ξ) function between high CMB fluctuation peaks ($|\Delta I| > 0.1\mu$Jy/beam, see text) and galaxies with limiting magnitude $M_{\rm UV} = -18,\ -16$ and -14 (plotted with red, blue and black lines, respectively).

experiment with ALMA. We compute the probability distribution functions (PDFs) of the intensity of [C II]-induced CMB fluctuations and [C II] galaxy emission at $z = 6$. We consider the signals extracted from the whole simulation FOV, $\simeq (350'')^2$, on the $\Delta\nu \simeq 2.6$ GHz bandwidth centered at the frequency $\nu_{\rm obs} \simeq 271$ GHz. The intensity of both signals accounts for the $\simeq (1'')^2$ ALMA synthesized beam introduced in Sec. 4.3. For each PDF, the corresponding integral is normalized to unity.

In the left panel of Fig. 4.5, we plot the PDFs for CMB fluctuations and galaxy emission with blue solid and red dashed lines, respectively. The plot is cut at $|\Delta I| = 10^{-3}\mu$Jy/beam for displaying purpose. As a reference, with vertical lines we plot 1-σ flux detection limits that correspond to the ALMA observing time indicated in the legend, calculated with the ALMA Sensitivity Calculator[8]. For the CMB fluctuations, the PDF rapidly decreases from $10^{-1.5}$ at $|\Delta I| \simeq 10^{-3}\mu$Jy/beam down to 10^{-4} at $|\Delta I| \simeq 10^{-0.5}\mu$Jy/beam. For the galaxy emission, the PDF decrease is less steep, and the two PDFs cross at $|\Delta I| \simeq 10^{-1}\mu$Jy/beam.

We indicate with $\sigma_{\rm N}$ the 1-σ flux detection limit of the ALMA blind survey. Then the integral of the PDF above $\sigma_{\rm N}$ provides the probability $P_{\rm dis}$ and $P_{\rm gal}$ of detecting CMB fluctuations and galaxy emission, respectively. For $\sigma_{\rm N} = 10^{-3}\mu$Jy/beam (corresponding to an ALMA observing time $t \simeq 10^6$hr), we find $P_{\rm dis} \simeq 4\%$ and $P_{\rm gal} \simeq 1\%$. Given the current telescope sensitivity, if we consider a more realistic – thought challenging –

---

[8] `https://almascience.eso.org/proposing/sensitivity-calculator`

observation, i.e. $\sigma_N = 10^{-1}\mu$Jy/beam ($t \simeq 10^4$hr), we find $P_{\rm gal} \simeq P_{\rm dis} \simeq 0.05\%$. This highlights that it is extremely difficult to detect CMB fluctuations with a blind survey.

Therefore, as an alternative strategy we consider the search for CMB fluctuations in the close proximity of high-z galaxies. We compute the cross-correlation (ξ) between CMB fluctuations peaks and UV galaxy emission. We calculate ξ by using an extension of the Hamilton estimator (e.g. Nollenberg & Williams, 2005):

$$\xi(\theta) + 1 = (D_G D_C \langle D_R D_R \rangle)/(\langle D_G D_R \rangle \langle D_C D_R \rangle)\,, \tag{4.5}$$

where $D_i D_j$ is the number of data pairs from sets i and j within angular distance θ, the subscripts G and C indicate the set of positions for galaxy and CMB fluctuations peaks respectively, and R labels a set of locations extracted from a random uniform distribution; the operator $\langle \dots \rangle$ indicates the average on different realizations of R. Both the dimension of the set R and the number of realizations for the average are fixed to reach a suitable convergence for ξ.

For what concerns CMB fluctuations, we consider only strong peaks, i.e. fluctuations with $|\Delta I| > 0.1\mu$Jy/beam. Within the simulated FOV we find $\simeq 30$ of such peaks, with signal intensity up to 0.25μJy/beam in emission and down to -0.82μJy/beam in absorption. For these signals, the mean $|\Delta I|$ is $\simeq 0.23\mu$Jy/beam and the r.m.s. is $\simeq 0.25\mu$Jy/beam. For what concerns galaxies, we select sets of galaxies, characterized by different UV limiting magnitudes.

In the right panel of Fig. 4.5, we plot with red, blue and black lines the cross-correlation calculated for galaxies with $M_{\rm UV} < -18$, -16 and -14, respectively. Although there is a clear cross-correlation between strong CMB fluctuations and galaxy emission, we find no strong dependence of the correlation scale from the considered $M_{\rm UV}$ limits[9]. Therefore, the most promising – though challenging – observational strategy for detecting [C II]-induced CMB fluctuations is to get a deep ($\sigma_N \lesssim 0.1\mu$Jy/beam) ALMA BAND6 observation pointing a $M_{\rm UV} \simeq -19$ known galaxy, e.g. in the HDF south, where the deepest photometry is available. This observational strategy is detailed in Sec. 4.3.

From Fig. 4.5 it appears that [C II] emission detection is very challenging even from the bright end galaxies in our simulation ($M_{\rm UV} \gtrsim -19$). As anticipated in Sec. 4.3, this is critically dependent on the assumed $\simeq 1''$ synthesized beam. A galaxy at $M_{\rm UV} \simeq -19$ has a [C II] emission of $\simeq 100\mu$Jy (see Fig. 4.1 and eq. 4.2). This correspond to a flux of

---

[9] The cross-correlation scale does not strongly depend on the considered $M_{\rm UV}$ limits because of the following. Brighter (more massive) galaxies are expected to be surrounded by more extended and enriched CGM. However CMB fluctuations linearly depend on the velocity field, thus there is a lack of correspondence between high $N_{\rm CII}$ values and strong fluctuations (see Sec 4.2 for details, in particular Fig. 4.3).

$\simeq 1\mu$Jy/beam in the ALMA map with a $\simeq 1''$ synthesized beam. Hence, with this set-up, $\simeq 10^3$ hours of integration time are required in order to detect the signal at $\simeq 4\sigma$.

The detectability drastically improves when using instead a synthesized beam similar to the galaxy size i.e. $\simeq 0.5''$, like the one used in recent high-z observations (Capak et al., 2015, Maiolino et al., 2015, Willott et al., 2015). With this set-up, we find that a $M_{\rm UV} = -18, -19, -20$ galaxy can be detected at 4σ in $\simeq 2000, 40, 1$ hours, respectively. Indeed, [C II] has been detected in high-z galaxies with magnitudes up to $M_{\rm UV} > -20$ with $t \sim 1$hr (Maiolino et al., 2015, Willott et al., 2015). With a more demanding observational time of ~ 40hr, we would be able to detect $M_{\rm UV} \simeq -19$ galaxies at $z \simeq 6$, thus sampling galaxies more similar to the true reionization sources.

4.5 Summary

In this Chapter we have studied the possibility of mapping heavy elements via far infrared (FIR) emission from the interstellar medium (ISM) of high-z galaxies and cosmic microwave background (CMB) fluctuations induced by metals in the circumgalactic and intergalactic medium. We focus on high-z low mass ($M_\star \lesssim 10^{10}{\rm M}_\odot$) galaxies, which are expected to be abundant (at $z \sim 6$) and to represent the first ($z \gtrsim 10$) efficient metal polluters of the IGM (e.g. Ferrara, 2008, Madau et al., 2001) and sources of reionization (e.g. Barkana & Loeb, 2001).

Among the FIR emission lines, the [C II] $\left(^2P_{3/2} \rightarrow {}^2P_{1/2}\right)$ transition at 157.74 μm is the brightest (e.g. Crawford et al., 1985, Madden et al., 1997), and it is used to trace and characterize $z \sim 6$ galaxies (e.g. Carilli & Walter, 2013). We compute both the [C II] emission arising from the interstellar medium (ISM) of $z = 6$ galaxies and the amplitude of [C II]-induced[10] CMB fluctuations from metals in the IGM and circumgalactic medium (CGM).

We use state-of-the-art high-z hydrodynamical simulations (see Chapter 2) that follow the evolution of the cosmic metal enrichment from $z = 10$ from $z = 4$. We calculate the galactic [C II] signal by using a ISM model (Vallini et al., 2013, 2015) that accounts for the detailed sub-kpc scales structure of the emission, namely for the cold and warm neutral medium and in high density photodissociation regions (PDRs). We calculate the CMB fluctuations induced by C II ions by modelling the resonant scattering between the CMB and metals in the IGM/CGM (e.g. Basu et al., 2004, Maoli et al., 1996) and we predict the related emission and absorption features arising in the FIR band.

---

[10] The presented method can be straightforwardly extended to other FIR lines, as [N II] at 122 μm, [O III] at 88 μm, [Si I] at 129 μm and [O I] at 63 μm.

We then carefully analyze the theoretical signal of CMB fluctuations from the IGM/CGM. While the effects of resonant scattering of CMB photons by very early metals ($z \gg 10$) were studied with analytical models and simple assumptions about the metal distribution (e.g. Basu et al., 2004, Schleicher et al., 2008), the present study is the first based on hydrodynamical numerical simulations extending to observable epochs ($z \sim 6$). In terms of the differential brightness temperature, $\Delta T \equiv \Delta I c^2/(2\nu^2 k_B)$, we calculate the signal from $z = 6$ integrating on the simulation available bandwidth, $\Delta\nu = 2.6$ GHz. We find that the metal-induced fluctuation signal is in the range $\Delta T \simeq \pm 10^2 \mu$K, i.e. can be seen either in emission or absorption. The peak of the signal is found on scales of $\theta \simeq 1''$, in correspondence of CGM absorption systems characterized by C II column density of $\log(N_{\rm CII}/{\rm cm}^{-2}) \simeq 16$.

To test the detectability of the [C II] signal, we have constructed and analyzed mock observations specifically suited for comparison with ALMA BAND6 data.

We predict that [C II] emission is correlated with $M_{\rm UV}$. At $M_{\rm UV} < -20$, the faintest high-z galaxy from which [C II] emission is detected, our relation (eq. 4.2) is in good agreement with recent observations (Capak et al., 2015, Maiolino et al., 2015, Willott et al., 2015). We find that a $M_{\rm UV} = -18, -19, -20$ galaxy can be detected at 4σ in $\simeq 2000, 40, 1$ hours, respectively. Indeed, [C II] has been detected in high-z galaxies with magnitudes up to $M_{\rm UV} > -20$ with $t \sim 1$hr (Maiolino et al., 2015, Willott et al., 2015). With a more demanding observational time of ~ 40hr at $z \simeq 6$ we would be able to detect $M_{\rm UV} \simeq -19$ galaxies, thus sampling galaxies more similar to the true reionization sources. Additionally, the relation is the analogous of the local ($z = 0$) $L_{\rm CII}$-SFR relation (De Looze et al., 2014). Eq. 4.2 highlights the possibility of using [C II] as a tracer of star formation activity, that can be used independently from UV flux determination. This is particularly important at high-z as, contrary to UV light, [C II] emission is not affected by dust extinction.

FIR observations allow in principle to simultaneously detect galaxies and to map their surrounding CGM through [C II] induced CMB fluctuations. The detection of this signal would be a breakthrough for our understanding of the early phases of galaxy formation and cosmic enrichment processes. The CGM is the interface regulating the outflows of enriched material from the galaxy and the inflows of pristine gas from the IGM; it has been probed so far up to $z \sim 2$ with absorption line experiments towards background sources, typically QSO (e.g. Churchill et al., 2013, Liang & Chen, 2014, Steidel et al., 2010). The intervening CGM associated with a foreground galaxy leaves an absorption feature in QSO spectra. With a large number of galaxy-absorber pairs, it is then possible to statistically determine the equivalent width of a given absorption line as a function of the line of sight impact parameter. Detecting CMB fluctuations is equivalent to actually map the bidimensional distribution of metals in the CGM, and it would allow to extend the enrichment study at higher redshift.

We have compared the efficiency of different observational strategies for detecting [C II] induced CMB fluctuations. We find that this signal is very faint, e.g. $|\Delta I| \simeq 10^{-1}\mu$Jy/beam. Because of the signal amplitude and the [C II] emission filling factor, we find that a blind experiment yields a low probability for the signal detection. However, strong (i.e. $|\Delta I| \gtrsim 10^{-1}\mu$Jy/beam) CMB fluctuations are seen in our maps, that are characterized by a mean $|\Delta I|$ of $\simeq 0.23\mu$Jy/beam a r.m.s. of $\simeq 0.25\mu$Jy/beam and maximum $|\Delta I|$ up to 0.82μJy/beam. On average, these fluctuations have signals comparable to the typical [C II] emission from a $M_{\rm UV} \simeq -18$ galaxy. Our analysis highlights that strong CMB fluctuations are found typically within $\sim 10''$ of galaxies, regardless of their $M_{\rm UV}$.

We have also considered an alternative observational strategy to detect (strong) CMB fluctuations that consists of a deep ALMA pointing in a field where known $M_{\rm UV} \simeq -19$ galaxies (e.g. in the HDF south) are present. Our model predicts that, for an ALMA sensitivity of $\sigma_N = 0.1\mu$Jy/beam CMB fluctuations would be detected at a confidence level $\sigma > 3,\ 7$ with a probability $\simeq 25\%,\ 5\%$, respectively, while for $\sigma_N = 0.05\mu$Jy/beam we expect a detection of CMB fluctuations with c.l. $\sigma > 3,\ 5,\ 7$ with a probability $\simeq 70\%,\ 30\%,\ 15\%$, respectively. We note that the sensitivity requested for detecting [C II] induced CMB fluctuations ($\sigma_N \lesssim 0.1\mu$Jy/beam) corresponds to extremely long ALMA observing times ($t \gtrsim 10^4$hr), making the detection of this signal extremely challenging with current facilities.

However, by stacking deep ALMA observations ($\nu_{\rm obs} \sim 272$ GHz) of several $M_{\rm UV} \simeq -19$ (lensed) galaxies it may be possible to "statistically" detect such elusive CMB fluctuations induced by C II ions at $z \sim 6$. The same experiment, repeated at different frequencies ($\nu_{\rm obs} \sim 1900/(1+z)$ GHz) would allow to track the metal enrichment history through cosmic times. We defer this further statistical analysis to a future study.

CHAPTER 5

THE BRIGHTEST LYα EMITTER: POP III OR BLACK HOLE?

The end of the Dark Ages is marked by the appearance of the first stars. Such – Pop III – stars had to form out of a pristine composition (H+He) gas with virtually no heavy elements. Lacking these cooling agents, the collapse had to rely on the inefficient radiative losses provided by H_2 molecules. Mini-halos, i.e. nonlinear dark matter (DM) structures with mass $M_h \sim 10^{6-7} \mathrm{M}_\odot$ collapsing at high redshift ($z \sim 30$), are now thought to be the preferred sites of first star formation episodes (Greif et al., 2012, Salvadori & Ferrara, 2009, Turk et al., 2009, Visbal et al., 2015, Yoshida et al., 2006). Although the Initial Mass Function (IMF) of Pop III stars is largely uncertain, physical arguments suggest that they could have been more massive than present-day (Pop II) stars. Furthermore, the metals produced by Pop III stars polluted the surrounding gas (Bromm et al., 2002, Wise et al., 2012, Xu et al., 2013), inducing a transition to the Pop II star formation mode ("chemical feedback", Schneider et al. 2002, 2006). Metal enrichment is far from being homogeneous, and pockets of pristine gas sustaining Pop III star formation can in principle persist down to $z \simeq 3-4$ (Ma et al., 2015, Maio et al., 2010, Salvadori et al., 2014, Tornatore et al., 2007, Trenti et al., 2009, , see Sec. 2.2 in particular Fig. 2.1), yielding Pop III star formation rate (SFR) densities of $\sim 10^{-4} \mathrm{M}_\odot \mathrm{yr}^{-1} \mathrm{Mpc}^{-3}$, i.e. $\lesssim 1\%$ of the Pop II SFR density at those redshifts.

The search effort for Pop III stars at moderate and high redshifts has become increasingly intense in the last few years (e.g. Heap et al., 2015, Kashikawa et al., 2012). Observationally, a galaxy hosting a recent ($t_\star \lesssim 2\,\mathrm{Myr}$) Pop III star formation episode should show strong Lyα and He II lines and no metal lines (e.g. Kehrig et al., 2015, Raiter et al., 2010, Schaerer, 2002). Until now, no indisputable evidence for Pop III stars in distant galaxies has been obtained, and observations have only yielded upper bounds on Pop

III SFR (e.g. Cai et al., 2011, Cassata et al., 2013, Zabl et al., 2015). This situation might dramatically change following the recent observations of CR7 by Sobral et al. (2015, S15 hereafter).

CR7 is the brightest Lyα emitter (LAE) at $z > 6$, and it is found in the COSMOS field (Matthee et al., 2015). Spectroscopic follow-up by S15 suggests that CR7 might host a PopIII-like stellar population. This is based on the astonishingly bright Lyα and He II lines ($L_\alpha \simeq 10^{43.93}\mathrm{erg\,s^{-1}}$, $L_{\rm HeII} \simeq 10^{43.29}\mathrm{erg\,s^{-1}}$) and no detection of metal lines. S15 shows that CR7 can be described by a composite of a PopIII-like and a more normal stellar population, which would have to be physically separated, and that would be consistent with e.g. Tornatore et al. (2007). HST imaging shows that CR7 is indeed composed of different components: 3 separate sub-systems (A, B, C) with projected separations of $\lesssim$ 5kpc. F110W(YJ) and F160W(H) band photometry indicates that clump A might be composed of young (blue) stars, while the stellar populations of B+C are old and relatively red. The observed Lyα and He II lines are narrow (FWHM $\lesssim 200\,\mathrm{km\,s^{-1}}$ and FWHM $\lesssim 130\,\mathrm{km\,s^{-1}}$, respectively), disfavoring the presence of an AGN or Wolf-Rayet (WR) stars, which are expected to produce much broader (FWHM $\gtrsim 10^3\mathrm{km\,s^{-1}}$) lines (e.g. Brinchmann et al., 2008, De Breuck et al., 2000, Erb et al., 2010). S15 concluded that CR7 likely contains a *composite* stellar population, with clump A being powered by a recent Pop III-like burst ($t_\star \lesssim 2\,\mathrm{Myr}$), and clumps B+C containing an old ($t_\star \sim 350\,\mathrm{Myr}$) burst of Pop II stars with $M_\star \simeq 10^{10}\mathrm{M}_\odot$, largely dominating the stellar mass of the entire system.

Based on cosmological simulations that follows the simultaneous evolution of Pop II and Pop III stars (see Chapter 2), we examine the interpretation of CR7 as a Pop III host system and explore its implications. We also propose an alternate explanation, briefly discussed in S15, where CR7 is powered by accretion onto a Direct Collapse Black Hole and suggest further tests.

5.1 Simulation overview

We use the ΛCDM cosmological hydrodynamical simulations presented in Chapter 2, obtained with a customized version of the Adaptive Mesh Refinement code RAMSES (Teyssier, 2002) to evolve a $(10h^{-1}\ \mathrm{Mpc})^3$ volume from $z = 99$ to $z = 4$, with a DM mass resolution of $\simeq 5 \times 10^5\,h^{-1}\mathrm{M}_\odot$, and an adaptive baryon spatial resolution ranging from $\simeq 20\,h^{-1}$ kpc to $\simeq 1\,h^{-1}$ kpc.

Star formation is included via sub-grid prescriptions based on a local density threshold. If the star forming cell gas has metallicity below (above) the critical metallicity, $\mathrm{Z_{crit}} \equiv 10^{-4}\mathrm{Z}_\odot$, we label the newly formed stars as Pop III (Pop II). Supernova feedback accounts for metal-dependent stellar yields and return fractions appropriate for the relevant stellar population[1].

The simulated galaxy sample reproduces the observed cosmic SFR (Bouwens et al., 2012, Zheng et al., 2012) and stellar mass density (González et al., 2011) evolution in the redshift range $4 \leq z \lesssim 10$, and – as shown in Sec. 4.1.2, in particular Fig. 4.1 – we reproduce the observed the luminosity function at $z = 6$. Additionally, the derived Pop III cosmic SFR density is consistent with current observational upper limits (e.g. Cai et al., 2011, Cassata et al., 2013, Nagao et al., 2008). To allow a direct comparison with CR7 we will concentrate on the analysis of the $z \simeq 6$ simulation output.

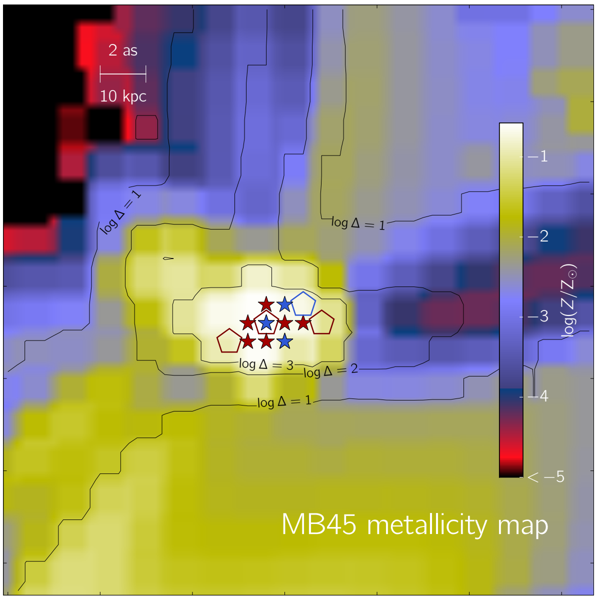

FIGURE 5.1: Metallicity (Z) map centered on the simulated galaxy MB45. Pop II locations are marked with filled stars, for recent (blue, $t_\star \lesssim 2$ Myr) and old (red) formation events, respectively. Locations of the recent (old) Pop III burst are shown by the open blue (red) pentagons. Overdensity ($\log \Delta = 1, 2, \text{and } 3$) contours are plotted with black lines. The scale is indicated in arcsecond and kpc.

5.1.1 Pop III-hosting galaxies

As noted in S15, the interpretation of CR7 fits in the “Pop III wave” scenario suggested by Tornatore et al. (2007). As an example of Pop III wave in action, we show the case of “MB45”, a simulated galaxy with total stellar mass $M_\star = 10^{7.9} \mathrm{M}_\odot$. In Fig. 5.1, we plot the metallicity (Z) and overdensity (Δ) map around MB45. The star formation history in MB45 starts with a Pop III event. These stars explode as supernovae enriching with metals the central regions of MB45. As a result, star formation there continues in the Pop II mode, while in the less dense external regions, not yet reached by the metal-bearing shocks, Pop III stars can still form. The process repeats until the unpolluted regions have densities exceedingly low to sustain star formation.

The total (i.e. old+young stars) Pop III mass in MB45 is $M_3 \simeq 10^{6.8} \mathrm{M}_\odot$; about 20% of this stellar mass formed in a recent burst (age $t_\star \lesssim 2$ Myr). The total stellar

---

[1] While in Sec. 2.5 we explore different types of IMF for Pop III, here we show results assuming a Pop II-like Salpeter IMF. It is to note that our simulations suggests that the Pop III SFR seems almost independent from the IMF (see in particular Fig. 2.14).

mass ($M_\star \simeq 10^8 M_\odot$) of MB45 is dominated by Pop II stars produced at a rate $\mathrm{SFR}_2 \simeq 0.5\,\mathrm{M}_\odot\,\mathrm{yr}^{-1}$. Thus, while MB45 formation activity proceeds in the Pop III wave mode and resembles that of CR7, the physical properties of MB45 and CR7 are different, because of the 2 orders of magnitude difference in total stellar mass. A direct comparison between the PopIII-PopII separation in CR7 (projected $\simeq 5\,$kpc) and MB45 (10 kpc, projected $\lesssim 5\,$kpc), although fairly consistent, might not be very meaningful due to the different mass of the two systems. This is because the separation depends on the mass-dependent metallicity profile in galaxy groups (see Sec. 3.1.1, in particular Fig. 3.1). However, we note that our current simulated volume is simply to small to be able to directly recover sources such as CR7, with volume densities of $\sim 10^{-6}\,\mathrm{Mpc}^{-3}$.

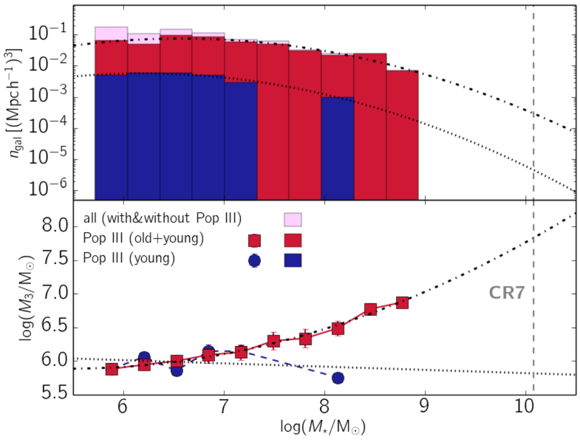

Figure 5.2: **Upper panel**: Number density (n_{gal}) of simulated galaxies as a function of their total stellar mass ($M_\star = M_2 + M_3$) for: (i) all galaxies (pink bar), (ii) galaxies with old+young Pop III stars (red bars), (iii) galaxies with a young Pop III component (blue bars). All quantities are averaged on $\log(\Delta M/\mathrm{M}_\odot) \simeq 0.3$ bins. Black dot-dashed and dotted lines correspond to the best-fit analytical extrapolation of n_{gal}. **Lower panel**: Mass of Pop III (M_3) in composite galaxies considering young (blue circle) and old+young (red squares) stars. In both panels the vertical dashed line indicates the value of $M_\star$ for CR7 as inferred by SED fitting (see Sec. 5.1.2).

The simulated volume contains many galaxies hosting Pop III star formation, whose number density (n_{gal}) as a function of their total stellar mass ($M_\star$) is shown in Fig. 5.2, along with their Pop III mass (M_3). Pop III stars are found preferentially in low-mass systems $M_\star \lesssim 10^{6.5}\mathrm{M}_\odot$, that typically form these stars in a series of a few $M_3 \simeq 10^6\mathrm{M}_\odot$ bursts[2], before Pop III formation is quenched by chemical feedback.

Note that all larger galaxies, $M_\star \gtrsim 10^7\mathrm{M}_\odot$, contain some Pop III component inherited from progenitor halos. We can then regard M_3 calculated by summing old and young Pop III stars as a solid upper bound to the total Pop III mass produced during the galaxy lifetime. The size of the simulation volume, dictated by the need of resolving the very first star-forming halos, is too small to fairly sample the mass function of galaxies with $M_\star \gtrsim 10^9\mathrm{M}_\odot$ and more massive. To make predictions in this high-mass range, we slightly extrapolate the simulated trends of n_{gal} and M_3 (lines in Fig. 5.2). We caution that such extrapolation might imply uncertainties.

---

[2] We refer to App. A for possible resolution effects.

5.1.2 Lyα and He II emission

We label as *pure* (*composite*) galaxies whose emission is produced by Pop II only (Pop II+Pop III) stars. For a pure galaxy, the Lyα line luminosity is (e.g. Dayal et al., 2008):

$$L_\alpha^{\rm pure} = 2.8 \times 10^{42} A_\alpha \, {\rm SFR}_2 \; {\rm erg\, s^{-1}} \,, \tag{5.1a}$$

where A_α is an attenuation factor that accounts for both internal (interstellar medium) absorption and intergalactic medium transmissivity; Pop II SFR is expressed in $\rm M_\odot yr^{-1}$ and to relate this to the $M_\star$ we assume ${\rm SFR}_2/M_\star = {\rm sSFR} \simeq 2.5\,{\rm Gyr}^{-1}$, consistent with our simulations and observations (Daddi et al., 2007, González et al., 2011, McLure et al., 2011, see Sec. 5.2).

Pure galaxies have no He II emission. For a composite galaxy, the Lyα emission is the sum of the contributions from Pop II and Pop III components:

$$L_\alpha^{\rm comp} = L_\alpha^{\rm pure} + A_\alpha l_3^\alpha M_3 \,, \tag{5.1b}$$

where l_3^α is the Pop III Lyα line luminosity per unit stellar mass[3]. Analogously, the He II emission is given by

$$L_{\rm HeII} = l_3^{\rm HeII} M_3 \,, \tag{5.1c}$$

where $l_3^{\rm HeII}$ is the Pop III He II luminosity per unit stellar mass. Both l_3^α and $l_3^{\rm HeII}$ depend on the IMF and burst age, $t_\star$. We adopt the Pop III models by Schaerer (2002) and Raiter et al. (2010), and we use a Salpeter IMF (power-law slope $\alpha = -2.35$), with variable lower (m_{low}) and upper (m_{up}) limits. As long as $m_{up} \gtrsim 10^2 \rm M_\odot$, the results are very weakly dependent on the upper limit, which we therefore fix to $m_{up} = 10^3 \rm M_\odot$, leaving m_{low} as the only free-parameter.

As noted by S15, to reproduce CR7 L_α and $L_{\rm HeII}$ with Pop IIIs, a mass of $M_3 \simeq 10^{7-9} \rm M_\odot$ *newly-born* ($t_\star \lesssim 2-5$ Myr) stars is required, depending on the IMF. Such a large amount of *young* Pop III stars is contained in none of the simulated galaxies and it is not predicted by the adopted analytical extrapolation (see Fig. 5.2). Thus none of the simulated composite galaxies would reproduce CR7 line emission. However, it is possible that CR7 might have experienced a more vigorous Pop III star formation burst as a result of a very rare event – e.g. a recent major merger – not frequent enough to be captured in our limited box volume. As an estimate we adopt the value of M_3 resulting from the sum of all (old+young) Pop III stars formed in our galaxies.

---

[3] We are implicitly assuming that Pop III stars form in a burst, an assumption justified by the analysis presented in Sec. 5.1.1.

Under this hypothesis, we can fix m_{low}, by using the zero age main sequence (ZAMS) tracks ($t_\star = 0$). By SED fitting, S15 shows that CR7 Pop II stellar mass (completely contained in clumps B+C) is likely $M_\star \simeq M_2 \simeq 10^{10}\mathrm{M}_\odot$. From the lower panel of Fig. 5.2, we find that this mass corresponds to a Pop III mass of $M_3 \sim 10^{7.5}\mathrm{M}_\odot$. From Pop III SED fits of region A S15 estimate $M_3 \sim 10^{7}\mathrm{M}_\odot$. As these stars must be located in CR7 clump A, whose He II luminosity is $L_{\mathrm{HeII}} = 10^{43.3}\mathrm{erg\,s^{-1}}$, eq. 5.1c requires that $l_3^{\mathrm{HeII}} = 10^{35.5}\mathrm{erg\,s^{-1}\,M_\odot^{-1}}$. In turn this entails a top-heavy IMF with $m_{low} = 6.7\,\mathrm{M}_\odot$.

Having fixed the IMF, we can readily derive the predicted Pop III contribution to the Lyα emission; this turns out to be $l_3^{\alpha} = 10^{36.7}\mathrm{erg\,s^{-1}\,M_\odot^{-1}}$. CR7 has an observed $L_\alpha = 10^{43.9}\mathrm{erg\,s^{-1}}$, with no contribution from clumps B+C ($\mathrm{SFR}_2 = 0$). This comparison allows us to determine, using eq. 5.1b, the Lyα line attenuation factor, $A_\alpha = 10^{-0.57}$.

Roughly 66% of the line luminosity is therefore damped, a figure consistent with other derivations (e.g. Dayal et al., 2008), and with the analysis of S15. The above procedure provides a basis to model Lyα and He II emission for both pure and composite galaxies, assuming that the properties of the Pop III component are similar to those derived from CR7.

5.2 Predictions for bright LAEs

Starting from the assumption that CR7 is a “typical” composite galaxy, and using $m_{low} = 6.7\,\mathrm{M}_\odot$ and $A_\alpha = 10^{-0.57}$, we can now predict how many LAEs among those observed by Matthee et al. (2015) are composite galaxies, i.e. contain Pop III stars. The number of LAEs in the COSMOS/UDS/SA22 fields with luminosity L_α is $N_\alpha = \Phi_\alpha(L_\alpha)\,V_{obs}$, where Φ_α is the observed Lyα luminosity function and $V_{obs} = 4.26 \times 10^6\,\mathrm{Mpc}^3$ is the observed volume. Among these, a fraction

$$f_\alpha^{\mathrm{comp}} = N_{\mathrm{comp}}/(N_{\mathrm{comp}} + N_{\mathrm{pure}}) \tag{5.2a}$$

contain Pop III stars, where N_{comp} (N_{pure}) is the number of composite (pure) galaxies in V_{obs} at a given L_α.

Eq.s 5.1a and 5.1b, show that a given L_α can be produced by a composite galaxy with a lower $M_\star$ with respect to a pure (PopII) galaxy. For instance, $L_\alpha \simeq 10^{43.5}\mathrm{erg\,s^{-1}}$ requires $M_\star \simeq 10^{10.5}\mathrm{M}_\odot$ for a pure galaxy, but only $M_\star \lesssim 10^{9.5}\mathrm{M}_\odot$ for a composite one. Such large objects are very rare at the redshift of CR7 ($z = 6.6$) and in the observed volume[4]. Therefore, it is important to account for the statistical (Poisson) fluctuations

---

[4] As a reference, a $M_\star \sim 10^{10.5}\mathrm{M}_\odot$ is hosted in a DM halo of mass $M_h \sim 10^{12.5}\mathrm{M}_\odot$, whose abundance is $n_h \sim 10^{-6}\mathrm{Mpc}^{-3}$ at $z \simeq 6$ (e.g. Sheth & Tormen, 1999).

of the galaxy number counts as follows:

$$N_\kappa = n_\kappa V_{obs}(1 \pm (n_\kappa V_{obs})^{-1/2}) \,, \tag{5.2b}$$

where $\kappa =$ (composite, pure). The distribution of $n_{\rm comp}(M_\star)$ is shown in the upper panel of Fig. 5.2 as the "young" Pop III curve[5]; while $n_{\rm pure}$ accounts for the remaining galaxies. The effect of the finite volume effects on $f_\alpha^{\rm comp}$ can be appreciated from the lower panel of Fig. 5.3. Assuming a higher sSFR $= 5\,{\rm Gyr}^{-1}$ (e.g. Stark et al., 2013) yields the modifications shown by the dash-dotted line.

In the upper panel of Fig. 5.3 we plot the LAE number (N_α) as a function of L_α. Matthee et al. (2015) observations (green pentagons) are shown along with our predictions for the composite LAE and expected $L_{\rm HeII}$ emission. CR7 is the most luminous LAE observed, and it is in the brightest luminosity bin ($L_\alpha = 10^{44\pm0.1}{\rm erg\,s^{-1}}$); by assumption CR7 is a composite galaxy. If so, we then predict that out of the 46 (30) LAEs with $L_\alpha = 10^{43.2\pm0.1}{\rm erg\,s^{-1}}$ ($> 10^{43.3}{\rm erg\,s^{-1}}$, cumulative), 13 (14) must also be composite galaxies[6], with observable $L_{\rm HeII} \simeq 10^{42.5}{\rm erg\,s^{-1}}$ ($\gtrsim 10^{42.7}{\rm erg\,s^{-1}}$). Follow-up spectroscopy of those luminous Lyman-α emitters at $z = 6.6$ will allow to test this prediction. We recall that this test assumes that all Pop III give raise to the same Lyα and He II emission as inferred from CR7, that requires that all the Pop III stellar mass was formed in a single burst with age $\lesssim 2$ Myr.

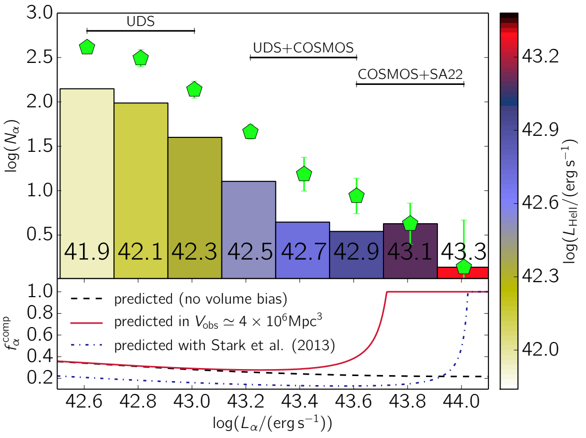

FIGURE 5.3: **Upper panel**: Number of LAEs (N_α) as a function of their Lyα luminosity (L_α) in the COSMOS/UDS/SA22 fields (Matthee et al., 2015, green pentagons). The histogram shows the predicted number of composite (i.e. Pop III hosts) LAEs in the same survey; the bar colors indicate the expected $L_{\rm HeII}$ emission, also shown by the numbers in the bars. **Lower panel**: Fraction of composite galaxies ($f_\alpha^{\rm comp}$, eq. 5.2a) for which the correction for the finite volume bias (eq. 5.2b) of Matthee et al. (2015) survey has been included (red solid) or neglected (black dashed).

Particularly in the regime where $f_{\rm comp} < 1$ (see lower panel in Fig. 5.3), a sample of LAEs is needed to test our model predictions. For example for "Himiko", the

---

[5] As noted in Sec. 5.1.1, all galaxies with $M_\star > 10^7$ have old Pop III stars, thus considering the "old+young" track for $n_{\rm comp}$ would yield an unrealistically high composite number.

[6] The predicted number would become 7 (7), by assuming sSFR from Stark et al. (2013).

second most luminous[7] confirmed LAE at $z = 6.6$ with $L_\alpha \simeq 10^{43.4}\mathrm{erg\,s^{-1}}$ (Ouchi et al., 2009), for which recent VLT/X-Shooter observations have provided a 3σ limit of $L_{\mathrm{HeII}} \lesssim 10^{42.1}\mathrm{erg\,s^{-1}}$ (Zabl et al., 2015), our model predicts $L_{\mathrm{HeII}} \simeq 10^{42.7}\mathrm{erg\,s^{-1}}$ i.e. a four times higher He II luminosity. However, this is predicted only for $f_{\mathrm{comp}} \simeq 20-30\%$ of galaxies at this L_α.

5.3 Alternative interpretation

Given the extreme conditions required to explain the observed properties of CR7 in terms of Pop III stars and a set of assumptions, it is worth exploring alternative interpretations. The most appealing one involves Direct Collapse Black Holes (DCBH), which is briefly discussed in S15. High-z pristine, atomic halos ($M_h \gtrsim 10^8\mathrm{M_\odot}$) primarily cool via Ly$\alpha$ line emission. In the presence of an intense Lyman-Werner (LW, $E_\gamma = 11.2-13.6\,\mathrm{eV}$) irradiation, H_2 molecule photo-dissociation enforces an isothermal collapse (Agarwal et al., 2013, Latif et al., 2013, Shang et al., 2010, Yue et al., 2014), finally leading to the formation of a DCBH of initial mass $M_\bullet \simeq 10^{4.5-5.5}\mathrm{M_\odot}$ (Begelman et al., 2006, Ferrara et al., 2014, Volonteri et al., 2008), eventually growing up to $10^{6-7}\mathrm{M_\odot}$ by accretion of the halo leftover gas.

In CR7, clump A appears to be pristine, and it is irradiated by a LW flux from B+C[8] of $\sim 5\times10^{-18}\mathrm{erg\,s^{-1}\,cm^{-2}Hz^{-1}\,sr^{-1}}$, well in excess of the required threshold for DCBH formation (Latif et al., 2013, Regan et al., 2014, Shang et al., 2010, Sugimura et al., 2014). Thus CR7 might be a perfect host for a DCBH.

We investigate the time-evolving spectrum of an accreting DCBH of initial mass $M_\bullet = 10^5\mathrm{M_\odot}$ by coupling a 1D radiation-hydrodynamic code (Pacucci & Ferrara, 2015) to the spectral synthesis code CLOUDY (Ferland et al., 2013), as detailed in Pacucci et al. (2015). The DCBH intrinsic spectrum is taken from Yue et al. (2013). The DCBH is at the center of a halo of total gas mass $M_g \simeq 10^7\mathrm{M_\odot}$, distributed with a core plus a r^{-2} density profile spanning up to 10 pc. The accretion is followed until complete depletion of the halo gas, i.e. for $\simeq 120\,\mathrm{Myr}$. During this period the total absorbing column density of the gas varies from an initial value of $\simeq 3.5\times10^{24}\mathrm{cm^{-2}}$ to a final value $\ll 10^{22}\mathrm{cm^{-2}}$, i.e. from mildly Compton-thick to strongly Compton-thin. Note that while Lyα attenuation by the interstellar medium is included, we do not account for the likely sub-dominant IGM analogous effect.

---

[7] As re-computed in S15 using Y band to estimate the continuum, in order to match the calculation for CR7.

[8] The LW is estimated by accounting for the stellar properties of clump B+C (in particular see Fig. 8 in S15), and by assuming a 5 kpc distance between B+C and A.

Fig. 5.4 shows the time evolution of the Lyα, He II and X-ray (0.5-2 keV) luminosities. Both Lyα and He II are consistent with the observed CR7 values during an evolutionary phase lasting $\simeq$ 17 Myr (14% of the system lifetime), longer than the shorter period ($t_\star \lesssim 2$ Myr) of our assumption for a massive Pop III burst.

The equivalent width of the He II line in the CR7 compatibility region ranges from 75 to 85 A. The column density during the CR7-compatible period is $\simeq 1.7 \times 10^{24}\mathrm{cm}^{-2}$, i.e. mildly Compton-thick. The associated X-ray luminosity is $\lesssim 10^{43}\mathrm{erg\,s}^{-1}$, fully consistent with the current upper limit for CR7 ($\lesssim 10^{44}\mathrm{erg\,s}^{-1}$, Elvis et al. 2009). Deeper X-ray observations of CR7 might then confirm the presence of the DCBH. However, this limit is already obtained with 180 ks of integration time on Chandra, meaning that a stringent test might only be possible with the next generation of X-ray telescopes.

5.4 Summary

CR7 is the brightest $z = 6.6$ LAE in the COSMOS field (Matthee et al., 2015). Spectroscopic follow-up (Sobral et al., 2015) suggests that CR7 might host Pop III stars, along with Pop II and thus be explained by a "Pop III wave" scenario. We have further investigated such interpretation using cosmological simulations following the formation of Pop II and Pop III stars in early galaxies.

We find simulated galaxies (like MB45 in Fig. 5.1) hosting both Pop III and Pop II stars at $z = 6.0$. Such "composite" galaxies have morphologies similar to that of CR7 and consistent with the "Pop III wave scenario". However, to reproduce the extreme CR7 Lyα/HeII1640 line luminosities, a top-heavy IMF combined with a massive ($M_3 \gtrsim 10^7\mathrm{M}_\odot$) Pop III burst of young stars ($t_\star \lesssim 2-5$ Myr) is required. Our simulations do not predict such large burst, i.e. $M_3 \simeq 10^6\mathrm{M}_\odot$, but our volume is also smaller than that used to discover CR7. Nonetheless, assuming that CR7 is typical of

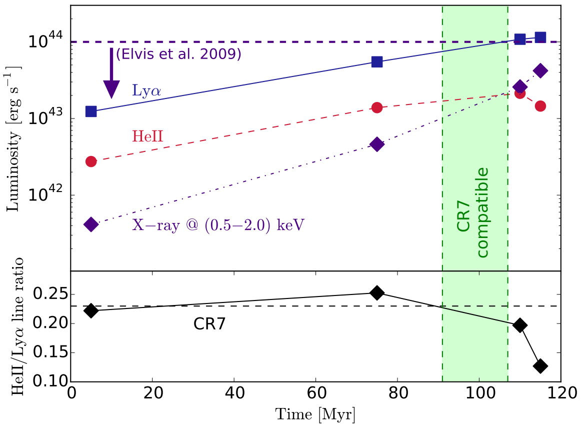

FIGURE 5.4: **Upper panel**: Time evolution of the Lyα (blue solid line), He II (red dashed line) line and X-ray (violet dot dashed line) luminosities calculated for the accretion process onto a DCBH of initial mass $10^5\mathrm{M}_\odot$. The green shaded region indicates the period of time during which our simulations are compatible with CR7 observations. The current upper limit for X-ray is $\lesssim 10^{44}\,\mathrm{erg\,s}^{-1}$, (Elvis et al., 2009, horizontal violet line). **Lower panel**: Time evolution of the HeII/Lyα lines ratio. The black horizontal dashed line indicates the observed values for CR7.

all metal-free components in our simulations, we predict that in the combined COSMOS, UDS and SA22 fields, out of the 30 LAEs with $L_\alpha > 10^{43.3}\mathrm{erg\,s^{-1}}$, 14 should also host Pop III stars producing an observable $L_{\mathrm{HeII}} \gtrsim 10^{42.7}\mathrm{erg\,s^{-1}}$.

Given the extreme requirements set by the Pop III interpretation, we explored the possibility that CR7 is instead powered by accretion onto a Direct Collapse Black Hole (DCBH) of initial mass $10^5\mathrm{M_\odot}$. The predicted L_α and L_{HeII} match CR7 observations during a time interval of $\sim 17\,\mathrm{Myr}$ ($\sim 14\%$ of the system lifetime). The predicted CR7 luminosity at 0.5-2 keV, $\lesssim 10^{43}\,\mathrm{erg\,s^{-1}}$, is significantly below the current upper limit, i.e. $\lesssim 10^{44}\,\mathrm{erg\,s^{-1}}$.

We conclude that the DCBH interpretation of CR7 is very appealing, and competitive with the explanation involving a massive Pop III burst. For both explanations, the dominant ionizing source of this galaxy should have formed from pristine gas. Deep X-ray observations and other follow-up observations should allow to shed more light on this very peculiar source.

CHAPTER 6

CONCLUSIONS

During the Ph.D. we have studied several topics in theoretical cosmology and astrophysics of galaxies, with cosmic metal enrichment being the leading thread of the research. We have constructed theoretical models based on numerical simulations, able to follow the cosmic evolution on galactic and intergalactic scales. Our state of the art simulations have been compared with the most updated observations. Our analysis and key results can be summarized as follows.

What is the cosmic metal enrichment history?

In Chapter 2 we study cosmic metal enrichment via AMR hydrodynamical simulations in a $(10\,\mathrm{Mpc}\,h^{-1})^3$ volume following the Pop III – Pop II transition and for different Pop III IMFs.

At $z \sim 4-6$ galaxies account for $\lesssim 9\%$ of the baryonic mass (Fig. 2.8); the remaining gas resides in the diffuse phases: (a) *voids*, i.e. regions with extremely low density ($\Delta \leq 1$), (b) the true *intergalactic medium* (IGM, $1 < \Delta \leq 10$) and (c) the *circumgalactic medium* (CGM, $10 < \Delta \leq 10^{2.5}$), the interface between the IGM and galaxies. By $z = 6$ a galactic mass-metallicity relation is established (Fig. 2.5). At $z = 4$, galaxies with a stellar mass $M_\star \simeq 10^{8.5} M_\odot$ show $\log(\mathrm{O}/H) + 12 = 8.19$, consistent with observations.

The total amount of heavy elements produced by stars rises from $\Omega_Z^{\mathrm{SFH}} = 1.52 \times 10^{-6}$ at $z = 6$ to 8.05×10^{-6} at $z = 4$. Metals in galaxies make up to $\simeq 0.89$ of such budget at $z = 6$ (Fig. 2.10); this fraction increases to $\simeq 0.95$ at $z = 4$. At $z = 6$ ($z = 4$) the remaining metals are distributed in CGM/IGM/voids with the following mass fractions (Fig. 2.9): 0.06/0.04/0.01 (0.03/0.02/0.01).

Analogously to galaxies, at $z = 4$ a density-metallicity ($\Delta - Z$) relation is in place for the diffuse phases (Fig. 2.11): the enriched IGM/voids have a spatially uniform metallicity, with average $Z \sim 10^{-3.5}\mathrm{Z}_\odot$; in the CGM Z steeply rises with density up to $\simeq 10^{-2}\mathrm{Z}_\odot$. In all diffuse phases a considerable fraction of metals is in a warm/hot ($T\,\mu^{-1} > 10^{4.5} K$) state (Fig. 2.9). Due to these physical conditions, C IV absorption line experiments (e.g. D'Odorico et al., 2013) can probe only $\simeq 2\%$ of the total carbon present in the IGM/CGM; however, metal absorption line spectra are very effective tools to study reionization (Fig. 2.18).

The Pop III star formation history is almost insensitive to the chosen Pop III IMF (Fig. 2.14). Pop III stars are preferentially formed in truly pristine ($Z = 0$) gas pockets, well outside polluted regions created by previous star formation episodes (Fig. 2.3).

How does feedback regulate the ISM-IGM interplay?

In Chapter 3, we focus on the properties of the circumgalactic medium (CGM) of high-z galaxies in the metal enrichment simulations presented in Chapter 2.

At $z = 4$, we find that the simulated CGM gas density profiles are self-similar, once scaled with the virial radius of the parent dark matter halo (Fig. 3.1). We also find a simple analytical expression (eq.s 3.1-3.3) relating the neutral hydrogen equivalent width ($\mathrm{EW}_{\mathrm{HI}}$) of CGM absorbers as a function of the line of sight impact parameter (b).

We test our predictions against mock spectra extracted from the simulations (Fig. 3.2), and show that the model reproduces the $\mathrm{EW}_{\mathrm{HI}}(b)$ profile extracted from the synthetic spectra analysis (Fig. 3.3). When compared with available data, our CGM model nicely predicts the $\mathrm{EW}_{\mathrm{HI}}(b)$ profile observed in $z = 0$ (Liang & Chen, 2014) and $z = 2$ (Steidel et al., 2010) galaxies (Fig. 3.3), and supports the idea that the CGM profile does not evolve with redshift.

How can we efficiently probe high-z metals?

In Chapter 4, we show how we can map metals with far-infrared (FIR) emission lines. We focus on the [C II] line at 157.74 μm, the most luminous FIR line emitted by the ISM of galaxies. Such line can also resonant scatter CMB photons inducing characteristic intensity fluctuations ($\Delta I/I_{\mathrm{CMB}}$) near the peak of the CMB spectrum, thus allowing to probe the low-density IGM (Fig. 4.2).

By using our AMR cosmological hydrodynamical simulations, we compute both [C II] galaxy emission and metal-induced CMB fluctuations at $z \sim 6$ by producing mock observations to be directly compared with ALMA BAND6 data ($\nu_{\rm obs} \sim 272$ GHz).

For galaxy we find that the [C II] line flux is correlated with $M_{\rm UV}$ as $\log(F_{\rm peak}/\mu{\rm Jy}) = -27.205 - 2.253\, M_{\rm UV} - 0.038\, M_{\rm UV}^2$ (eq. 4.2). Such relation is in very good agreement with recent ALMA observations (e.g. Capak et al., 2015, Maiolino et al., 2015) of $M_{\rm UV} < -20$ galaxies (Fig. 4.1). We predict that a $M_{\rm UV} = -19$ ($M_{\rm UV} = -18$) galaxy can be detected at 4σ in $\simeq 40$ (2000) hours, respectively.

CMB resonant scattering can produce $\simeq \pm 0.1$ μJy/beam emission/absorptions features that are very challenging to be detected with current facilities (Fig. 4.5). The best strategy to detect these signals consists in the stacking of deep ALMA observations pointing fields with known $M_{\rm UV} \simeq -19$ galaxies (Fig. 4.4). This would allow to simultaneously probe both [C II] emission from galactic reionization sources and CMB fluctuations produced by $z \sim 6$ metals (Fig. 4.3).

Can we detect the signature of the Pop III?

In Chapter 5, we analyze the case of CR7 – the brightest $z = 6.6$ Lyα emitter (LAE) known to date – that might represent the first detection of a Pop III hosting galaxy, as suggested by the spectroscopic follow-up of Sobral et al. (2015).

We examine this interpretation using cosmological hydrodynamical simulations. Several simulated galaxies show the same “Pop III wave” pattern observed in CR7 (Fig. 5.1). However, to reproduce the extreme CR7 Lyα/He II 1640 line luminosities ($L_{\alpha/{\rm HeII}}$) a top-heavy IMF and a massive ($\gtrsim 10^7 {\rm M}_\odot$) Pop III burst with age $\lesssim 2$ Myr are required (Fig. 5.2).

Assuming that the observed properties of Lyα and He II emission are typical for Pop III, we predict that in the COSMOS/UDS/SA22 fields, 14 out of the 30 LAEs at $z = 6.6$ with $L_\alpha > 10^{43.3} {\rm erg\, s^{-1}}$ should also host Pop III stars producing an observable $L_{\rm HeII} \gtrsim 10^{42.7} {\rm erg\, s^{-1}}$ (Fig. 5.3).

As an alternate explanation, we explore the possibility that CR7 is instead powered by accretion onto a Direct Collapse Black Hole (DCBH). Our model predicts L_α, $L_{\rm HeII}$, and X-ray luminosities that are in agreement with the observations (Fig. 5.4).

In any case, the observed properties of CR7 indicate that this galaxy is most likely powered by sources formed from pristine gas. We propose that further X-ray observations can distinguish between the two above scenarios.

CITATIONS TO PREVIOUSLY PUBLISHED STUDIES

Part of the content of this Thesis has already appeared in the following publications, that have been published during this Ph.D.:

- Vallini, Gallerani, Ferrara, Pallottini & Yue, *On the [C II]-SFR relation in high redshift galaxies*, 2015, ArXiv:astro-ph/1507.00340, accepted for pubblication in ApJ
- Pallottini, Ferrara, Pacucci, Gallerani, Salvadori, Schneider, Schaerer, Sobral & Matthee, *The Brightest Lyα Emitter: Pop III or Black Hole?*, 2015b, Vol. 453, 2465-2470.
- Pallottini, Gallerani, Ferrara, Yue, Vallini, Maiolino & Feruglio, *Mapping metals at high redshift with far-infrared lines*, 2015a, Vol. 453, 1898-1909.
- Yue, Ferrara, Pallottini, Gallerani & Vallini, *Intensity mapping of [C II] emission from early galaxies*, 2015, MNRAS, Vol. 450, 3829-3839.
- Campana, Salvaterra, Ferrara & Pallottini, *Missing cosmic metals revealed by X-ray absorption towards distant sources*, 2015, A&A, Vol. 575, A43.
- Pallottini, Gallerani & Ferrara, *The circumgalactic medium of high-redshift galaxies*, 2014b, MNRAS, Vol. 444, L105-L109.
- Pallottini, Ferrara, Gallerani, Salvadori & D'Odorico, *Simulating cosmic metal enrichment by the first galaxies*, 2014a, MNRAS, Vol. 440, 2498-2518.
- Pallottini, Ferrara & Evoli, *Simulating intergalactic quasar scintillation*, 2013, MNRAS, Vol. 434, 3293-3304.

preprint, (arXiv:1509.01699)

Agarwal B., Davis A. J., Khochfar S., Natarajan P., Dunlop J. S., 2013, MNRAS, 432, 3438

Agertz O., Kravtsov A. V., Leitner S. N., Gnedin N. Y., 2013, ApJ, 770, 25

Aguirre A., Schaye J., 2007, in Emsellem E., Wozniak H., Massacrier G., Gonzalez J.-F., Devriendt J., Champavert N., eds, EAS Publications Series Vol. 24, EAS Publications Series. pp 165–175 (arXiv:astro-ph/0611637), doi:10.1051/eas:2007024

Alvarez M. A., Finlator K., Trenti M., 2012, ApJL, 759, L38

Asplund M., Grevesse N., Sauval A. J., Scott P., 2009, ARA&A, 47, 481

Aubert D., Teyssier R., 2008, MNRAS, 387, 295

Barai P., et al., 2013, MNRAS, 430, 3213

Bardeen J. M., Bond J. R., Kaiser N., Szalay A. S., 1986, ApJ, 304, 15

Barkana R., Loeb A., 2001, Phys. Rep., 349, 125

Barnes L. A., Garel T., Kacprzak G. G., 2014, Publ. Astr. Soc. Pac., 126, 969

Basu K., 2007, New Astronomy Reviews, 51, 431

Basu K., Hernández-Monteagudo C., Sunyaev R. A., 2004, A&A, 416, 447

Becker G. D., Rauch M., Sargent W. L. W., 2009, ApJ, 698, 1010

Becker G. D., Hewett P. C., Worseck G., Prochaska J. X., 2013, MNRAS, 430, 2067

Begelman M. C., Volonteri M., Rees M. J., 2006, MNRAS, 370, 289

Behar E., Dado S., Dar A., Laor A., 2011, ApJ, 734, 26

Bell T. A., Viti S., Williams D. A., Crawford I. A., Price R. J., 2005, MNRAS, 357, 961

Bertschinger E., 1995, preprint, (arXiv:astro-ph/9506070)

Bertschinger E., 2001, ApJS, 137, 1

Biffi V., Maio U., 2013, MNRAS, 436, 1621

Blaizot J., Wadadekar Y., Guiderdoni B., Colombi S. T., Bertin E., Bouchet F. R., Devriendt J. E. G., Hatton S., 2005, MNRAS, 360, 159

Borthakur S., Heckman T., Strickland D., Wild V., Schiminovich D., 2013, ApJ, 768, 18

Bouwens R. J., et al., 2012, ApJ, 754, 83

Bouwens R. J., et al., 2014, preprint, (arXiv:1403.4295)

Brinchmann J., Pettini M., Charlot S., 2008, MNRAS, 385, 769

Bromm V., Coppi P. S., Larson R. B., 2002, ApJ, 564, 23

Caffau E., et al., 2011, A&A, 534, A4

Cai Z., et al., 2011, ApJL, 736, L28

Calverley A. P., Becker G. D., Haehnelt M. G., Bolton J. S., 2011, MNRAS, 412, 2543

Campana S., Thöne C. C., de Ugarte Postigo A., Tagliaferri G., Moretti A., Covino S., 2010, MNRAS, 402, 2429

Campana S., Salvaterra R., Ferrara A., Pallottini A., 2015, A&A, 575, A43

Capak P. L., et al., 2015, Nature, 522, 455

Carilli C. L., Walter F., 2013, ARA&A, 51, 105

Cassata P., et al., 2013, A&A, 556, A68

Cen R., Chisari N. E., 2011, ApJ, 731, 11

Cen R., Nagamine K., Ostriker J. P., 2005, ApJ, 635, 86

Chen H.-W., 2012, MNRAS, 427, 1238

Chen H.-W., Lanzetta K. M., Webb J. K., Barcons X., 1998, ApJ, 498, 77

Chen H.-W., Lanzetta K. M., Webb J. K., Barcons X., 2001, ApJ, 559, 654

Chiosi C., Bertelli G., Bressan A., 1992, ARA&A, 30, 235

Chluba J., 2014, preprint, (arXiv:1405.6938)

Choudhury T. R., Ferrara A., Gallerani S., 2008, MNRAS, 385, L58

Christensen C. R., Quinn T., Stinson G., Bellovary J., Wadsley J., 2010, ApJ, 717, 121

Churchill C. W., Trujillo-Gomez S., Nielsen N. M., Kacprzak G. G., 2013, ApJ, 779, 87

Ciardi B., Ferrara A., 2005, Space Science Reviews, 116, 625

Cirelli M., Corcella G., Hektor A., Hütsi G., Kadastik M., Panci P., Raidal M., Sala F., Strumia A., 2011, JCAP, 3, 51

Cooksey K. L., Thom C., Prochaska J. X., Chen H.-W., 2010, ApJ, 708, 868

Cormier D., et al., 2015, A&A, 578, A53

Crain R. A., McCarthy I. G., Schaye J., Theuns T., Frenk C. S., 2013, MNRAS, 432, 3005

Crawford M. K., Genzel R., Townes C. H., Watson D. M., 1985, ApJ, 291, 755

Croft R. A. C., 1998, in Olinto A. V., Frieman J. A., Schramm D. N., eds, Eighteenth Texas Symposium on Relativistic Astrophysics. p. 664 (`arXiv:astro-ph/9701166`)

Crosby B. D., O'Shea B. W., Smith B. D., Turk M. J., Hahn O., 2013, ApJ, 773, 108

Crow F. C., 1977, Commun. ACM, 20, 799

D'Odorico V., Calura F., Cristiani S., Viel M., 2010, VizieR Online Data Catalog, 740, 12715

D'Odorico V., et al., 2013, MNRAS, 435, 1198

Daddi E., et al., 2007, ApJ, 670, 156

Dalla Vecchia C., Schaye J., 2012, MNRAS, 426, 140

Davé R., Finlator K., Oppenheimer B. D., 2011, MNRAS, 416, 1354

Davis M., Efstathiou G., Frenk C. S., White S. D. M., 1985, ApJ, 292, 371

Dayal P., Ferrara A., Gallerani S., 2008, MNRAS, 389, 1683

Dayal P., Ferrara A., Dunlop J. S., 2013, MNRAS, 430, 2891

Dayal P., Ferrara A., Dunlop J. S., Pacucci F., 2014, MNRAS, 445, 2545

De Breuck C., Röttgering H., Miley G., van Breugel W., Best P., 2000, A&A, 362, 519

De Looze I., et al., 2014, A&A, 568, A62

Decarli R., et al., 2014, ApJL, 782, L17

Díaz C. G., Koyama Y., Ryan-Weber E. V., Cooke J., Ouchi M., Shimasaku K., Nakata F., 2014, MNRAS, 442, 946

Dodelson S., 2003, Modern cosmology. Academic Press.

Dolag K., Reinecke M., Gheller C., Imboden S., 2008, New Journal of Physics, 10, 125006

Dubois Y., Teyssier R., 2007, in Emsellem E., Wozniak H., Massacrier G., Gonzalez J.-F., Devriendt J., Champavert N., eds, EAS Publications Series Vol. 24, EAS Publications Series. pp 95–100 (`arXiv:astro-ph/0611419`), doi:10.1051/eas:2007062

Dubois Y., Teyssier R., 2008, A&A, 477, 79

Dunlop J. S., 2013a, in Wiklind T., Mobasher B., Bromm V., eds, Astrophysics and Space Science Library Vol. 396, Astrophysics and Space Science Library. p. 223 (`arXiv:1205.1543`), doi:10.1007/978-3-642-32362-1˙5

Dunlop J. S., 2013b, in Wiklind T., Mobasher B., Bromm V., eds, Astrophysics and Space Science Library Vol. 396, Astrophysics and Space Science Library. p. 223 (`arXiv:1205.1543`), doi:10.1007/978-3-642-32362-1˙5

Eisenstein D. J., Hu W., 1998, ApJ, 496, 605

Elvis M., et al., 2009, ApJS, 184, 158

Erb D. K., Pettini M., Shapley A. E., Steidel C. C., Law D. R., Reddy N. A., 2010, ApJ, 719, 1168

Fan X., Carilli C. L., Keating B., 2006, ARA&A, 44, 415

Ferland G. J., Korista K. T., Verner D. A., Ferguson J. W., Kingdon J. B., Verner E. M., 1998, Publ. Astr. Soc. Pac., 110, 761

Ferland G. J., Porter R. L., van Hoof P. A. M., Williams R. J. R., Abel N. P., Lykins M. L., Shaw G., Henney W. J., Stancil P. C., 2013, Revista Mexicana de Astronomia y Astrofisica, 49, 137

Ferrara A., 2008, in Hunt L. K., Madden S. C., Schneider R., eds, IAU Symposium Vol. 255, IAU Symposium. pp 86–99, doi:10.1017/S1743921308024630

Ferrara A., Tolstoy E., 2000, MNRAS, 313, 291

Ferrara A., Scannapieco E., Bergeron J., 2005, ApJL, 634, L37

Ferrara A., Salvadori S., Yue B., Schleicher D., 2014, MNRAS, 443, 2410

Fialkov A., Barkana R., Tseliakhovich D., Hirata C. M., 2012, MNRAS, 424, 1335

Finlator K., Muñoz J. A., Oppenheimer B. D., Oh S. P., Özel F., Davé R., 2013, MNRAS, 436, 1818

Fixsen D. J., 2009, ApJ, 707, 916

Frebel A., Kirby E. N., Simon J. D., 2010, Nature, 464, 72

Gallerani S., Choudhury T. R., Ferrara A., 2006, MNRAS, 370, 1401

Gallerani S., Ferrara A., Fan X., Choudhury T. R., 2008a, MNRAS, 386, 359

Gallerani S., Salvaterra R., Ferrara A., Choudhury T. R., 2008b, MNRAS, 388, L84

Gao L., Theuns T., Frenk C. S., Jenkins A., Helly J. C., Navarro J., Springel V., White S. D. M., 2010, MNRAS, 403, 1283

Gnedin N. Y., Ostriker J. P., 1997, ApJ, 486, 581

Gong Y., Cooray A., Silva M., Santos M. G., Bock J., Bradford C. M., Zemcov M., 2012, ApJ, 745, 49

González-López J., et al., 2014, ApJ, 784, 99

González M., Audit E., Huynh P., 2007, A&A, 464, 429

González V., Labbé I., Bouwens R. J., Illingworth G., Franx M., Kriek M., 2011, ApJL, 735, L34

Grassi T., Bovino S., Schleicher D. R. G., Prieto J., Seifried D., Simoncini E., Gianturco F. A., 2014, MNRAS, 439, 2386

Grazian A., et al., 2011, A&A, 532, A33

Greif T. H., Glover S. C. O., Bromm V., Klessen R. S., 2010, ApJ, 716, 510

Greif T. H., Bromm V., Clark P. C., Glover S. C. O., Smith R. J., Klessen R. S., Yoshida N., Springel V., 2012, MNRAS, 424, 399

Guo Q., White S., 2014, MNRAS, 437, 3228

Guo Q., White S., Li C., Boylan-Kolchin M., 2010, MNRAS, 404, 1111

Haardt F., Madau P., 1996, ApJ, 461, 20

Haardt F., Madau P., 2012, ApJ, 746, 125

Haehnelt M. G., Madau P., Kudritzki R., Haardt F., 2001, ApJL, 549, L151

Hahn O., Abel T., 2011, MNRAS, 415, 2101

Haiman Z., Bryan G. L., 2006, ApJ, 650, 7

Heap S., Bouret J.-C., Hubeny I., 2015, preprint, (`arXiv:1504.02742`)

Heger A., Woosley S. E., 2002, ApJ, 567, 532

Heywood I., Avison A., Williams C. J., 2011, preprint, (`arXiv:1106.3516`)

Hopkins P. F., Narayanan D., Murray N., 2013, MNRAS, 432, 2647

Hosokawa T., Yoshida N., Omukai K., Yorke H. W., 2012, ApJL, 760, L37

Iapichino L., Viel M., Borgani S., 2013, MNRAS, 432, 2529

Johnson J. L., 2013, in Wiklind T., Mobasher B., Bromm V., eds, Astrophysics and Space Science Library Vol. 396, Astrophysics and Space Science Library. p. 177 (`arXiv:1105.5701`), doi:10.1007/978-3-642-32362-1˙4

Johnson J. L., Dalla V. C., Khochfar S., 2013, MNRAS, 428, 1857

Kähler R., Wise J., Abel T., Hege H., 2006, Volume Graphics, 1, 103

Kashikawa N., et al., 2012, ApJ, 761, 85

Keating L. C., Haehnelt M. G., Becker G. D., Bolton J. S., 2014, MNRAS, 438, 1820

Kehrig C., Vílchez J. M., Pérez-Montero E., Iglesias-Páramo J., Brinchmann J., Kunth D., Durret F., Bayo F. M., 2015, ApJL, 801, L28

Kennicutt Jr. R. C., 1998, ApJ, 498, 541

Khandai N., Di Matteo T., Croft R., Wilkins S., Feng Y., Tucker E., DeGraf C., Liu M.-S., 2015, MNRAS, 450, 1349

Kim J.-h., et al., 2014, ApJS, 210, 14

Kirby E. N., Cohen J. G., Guhathakurta P., Cheng L., Bullock J. S., Gallazzi A., 2013, ApJ, 779, 102

Knebe A., et al., 2013, MNRAS, 435, 1618

Kobayashi C., Tominaga N., Nomoto K., 2011, ApJL, 730, L14

Krane K., 1987, Introductory Nuclear Physics. Wiley

Labadens M., Chapon D., Pomaréde D., Teyssier R., 2012, in Ballester P., Egret D., Lorente N. P. F., eds, Astronomical Society of the Pacific Conference Series Vol. 461, Astronomical Data Analysis Software and Systems XXI. p. 837

Labadens M., Pomarède D., Chapon D., Teyssier R., Bournaud F., Renaud F., Grandjouan N., 2013, in Pogorelov N. V., Audit E., Zank G. P., eds, Astronomical Society of the Pacific Conference Series Vol. 474, Numerical Modeling of Space Plasma Flows (ASTRONUM2012). p. 287 (`arXiv:1210.8014`)

Lahav O., Lilje P. B., Primack J. R., Rees M. J., 1991, MNRAS, 251, 128

Larson R. B., 1998, MNRAS, 301, 569

Larson D., et al., 2011, ApJS, 192, 16

Latif M. A., Schleicher D. R. G., Schmidt W., Niemeyer J. C., 2013, MNRAS, 436, 2989

Leitherer C., Ortiz Otálvaro P. A., Bresolin F., Kudritzki R.-P., Lo Faro B., Pauldrach A. W. A., Pettini M., Rix S. A., 2010, ApJS, 189, 309

Liang C. J., Chen H.-W., 2014, MNRAS, 445, 2061

Liddle A. R., Lyth D. H., 2000, Cosmological Inflation and Large-Scale Structure. Cambridge University Press

Ma Q., Maio U., Ciardi B., Salvaterra R., 2015, MNRAS, 449, 3006

Mac Low M.-M., Ferrara A., 1999, ApJ, 513, 142

Madau P., Dickinson M., 2014, ARA&A, 52, 415

Madau P., Haardt F., 2015, preprint, (`arXiv:1507.07678`)

Madau P., Ferrara A., Rees M. J., 2001, ApJ, 555, 92

Madden S. C., Poglitsch A., Geis N., Stacey G. J., Townes C. H., 1997, ApJ, 483, 200

Maio U., Dolag K., Ciardi B., Tornatore L., 2007, MNRAS, 379, 963

Maio U., Ciardi B., Dolag K., Tornatore L., Khochfar S., 2010, MNRAS, 407, 1003

Maiolino R., 2008, New Astronomy Reviews, 52, 339

Maiolino R., et al., 2008, A&A, 488, 463

Maiolino R., et al., 2015, MNRAS, 452, 54

Mannucci F., Cresci G., Maiolino R., Marconi A., Gnerucci A., 2010, MNRAS, 408, 2115

Maoli R., Ferrucci V., Melchiorri F., Signore M., Tosti D., 1996, ApJ, 457, 1

Maoli R., et al., 2005, in Wilson A., ed., ESA Special Publication Vol. 577, ESA Special Publication. pp 293–296 (`arXiv:astro-ph/0411641`)

Maselli A., Ferrara A., Ciardi B., 2003, MNRAS, 345, 379

Matthee J., Sobral D., Santos S., Röttgering H., Darvish B., Mobasher B., 2015, MNRAS, 451, 4919

McGaugh S. S., Wolf J., 2010, ApJ, 722, 248

McLure R. J., et al., 2011, MNRAS, 418, 2074

Meece G. R., Smith B. D., O'Shea B. W., 2014, ApJ, 783, 75

Meiksin A. A., 2009, Reviews of Modern Physics, 81, 1405

Mesinger A., McQuinn M., Spergel D. N., 2012, MNRAS, 422, 1403

Mesinger A., Ewall-Wice A., Hewitt J., 2014, MNRAS, 439, 3262

Nagao T., et al., 2008, ApJ, 680, 100

Naoz S., Noter S., Barkana R., 2006, MNRAS, 373, L98

Nielsen N. M., Churchill C. W., Kacprzak G. G., 2013, ApJ, 776, 115

Nollenberg J. G., Williams L. L. R., 2005, ApJ, 634, 793

Nomoto K., Tominaga N., Umeda H., Kobayashi C., Maeda K., 2006, Nuclear Physics A, 777, 424

Norman M. L., 2010, preprint, (`arXiv:1005.1100`)

Oh S. P., 2002, MNRAS, 336, 1021

Oppenheimer B. D., Davé R., 2006, MNRAS, 373, 1265

Oppenheimer B. D., Davé R., Finlator K., 2009, MNRAS, 396, 729

Oppenheimer B. D., Davé R., Katz N., Kollmeier J. A., Weinberg D. H., 2012, MNRAS, 420, 829

Ota K., et al., 2014, ApJ, 792, 34

Ouchi M., et al., 2009, ApJ, 696, 1164

Pacucci F., Ferrara A., 2015, MNRAS, 448, 104

Pacucci F., Ferrara A., Volonteri M., Dubus G., 2015, preprint, (`arXiv:1506.05299`)

Padmanabhan T., 1993, Structure Formation in the Universe. Cambridge University Press

Pallottini A., Ferrara A., Evoli C., 2013, MNRAS, 434, 3293

Pallottini A., Ferrara A., Gallerani S., Salvadori S., D'Odorico V., 2014a, MNRAS, 440, 2498

Pallottini A., Gallerani S., Ferrara A., 2014b, MNRAS, 444, L105

Pallottini A., Gallerani S., Ferrara A., Yue B., Vallini L., Maiolino R., Feruglio C., 2015a, MNRAS, 453, 1898

Pallottini A., Ferrara A., Pacucci F., Gallerani S., Salvadori S., Schneider R., Schaerer D., Sobral D., Matthee J., 2015b, MNRAS, 453, 2465

Panter B., Jimenez R., Heavens A. F., Charlot S., 2008, MNRAS, 391, 1117

Peebles P. J. E., 1993, Principles of Physical Cosmology. Princeton University Press

Pentericci L., et al., 2011, ApJ, 743, 132

Péroux C., Kulkarni V. P., Meiring J., Ferlet R., Khare P., Lauroesch J. T., Vladilo G., York D. G., 2006, A&A, 450, 53

Pettini M., 1999, in Walsh J. R., Rosa M. R., eds, Chemical Evolution from Zero to High Redshift. p. 233 (`arXiv:astro-ph/9902173`)

Pieri M. M., et al., 2014, MNRAS, 441, 1718

Placco V. M., Frebel A., Beers T. C., Karakas A. I., Kennedy C. R., Rossi S., Christlieb N., Stancliffe R. J., 2013, ApJ, 770, 104

Planck Collaboration et al., 2014, A&A, 571, A16

Power C., Read J. I., Hobbs A., 2014, MNRAS, 440, 3243

Press W. H., Schechter P., 1974, ApJ, 187, 425

Price D. J., 2007, Publ. Astr. Soc. Australia, 24, 159

Prochaska J. X., Chen H.-W., Howk J. C., Weiner B. J., Mulchaey J., 2004, ApJ, 617, 718

Raiter A., Schaerer D., Fosbury R. A. E., 2010, A&A, 523, A64

Rasera Y., Teyssier R., 2006, A&A, 445, 1

Rauch M., 1998, ARA&A, 36, 267

Recchi S., Hensler G., 2013, A&A, 551, A41

Reed D. S., Bower R., Frenk C. S., Jenkins A., Theuns T., 2009, MNRAS, 394, 624

Regan J. A., Johansson P. H., Wise J. H., 2014, ApJ, 795, 137

Rosdahl J., Blaizot J., Aubert D., Stranex T., Teyssier R., 2013, MNRAS, 436, 2188

Rudie G. C., et al., 2012, ApJ, 750, 67

Rudie G. C., Steidel C. C., Shapley A. E., Pettini M., 2013, ApJ, 769, 146

Ryan-Weber E. V., Pettini M., Madau P., Zych B. J., 2009, MNRAS, 395, 1476

Salvadori S., Ferrara A., 2009, MNRAS, 395, L6

Salvadori S., Ferrara A., 2012, MNRAS, 421, L29

Salvadori S., Schneider R., Ferrara A., 2007, MNRAS, 381, 647

Salvadori S., Ferrara A., Schneider R., 2008, MNRAS, 386, 348

Salvadori S., Tolstoy E., Ferrara A., Zaroubi S., 2014, MNRAS, 437, L26

Scannapieco E., Schneider R., Ferrara A., 2003, ApJ, 589, 35

Scannapieco E., Pichon C., Aracil B., Petitjean P., Thacker R. J., Pogosyan D., Bergeron J., Couchman H. M. P., 2006, MNRAS, 365, 615

Scannapieco C., et al., 2012, MNRAS, 423, 1726

Schaerer D., 2002, A&A, 382, 28

Schaye J., 2004, ApJ, 609, 667

Schaye J., Aguirre A., Kim T.-S., Theuns T., Rauch M., Sargent W. L. W., 2003, ApJ, 596, 768

Schleicher D. R. G., Galli D., Palla F., Camenzind M., Klessen R. S., Bartelmann M., Glover S. C. O., 2008, A&A, 490, 521

Schmidt M., 1959, ApJ, 129, 243

Schneider R., Ferrara A., Natarajan P., Omukai K., 2002, ApJ, 571, 30

Schneider R., Omukai K., Inoue A. K., Ferrara A., 2006, MNRAS, 369, 1437

Schön S., Mack K. J., Avram C. A., Wyithe J. S. B., Barberio E., 2015, MNRAS, 451, 2840

Schroeder J., Mesinger A., Haiman Z., 2013, MNRAS, 428, 3058

Shang C., Bryan G. L., Haiman Z., 2010, MNRAS, 402, 1249

Shen S., Madau P., Guedes J., Mayer L., Prochaska J. X., Wadsley J., 2013, ApJ, 765, 89

Sheth R. K., Tormen G., 1999, MNRAS, 308, 119

Shull J. M., 2014, ApJ, 784, 142

Shull J. M., Danforth C. W., Tilton E. M., 2014, ApJ, 796, 49

Simcoe R. A., et al., 2011, ApJ, 743, 21

Sobral D., Matthee J., Darvish B., Schaerer D., Mobasher B., Röttgering H., Santos S., Hemmati S., 2015, ApJ, 808, 139

Songaila A., 2001, ApJL, 561, L153

Songaila A., 2004, AJ, 127, 2598

Songaila A., 2005, AJ, 130, 1996

Songaila A., Cowie L. L., 1996, AJ, 112, 335

Springel V., White S. D. M., Hernquist L., 2004, in Ryder S., Pisano D., Walker M., Freeman K., eds, IAU Symposium Vol. 220, Dark Matter in Galaxies. p. 421

Stark D. P., Schenker M. A., Ellis R., Robertson B., McLure R., Dunlop J., 2013, ApJ, 763, 129

Starkenburg E., et al., 2010, A&A, 513, A34

Steidel C. C., Erb D. K., Shapley A. E., Pettini M., Reddy N., Bogosavljević M., Rudie G. C., Rakic O., 2010, ApJ, 717, 289

Storrie-Lombardi L. J., McMahon R. G., Irwin M. J., 1996, MNRAS, 283, L79

Sugimura K., Omukai K., Inoue A. K., 2014, MNRAS, 445, 544

Suginohara M., Suginohara T., Spergel D. N., 1999, ApJ, 512, 547

Sutherland R. S., Dopita M. A., 1993, ApJS, 88, 253

Tescari E., Viel M., D'Odorico V., Cristiani S., Calura F., Borgani S., Tornatore L., 2011, MNRAS, 411, 826

Teyssier R., 2002, A&A, 385, 337

Teyssier R., Moore B., Martizzi D., Dubois Y., Mayer L., 2011, MNRAS, 414, 195

Theuns T., Leonard A., Efstathiou G., Pearce F. R., Thomas P. A., 1998, MNRAS, 301, 478

Tielens A. G. G. M., Hollenbach D., 1985, ApJ, 291, 747

Tinsley B. M., 1980, Fundamentals of Cosmic Physics, 5, 287

Tolstoy E., 2010, in Bruzual G. R., Charlot S., eds, IAU Symposium Vol. 262, IAU Symposium. pp 119–126, doi:10.1017/S1743921310002632

Tornatore L., Ferrara A., Schneider R., 2007, MNRAS, 382, 945

Tremonti C. A., et al., 2004, ApJ, 613, 898

Trenti M., Stiavelli M., 2009, ApJ, 694, 879

Trenti M., Stiavelli M., Michael Shull J., 2009, ApJ, 700, 1672

Troncoso P., et al., 2014, A&A, 563, A58

Turk M. J., Smith B. D., 2011, preprint, (`arXiv:1112.4482`)

Turk M. J., Abel T., O'Shea B., 2009, Science, 325, 601

Valdés M., Evoli C., Mesinger A., Ferrara A., Yoshida N., 2013, MNRAS, 429, 1705

Vallini L., Gallerani S., Ferrara A., Baek S., 2013, MNRAS, 433, 1567

Vallini L., Gallerani S., Ferrara A., Pallottini A., Yue B., 2015, preprint, (`arXiv:1507.00340`)

Vasta M., Barlow M. J., Viti S., Yates J. A., Bell T. A., 2010, MNRAS, 404, 1910

Visbal E., Haiman Z., Bryan G. L., 2015, preprint, (`arXiv:1505.06359`)

Vogelsberger M., Genel S., Sijacki D., Torrey P., Springel V., Hernquist L., 2013, MNRAS, 436, 3031

Volonteri M., Lodato G., Natarajan P., 2008, MNRAS, 383, 1079

Wald R. M., 1984, General relativity. University of Chicago Press

Whalen D. J., et al., 2013, ApJ, 777, 110

White M., Carlstrom J. E., Dragovan M., Holzapfel W. L., 1999, ApJ, 514, 12

William E. L., Harvey E. C., 1987, COMPUTER GRAPHICS, 21, 163

Willott C. J., Carilli C. L., Wagg J., Wang R., 2015, ApJ, 807, 180

Wise J. H., Turk M. J., Norman M. L., Abel T., 2012, ApJ, 745, 50

Wolcott-Green J., Haiman Z., Bryan G. L., 2011, MNRAS, 418, 838

Wolfire M. G., Hollenbach D., McKee C. F., Tielens A. G. G. M., Bakes E. L. O., 1995, ApJ, 443, 152

Wolfire M. G., McKee C. F., Hollenbach D., Tielens A. G. G. M., 2003, ApJ, 587, 278

Woosley S. E., Weaver T. A., 1995, ApJS, 101, 181

Wyithe J. S. B., Bolton J. S., 2011, MNRAS, 412, 1926

Wyithe J. S. B., Loeb A., 2004, Nature, 432, 194

Xu H., Wise J. H., Norman M. L., 2013, ApJ, 773, 83

Yong D., Carney B. W., Friel E. D., 2012, AJ, 144, 95

Yoshida N., Omukai K., Hernquist L., Abel T., 2006, ApJ, 652, 6

Yue B., Ferrara A., Salvaterra R., Xu Y., Chen X., 2013, MNRAS, 433, 1556

Yue B., Ferrara A., Salvaterra R., Xu Y., Chen X., 2014, MNRAS, 440, 1263

Yue B., Ferrara A., Pallottini A., Gallerani S., Vallini L., 2015, MNRAS, 450, 3829

Zabl J., Nørgaard-Nielsen H. U., Fynbo J. P. U., Laursen P., Ouchi M., Kjærgaard P., 2015, MNRAS, 451, 2050

Zahn O., Mesinger A., McQuinn M., Trac H., Cen R., Hernquist L. E., 2011, MNRAS, 414, 727

Zaldarriaga M., Seljak U., 2000, ApJS, 129, 431

Zheng W., et al., 2012, Nature, 489, 406

da Cunha E., et al., 2013, ApJ, 766, 13

de Bernardis P., et al., 1993, A&A, 269, 1

de Souza R. S., Ciardi B., Maio U., Ferrara A., 2013, MNRAS, 428, 2109

van den Hoek L. B., Groenewegen M. A. T., 1997, A&A Supp., 123, 305

APPENDIX

APPENDIX

A Numerical resolution effects on Pop III SFR

The nature of Pop III stars is still under debate, and there is a lack of consensus on their formation properties and subsequent evolution. Although Chapter 2 is not specifically focused on Pop III stars, it is necessary to address numerical effects that could possibly affect Pop III evolution.

Using definitions given in Sec. 2.1.1, each Pop III formation event on average spawns a star particle with a mass $M_s = m_\star \langle N \rangle$. Using eq. 2.1b, by assuming $\langle N \rangle > 0$ and that one stellar particle is sufficient to pollute its surrounding environment, we can write

$$M_s \propto (\Delta x)^3 \Delta t / t_\star \simeq M_{\rm res}^{4/3} / t_\star \,, \tag{A.1}$$

where $M_{\rm res}$ is the mass resolution of the AMR simulation, and we have implicitly assumed a Lagrangian mass threshold-based refinement criterion. In eq. A.1 M_s is limited from below, since we expect PopIII to form in clouds of mass $\sim 10^2 - 10^3 {\rm M}_\odot$ (Bromm et al., 2002, Greif et al., 2012, Hosokawa et al., 2012, Meece et al., 2014, Yoshida et al., 2006); however, for the present estimate, we can neglect this point. Throughout the paper we have shown that each halo can host at most one Pop III formation event. Assuming no external pollution, an upper limit for the Pop III SFR can be approximated by

$$\mathrm{SFR}_{\rm PopIII} \lesssim M_s n(M > M_h^{\rm min}) / t_\star \,, \tag{A.2}$$

where $n(M > M_{\rm h}^{\rm min})$ is the number of halos with mass larger than $M_{\rm h}^{\rm min}$, the minimum mass that can host star formation. For low mass halos we can approximate $n(M >$

$M_{\rm h}^{\rm min}) \sim 1/M_{\rm h}^{\rm min}$ (Press & Schechter, 1974, Sheth & Tormen, 1999), thus

$$\mathrm{SFR}_{\rm PopIII} \propto \frac{M_{\rm res}^{4/3}}{M_h^{\rm min} t_\star^2} \,. \tag{A.3}$$

Numerically, $M_{\rm h}^{\rm min}$ is the mass of halos resolved by a suitable minimum number of particles, usually taken to be $M_{\rm h}^{\rm min} \simeq 10^{2.5} M_{\rm res}$ (Christensen et al., 2010). From the physical point of view, $M_{\rm h}^{\rm min}$ is determined by feedbacks, star formation criteria and the presence of a LW background (e.g. Johnson et al., 2013, Wise et al., 2012, Xu et al., 2013). Johnson et al. (2013) show that the LW background can induce differences in $\mathrm{SFR}_{\rm PopIII}$ up to a factor $\simeq 8$ during the early stages of star formation ($z \gtrsim 10$). Then the scaling provided by eq. A.3 reproduces well such result once the proper values of $M_{\rm h}^{\rm min}$ in the Johnson et al. (2013) simulation are inserted for the case with or without LW background.

There is a caveat regarding eq. A.3. In our formalism $t_\star$ depends on $M_{\rm res}$, and is calibrated by reproducing the observed SFR/SMD; thus, without a dedicated simulation suite, the $t_\star(M_{\rm res})$ functional dependence is uncertain. Moreover, differences in both models and implementations (Kim et al., 2014, Scannapieco et al., 2012) might hinder the effectiveness of the estimate when making a cross-code comparison.

For our fiducial simulation at $z = 6$ the Pop III SFR is $10^{-2.7}\mathrm{M}_\odot\ \mathrm{yr}^{-1}\mathrm{Mpc}^{-3}$. Using eq. A.3 and considering a slowly varying $t_\star$, our result is compatible with the values reported by Johnson et al. (2013) ($\mathrm{SFR}_{\rm PopIII} \simeq 10^{-4}\mathrm{M}_\odot\ \mathrm{yr}^{-1}\mathrm{Mpc}^{-3}$) and Wise et al. (2012) ($\mathrm{SFR}_{\rm PopIII} \simeq 10^{-4.5}\mathrm{M}_\odot\ \mathrm{yr}^{-1}\mathrm{Mpc}^{-3}$) at the same redshift.

We remind that we have not taken into account external enrichment. The estimate thus holds up to $z \gtrsim 5$, where in our simulation Pop III star formation is definitively quenched (see Sec. 2.3.1). Such quenching redshift is almost independent of resolution (see Sec. 2.5).

In principle, the pollution efficiency depends on the ratio between the galaxy correlation length, $r_{\rm SF}$, and the metal bubble size $\langle R_B \rangle$ (see Sec. 2.5 for the definitions). A rough approximation for $r_{\rm SF}$ is given by the autocorrelation scale of DM halos of mass $\gtrsim M_h^{\rm min}$. Since $M_h^{\rm min} \geq 10^{2.5} M_{\rm res}$, the quantity can be considered almost independent from resolution (Guo & White, 2014, Reed et al., 2009). On the other hand $\langle R_B \rangle$ can be estimated using the Sedov-Taylor approximation (eq. 2.8) with $\langle R_B \rangle \propto \langle (\eta_{\rm sn} M_\star)^{1/5} \rangle$, where $M_\star$ is the stellar mass per halo of mass $M_{\rm h}$. The total stellar mass is calibrated with observations (see Fig. 2.1) and for $z \lesssim 6$, in each halo with $M_{\rm h} \gtrsim 10 M_h^{\rm min}$, the stellar mass is dominated by Pop II (see Fig. 2.4). Thus $\langle R_B \rangle$ is expected to be weakly resolution dependent as $\langle R_B \rangle \propto (\eta_{sn})^{1/5}$.

As a corollary, when in a simulation $\langle R_B \rangle$ becomes comparable with the box size, chemical feedback might be artificially enhanced. However, a robust test of this idea would involve a simulation suite with increasing box size and fixed resolution and a convergence study with fixed box-size and increasing mass resolution. While this is outside the purpose of the current work, it would be interesting to analyze the problem in the future.

As a final note, in Sec. 2.1.1 we have assumed the same $t_\star$ for Pop III and Pop II. Considering two distinct star formation timescales would introduce an extra degree of freedom in the model. The natural way to fix the introduced Pop III time scale would be fitting cosmic $\mathrm{SFR}_{\mathrm{PopIII}}$ observations; however, these are not currently available.

B Rendering technique

Rendering is an efficient and widely used support tool for a cosmological simulation, since it allows an immediate visual qualitative representation of the data. A large amount of 3-D volume rendering algorithms are already present and have been specifically implemented for SPH (Dolag et al., 2008, Price, 2007), AMR (Labadens et al., 2013, Turk & Smith, 2011) and moving mesh (Vogelsberger et al., 2013) cosmological codes.

The majority of the available methods are based on a raycasting approach, which is best suited to create images from data obtained from simulations with SPH-type data structure. For the present paper we implement a rendering technique aimed at exploiting the intrinsic AMR nature of the data structure. As a matter of fact, the presence of refinement levels naturally allows the generation of high-definition images. The method is based on a voxel representation, and currently the code is still under development.

Let $\mathbf{u}$ denote the bidimensional coordinate of the image to be created and $\mathbf{x}$ the spatial coordinate of the data to be rendered. Let $\hat{n}$ denote the direction of the l.o.s. of the observer. As the data is made of AMR cubic cells (e.g. Labadens et al., 2012, 2013), the projection $\mathbf{u}(\mathbf{x})$ from the real space to the image plane depends both on the cell position, orientation respect to $\hat{n}$ and the field of view of the observer. Note that the image resolution is taken to be equal to the finest level of refinement resolved in the simulation; this implies that $\mathbf{u}(\mathbf{x})$ depends on the size of the cell.

The basic idea is that the cells can be rendered similarly to the marching cube technique (i.e. William & Harvey, 1987), thus, in principle, the part of the projection matrix depending on relative orientations can be calculated a priori. Although for now, the algorithm allows only fixed $\hat{n}$ face-on oriented respect to the cells.

To calculate the intensity I of the image we make use of a back-to-front emission-absorption rendering (e.g. Kähler et al., 2006). After sorting the data by $\hat{n}$, at every pixel I is updated via a transfer like equation

$$\mathrm{d}I\left(\mathbf{u}\right) = \left(E_{\mathrm{rt}}(\mathbf{u}(\mathbf{x})) - A_{\mathrm{rt}}(\mathbf{u}(\mathbf{x}))I\left(\mathbf{u}\right)\right)\rho(\mathbf{u}(\mathbf{x}))\mathrm{d}n \tag{B.1}$$

where E_{rt} and A_{rt} are respectively the emission and absorption coefficients, while ρ is the density field. Like in Dolag et al. (2008) we set $E_{\mathrm{rt}} = A_{\mathrm{rt}}$ in order to obtain appealing images without artifact effects. We let the coefficient dependents of the characteristic of the cell at $\mathbf{x}$ by selecting *generalized isosurface*, in order to have a smoother and less noisy final image. The rendering of the physical field q is calculated by selecting $i = 1, \ldots, n$ isosurface implicitly defined by calculating the emission coefficient as

$$E_{\mathrm{rt}}(\mathbf{x}) \propto \max_i \left\{ \exp\left[K\left(\frac{q(\mathbf{x}) - c_i}{h_i} \right) \right] \right\} \tag{B.2}$$

where K is a kernel smoothing function, h_i the bandwidth and c_i the center of the i-th isosurface. The normalization for E_{rt} is chosen in order to avoid I saturation. By using different kernels and a varying the isosurfaces, it is possible to obtain different visual effects, which can be best suited for the rendering of different physical quantities.

In particular, Fig. 2.6 is calculated by choosing 6 temperature isosurfaces. These are defined by a B-spline kernel function, with centers c_i equispaced in $\log T$, with constant bandwidths satisfying $c_i - c_{i-1} = h_i$. The balancing in the level selection ensure a good dynamical range for the temperature, thus the output is a visual appealing image that gives a representation of the temperature field convolved with the density structure. Note that the convolution is obtained by definition, since in eq. B.1 the density has the role of an optical depth.

As said the image resolution is taken is linked to the finest level of refinement resolved in the simulation. This over-sampling of the image (e.g. Crow, 1977) avoid most of the aliasing problems that occurs in rendering a 3D-voxel mesh. On the other hand, the technique augment the image processing time (e.g. Labadens et al., 2013). However, since the imaging algorithm can be massively parallelized, this does not represent a relevant issue.

Note that it is possible to have additional antialias by directly smoothing the image pixels with their neighbors (Vogelsberger et al., 2013) or –equivalently– by convolving the final image with a proper filter (Labadens et al., 2013). However, these technique degrade the image resolution and should not be required after the full implementation of the projection method.

C Numerical method for structure identification

In the present simulation structure identification is achieved in post processing via a Friend-Of-Friend (FOF) algorithm (e.g. Davis et al., 1985). While the FOF is readily able to identify particle groups, the method must be modified when dealing with cell based structure, such as the baryons of RAMSES.

In the simulation, DM and stars are traced by particles. Considering them altogether, the FOF is able to construct the complete halo catalogue and the stellar content associated with each DM group. It is important to highlight that the chosen FOF linking length is calculated by accounting only DM particles. Note that in principle the DM-stellar association can be achieved first by founding with the FOF the DM halo catalogue, then associate each star to a particular halo if the relative distance[1] is less then the halo virial radius.

Additionally, in the simulation we have identified baryonic groups, such as star forming regions ($\Delta > \Delta_{\rm th}$) and metal bubbles ($Z > Z_{\rm th} \equiv 10^{-7}{\rm Z}_\odot$). This is achieved by slightly changing the FOF algorithm to let it operate on cells rather then particles. Firstly, from the whole baryons we extract only those cells satisfying the relevant threshold criterion, i.e. density based for star forming regions or metallicity based for bubbles. The we let the FOF link the baryons by treating them as particles. It is important to state that the FOF linking length is equal to half the coarse grid size of the simulation. This choice allows the reconstruction of the proper catalogue of structure, but deny substructure identification.

To describe the properties of the baryonic regions found, we can adopt definitions similar to the one used to characterize DM halos (e.g. Springel et al., 2004, de Souza et al., 2013). The position of a region is given by the location of the density peak, while its "radius" is defined as $R \equiv V^{1/3}$, where V is the volume occupied by the selected region. As the baryons are extracted from an AMR code, there is no ambiguity in the volume definition. The shape can be described in terms of the eigenvalues I_i of the inertia tensor, where $I_1 \geq I_2 \geq I_3$. The ratios of the principal axis are used as index of sphericity (I_3/I_1), prolateness (I_3/I_2) and oblateness (I_2/I_1). The other physical quantities, such as the temperature $T_{\rm SF}$ and metallicity $Z_{\rm SF}$, are calculated as mass weighted mean on the cells.

The method for baryon groups identification have been tested on metal bubbles. We have constructed the metal bubble catalogue at various redshifts and for different values of the metallicity threshold, $Z_{\rm th}$. We have checked that the total volume occupied by the identified bubbles gives a filling factor equal to $Q(Z_{\rm th})$ at the selected redshifts (see Fig. 2.2).

Throughout the paper we have associated DM halos and stars with baryonic regions. This is achieved using a distance based criterion. Each baryonic region is linked with every DM halos whose position of the center of mass is inside the boundary of the region. We indicate with $N_{\rm h}$ the number of DM halos associated with each region. Broadly

---

[1] Distances are calculated by properly accounting for the periodic boundary conditions of the box.

speaking, for metal bubbles N_h can be regarded as an index indicating degree of merging experienced during the evolution.

D Power spectrum of the metal-induced CMB fluctuations

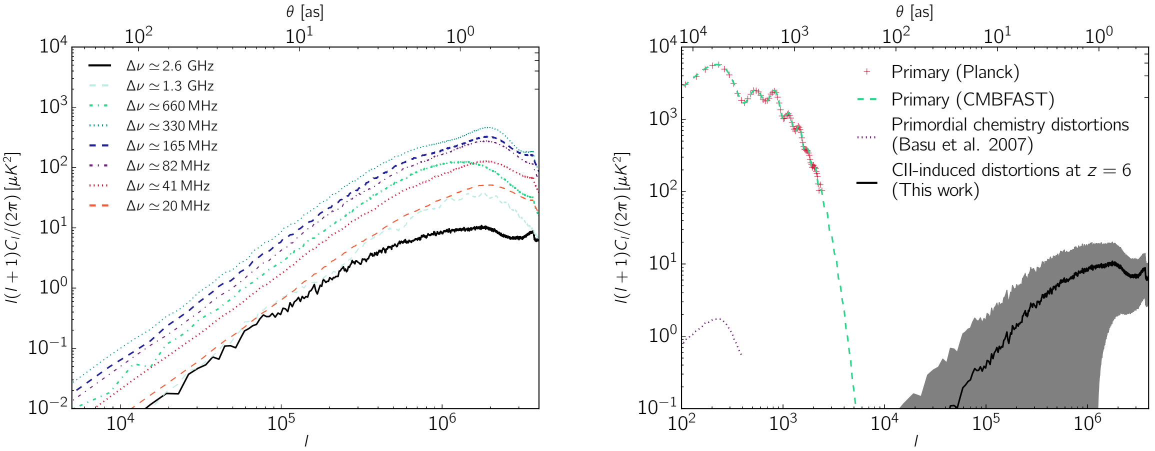

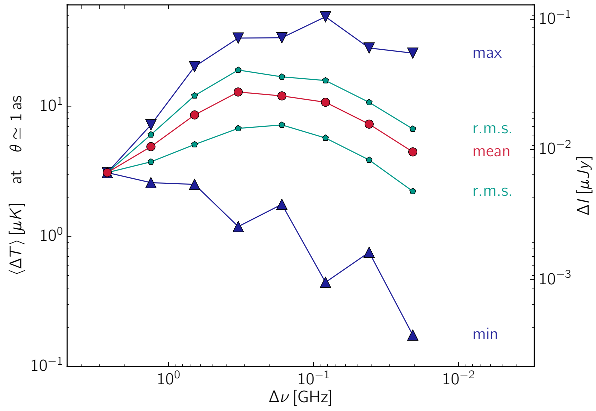

FIGURE D.1: [C II]-induced CMB power spectrum (PS, P_l) as a function of the angular scale, l and θ in the lower and upper axis, respectively. In the **upper left panel** we plot P_l calculated for different bandwidths, as indicated in the legend. In the **upper right panel** we compare our result with other PSs, as detailed in the legend and in the text. A color version of the plot is available in the online version of the paper. **lower panel**: maximum of PS ($\theta \simeq 1''$) as a function of the bandwidth ($\Delta\nu$). For each $\Delta\nu$ we plot the mean (red circles), the r.m.s. variance (green pentagons) and the max/min values (blue triangles). The maximum is indicated in unit of μK (left axis) and μJy (right axis).

We investigate the CMB fluctuations morphology by calculating the angular power spectrum (PS, C_l) of their amplitude. At $z = 6$ the simulation FOV is limited to $\simeq (350'')^2$, therefore the minimum angular scale solved is $l \simeq 10^4$. This allows us to compute the C_l in the flat-sky approximation (e.g. Mesinger et al., 2012, White et al., 1999). We calculate PS for different bandwidths 20 MHz $\lesssim \Delta\nu \lesssim$ 2.6 GHz, where the upper limit of the interval represents the total bandwidth of the simulation. For $\Delta\nu \lesssim$ 1.3 GHz, this procedure provides multiple bandwidths that we assume to be independent to calculate the averaged C_l.

In upper left panel of Fig. D.1, we plot the power spectrum as $P_l = l(l+1)C_l/2\pi$ as a function of the angular scale ($\theta = 2\pi/l$) for different bandwidths, as indicated in the legend. Independently of $\Delta\nu$, the power spectrum has a noise-like shape, i.e. $P_l \propto l^2$, for $l \lesssim 10^6$. In correspondence of smaller scales, P_l reaches a peak at $\theta \simeq 1''$ and then flattens, confirming the qualitative analysis discussed in Sec. 4.2.

In the upper right panel of Fig. D.1, we compare our result ($\Delta\nu \simeq 2.6$, solid black line) and PS for CMB distortions/fluctuations induced by primordial chemistry (Basu, 2007, violet dotted line). The latter PS is obtained for C II that are assumed to be uniformly distributed ($\Delta = 1$) at[2] $z = 4$ with $Z = 10^{-1} \mathrm{Z}_\odot$. With a grey shaded region we indicate the cosmic variance of the [C II]-induced CMB fluctuations. As a reference, we plot the primary CMB power spectrum inferred from *Planck* observations (Planck Collaboration et al., 2014, red crosses) and calculated with CMBFAST (Zaldarriaga & Seljak, 2000, green dashed line).

For the primordial fluctuations, P_l has a functional dependence on l as the primary CMB power spectrum (Basu, 2007, Schleicher et al., 2008). With respect to the primary power spectrum, these induced fluctuations produce a $\sim 10^4$ smaller power, e.g. $P_l \lesssim \mu\mathrm{K}^2$ on scales $l \lesssim 10^3$ (Basu, 2007, Basu et al., 2004).

We define, the PS peak as $\langle \Delta T \rangle = \sqrt{P_l}$ at $\theta \simeq 1''$, and we study its dependence on $\Delta\nu$. The result is shown in the lower panel of Fig. D.1, where we plot the PS peak mean value (red circles), the r.m.s. variance (green pentagons) and the max/min values (blue triangles) as a function of $\Delta\nu$. We restate that the mean and variance are calculated for the multiple bandwidths extracted from the simulation: they must not be confused with variation of CMB fluctuations from different metal bubbles.

The peak value increases with decreasing bandwidth up to $\Delta\nu \simeq 300\,\mathrm{MHz}$, and decreases for smaller $\Delta\nu$. This behavior can be explained as follows. The peak value increases as the bandwidth becomes comparable to metal bubble size in frequency space (see Fig. 4.2). As we further decrease $\Delta\nu$, it becomes increasingly difficult to find enriched structure in the selected bandwidth, and the peak becomes shallower.

Finally, note that the peak ($\sqrt{P_l}$) increases faster than $\Delta\nu^{-1}$ for $2.6 \gtrsim \Delta\nu/\mathrm{GHz} \gtrsim 0.3$ and decreases for smaller $\Delta\nu$. The power spectrum of a pure noise is expected to behave as $\Delta\nu^{-1/2}$. Therefore – in principle – the peculiar trend with $\Delta\nu$ can discriminate a signal from CMB fluctuations from noise.

---

[2] As shown in Basu (2007, in particular, see left panel of Fig. 1), at a different redshift, the primordial chemistry PS induced by C II is comparable to the one reported here.

LIST OF FIGURES

LIST OF ACRONYMS

ALMA	**A**tacama **L**arge **M**illimeter-submillimeter **A**rray
AGN	**A**ctive **G**alactic **N**ucleus
BBN	**B**ig **B**ang **N**ucleosynthesis
CDF	**C**umulative **D**istribution **F**unction
CNM	**C**old **N**eutral **M**edium
CMB	**C**osmic **M**icrowave **B**ackground
CGM	**C**ircum**g**alactic **M**edium
DCBH	**D**irect **C**ollapse **B**lack **H**ole
EOS	**E**quation **O**f **S**tate
FIR	**F**ar **I**nfra**r**ed
FWHM	**F**ull **W**idth **H**alf **M**aximum
GRB	**G**amma **R**ay **B**urst
HST	**H**ubble **S**pace **T**elescope
IGM	**I**nter**g**alactic **M**edium
IMF	**I**nitial **M**ass **F**unction
ISM	**I**nter**s**tellar **M**edium
JWST	**J**ames **W**ebb **S**pace **T**elescope
l.o.s.	**l**ine **o**f **s**ight
LAE	**L**yman **A**lpha **E**mitter
ΛCDM	**Λ** **C**old **D**ark **Matter**
LW	**L**yman **W**erner

PDF	**P**robability **D**istribution **F**unction
PDR	**P**hoto**d**issociation **R**egion
Pop II	**Pop**ulation **II**
Pop III	**Pop**ulation **III**
QSO	**Q**uasi **S**tellar **O**bject
SED	**S**pectral **E**nergy **D**istribution
SFR	**S**tar **F**ormation **R**ate
SN	**S**uper**n**ova
UV	**U**ltra**v**iolet
UVB	**U**ltra**v**iolet **B**ackground
VLT	**V**ery **L**arge **T**elescope
WNM	**W**arm **N**eutral **M**edium